CONDUCTIVITY ESTIMATION WITH EEG/MEG BRAIN SOURCE LOCALIZATION IN A FINITE ELEMENT HEAD MODEL

by

Seok Lew

A dissertation submitted to the faculty of
The University of Utah
in partial fulfillment of the requirements for the degree of

Doctor of Philosophy

Department of Bioengineering

The University of Utah

July 2008

Copyright © Seok Lew 2008

All Rights Reserved

THE UNIVERSITY OF UTAH GRADUATE SCHOOL

SUPERVISORY COMMITTEE APPROVAL

of a dissertation submitted by

Seok Lew

This dissertation has been read by each member of the following supervisory committee and by majority vote has been found to be satisfactory.

____________________	____________________
	Chair: Robert S. MacLeod
____________________	____________________
	Christopher Johnson
____________________	____________________
	Bradley Greger
____________________	____________________
	Elena Cherkaev
____________________	____________________
	Tawnya Constantino

THE UNIVERSITY OF UTAH GRADUATE SCHOOL

FINAL READING APPROVAL

To the Graduate Council of the University of Utah:

I have read the dissertation of Seok Lew in its final form and have found that (1) its format, citations, and bibliographic style are consistent and acceptable; (2) its illustrative materials including figures, tables, and charts are in place; and (3) the final manuscript is satisfactory to the Supervisory Committee and is ready for submission to The Graduate School.

Date	Robert S. MacLeod Chair, Supervisory Committee

Approved for the Major Department

Richard D. Rabbitt
Chair/Dean

Approved for the Graduate Council

David S. Chapman
Dean of The Graduate School

ABSTRACT

Brain source localization with EEG and MEG modalities provides a useful means of identifying and localizing bioelectric source in the brain. Source localization has been used as an important tool in neuroscience and in clinical applications. Due to modern imaging technology, one can construct a subject specific volume conductor model from a set of MRI or CT images that can improve the accuracy of source localization over generic models. Finite element method makes it possible to use the realistic geometry from the subject specific imaging data and to assign tissue conductivity in a flexible way. The thesis works use the FEM volume conductor model and studied three scientific issues in FEM source localization, i.e., impact of current dipole model on the accuracy of forward solution, tissue conductivity estimation with EEG data, and combined MEG/EEG conductivity estimation.

The first study is to investigate the impact of dipole models and numerical solvers on solution accuracy and computational efficiency. The accuracy and efficiency of analysis play an important role in medical diagnostics and research as well as in the field of neuroscience. In Electroencephalography (EEG) source reconstruction, a current distribution in the human brain is reconstructed noninvasively from measured potentials on the head surface (the EEG inverse problem). To solve this problem requires a numerical modeling technique to simulate head surface potentials for dipolar current sources in the human cortex, the so-called EEG forward problem. The solution to the inverse problem then becomes an iterative optimization process involving many forward solutions. The accuracy of the forward solution has a direct impact on the accuracy of inverse localization. As one of the components in volume conduction, current dipole should be modeled in the finite element space. Three FE dipole models (Venant, partial integration and subtraction methods) have been proposed in an attempt to avoid source singularity problem. We studied the impact of dipole models on the accuracy of forward solution by EEG simulation. We also evaluated the computational efficiency of the FE solvers (AMG-CG, IC-CG, Jacobi-CG) and the interplay between the solvers and the dipole models. Best accuracies were achieved by the subtraction approach. It is shown that the AMG-CG achieved an order of magnitude higher computational speed than the other solvers. Our results should broaden the application of accurate and fast high-resolution FE volume conductor modeling in source analysis routine.

The second study is to estimate the tissue conductivity with EEG data during source localization. Bioelectric source analysis in the human brain from scalp EEG signals is sensitive to geometry and conductivity properties of the different head tissues. We developed a Low Resolution Conductivity Estimation (LRCE) method using simulated annealing optimization on high resolution finite element models that individually optimizes a realistically-shaped volume conductor with regard to the tissue conductivities. As input data, the method needs T1- and PD-weighted magnetic resonance images and scalp potential data. Our simulation studies showed that for realistic signal-to-noise somatosensory evoked potentials, the LRCE method was able to simultaneously reconstruct both the brain and the skull conductivity together with the underlying dipole source in somatosensory cortex and provided an improved source analysis result. Furthermore, using scalp potentials with a high signal-to-noise ratio, the LRCE method was even able to simultaneously reconstruct a pair of dipole sources together with the brain and the skull conductivity.

The third study is to stabilize the procedure of conductivity estimation by MEG data. Adding MEG modality to the EEG could play a role of stabilizing the EEG LRCE estimation procedure, especially in case of low signal-to-noise ratio data. Since the MEG is much less sensitivity to the tissue conductivity, the MEG dipole fit provides good source parameter information that is relatively insensitive to conductivity variations. The combined analysis takes the source parameter from the MEG dipole fit and uses it as a prior constraint on the source for the EEG LRCE. We introduced a combination of iteration scheme to compensate for the radial insensitivity of MEG and to estimate conductivity more accurately. With these results, we have shown the viability of an approach that computes its own conductivity values and thus reduces the dependence on assigning values from the literature and likely produces a more robust estimate of current sources. Using the LRCE method, the individually optimized (with regard to both geometry and conductivity) volume conductor model can in a second step be used for the analysis of clinical or cognitive data acquired from the same subject.

For my family

CONTENTS

CHAPTERS

APPENDICES

LIST OF FIGURES

LIST OF TABLES

ACKNOWLEDGEMENTS

I am very grateful to those who made it possible for me to finish Ph.D. program and who made my student life a fruitful time. The discussions with colleagues and friends in the SCI institute and the bioengineering department were a great asset to improve this thesis research.

First of all, I would like to give many thanks to my advisor Dr. Rob MacLeod. He is a great mentor. When I talked to him about an issue, he was always open to listen and lead me to come up with a good solution. He encouraged me to think critically and independently, so that I could prepare for my future academic career. His simple tips in how to manage multiple works simultaneously helped me a lot to reorganize my works more efficiently. Specially I learned a lot from him about professional academic writing. He was the one who made me think writing could be a fun job even though it's hard. Chatting with him about my career in academia was a great chance to taste the environment of a professional researcher.

I would like to give special thanks to Dr. Carsten Wolters who brought me into the field of brain source analysis. Since then, he continued to support me intellectually and to show a vision in the field, so that I could make everyday progress in the source analysis. Whenever I came up with scientific, technical, or general inquiries, he was very prompt in responding to them from Muenster Germany. I also want to recognize his hospitality during my visit to Muenster. He allowed me to stay at his apartment, so that we could discuss the core of my thesis work more closely.

I also give thanks to my committee who provided me a research direction and a technical assistance. Dr. Chris Johnson showed me a vision in computational science and engineering. Dr. Tawnya Constantino helped me understand the clinical issues in the research, especially in the epilepsy diagnosis. Dr. Elena Cherkaev gave good feedback on the mathematical portion of the research works. Dr. Bradley Greger gave me practical advise about a future career in brain science.

I want to give thanks to my wife Sookhyun for her support and prayer, to my daughter Michelle for her silent support during my study at home, to my son Chris for his smile

when I was exhausted, to my father and mother who prayed for me like always, and to parents-in-law for their financial support to travel to Korea during vacations.

CHAPTER 1

INTRODUCTION

Brain source localization is defined as reconstructing current sources responsible for the electric and/or magnetic field distributed in the conducting medium of the human head. Source localization with the data from the modalities such as EEG (Electroencephalograpy) or MEG (Magnetoencephalograpy) provides clinically significant information of source parameters that can indicate the activity of brain functional disorders such as epilepsy. An essential and critical component of source reconstruction is the head volume conductor model, which contains both the geometry and the electrical conduction properties of the head tissues. Studies have shown that the accuracy of both parameters has a direct impact on the accuracy of the source localization [5–7] so that it has become desirable to have patient specific models of the head. There are practical challenges to creating patient specific conductor models that currently prohibit this degree of customization for each routine case of clinical source localization. Specifically, the conductivities of head tissues vary across individuals and within the same individual due to variations in age, size, disease state, and environmental factors. In fact, while modern imaging modalities provide the information necessary for geometric accuracy, there is no functional equivalent that will provide conductivity information.

We propose an approach that will deal with uncertainty in conductivity by incorporating that uncertainty into the solution method and solving the resulting formulation both for the source parameters and the conductivity values. **The hypothesis of this dissertation is that customized tissue conductivities with realistic head geometry will improve the accuracy of source localization and that incorporating conductivity parameters into the problem formulation will achieve those improvements.** The hypothesis is based on the following observations. **First**, accurate knowledge of bioelectric source parameter provides valuable information for the diagnosis and pre-surgical planning of a patients with focal abnormal brain activity. Subject-specific volume conductor models in terms of geometry and conductivity are the basis for obtaining the accurate source information. **Second**, medical images from MR and/or CT techniques provide accurate geometry information of the human head and enable the creation of realistic finite element head models. **Third**, a prevailing disadvantage of the computational cost for the FEM (Finite Element Method) no longer exists because the recent development of efficient FE solvers and the transfer matrix (or lead field basis) approach reduces the complexity of FE computation. Global optimizers such as SA (Simulated Annealing) are able to effectively handle multiple optimization parameters of both source locations and tissue conductivities. **Forth**, recent studies to resolve the uncertainty of conductivity values with sphere head model and/or boundary element model have shows that incorporating the conductivity variance into the source localization procedure improve the accuracy of source localization. **Based on these observations, the main goal of this research was to individually optimizes a realistically-shaped volume conductor with regard to the tissue conductivities and evaluate the resulting improvements in solution accuracy.**

The following specific aims were designed to develop the hypothesis and served as the major topics of the thesis.

1. **Evaluate the role of the choice of FE solver and FE dipole model on the accuracy of the forward computation.** We investigated the impact with three FE solvers (Jacobi-CG, IC-CG, and AMG-CG) and three FE dipole source models (Venant method, partial integration approach, and subtraction method) and compared accuracy and computational cost. The importance of the specific choice of FE solver and FE dipole model on the accuracy of forward solution lies in the fact that the inverse dipole fit method is based on iterative calls of a forward simulation. We computed the solutions using a sphere FE model and evaluated the accuracy with that of analytic solution for the same sphere model model.

2. **Estimate tissue conductivity as part of the EEG source localization.** We developed a new method of LRCE (Low Resolution Conductivity Estimation) that estimates tissue conductivities during source localization by allowing each tissue conductivity to vary within a predefined set of values. The method used a realistic FE head geometry created from a single subject's three-dimensional MR images. We tested our method with simulated EEG data and also applied it to empirical

SEP (Somatosensory Evoked Potentials) EEG data collected from the subject in order to estimate subject specific brain and skull conductivity.

3. **Estimate tissue conductivity with EEG/MEG combined modalities.** We apply EEG/MEG combined analysis to the LRCE method in order to estimate tissue conductivity. Using combined EEG and MEG data in combination with realistic FE head geometry should further stabilize the application of the LRCE method for the estimation of tissue conductivities. Given the FE head model, we use the simulated MEG data to obtain the source parameters by MEG dipole fit method. Then we apply our LRCE method to the simulated EEG data in order to estimate brain and skull conductivities by fixing the source parameters to the MEG fitted source. We continue to apply the method to real SEP/SEF (Somatosensory Evoked Fields) data to estimate brain and skull conductivities.

The research was thus organized into three separate projects, each of which was destined to result in a publication. in order to produce this dissertation, we begin with a general introduction of the motivation for solving this problem. We then continue with a background chapter on bioelectric field and one on the finite element approach as it applies to bioelectric field problems. We then provide a chapter for each of three projects that include specific methods, results and discussion sections. The dissertation concludes with some general observations and an outline of some future research.

1.1 Motivation

The in-depth introduction of each aim is described in the following three sections.

1.1.1 Evaluate the role of the choice of FE solver and FE dipole model on the accuracy of the forward computation.

Electroencephalography (EEG) based source reconstruction of cerebral activity (the EEG inverse problem) is an important tool both in clinical practice and research [8], and in cognitive neuroscience [9]. Methods for solving the inverse problem are based on solutions to the corresponding forward problem, i.e., the simulation of EEG potentials for a given primary source in the brain using a volume-conduction model of the human head. While the theory of this forward problem is well established and many numerical implementations exist, there remain unresolved questions regarding the accuracy and efficiency of contemporary approaches. In this study, we compared a range of numerical techniques and source representation approaches in the finite element method (FEM) and have shown that careful choice of both are critical in order to solve realistic elecroencephalographic forward (and inverse) problems.

The general approach for solving bioelectric field problems under realistic conditions is well established and all quantitative solutions for the EEG forward problem are based on the quasi-static Maxwell equations [10]. While boundary element method is able to represent a head by realistic surface based compartments and to assign tissue conductivity to each compartment, the finite element method has more flexibility in segmenting the head and assigning conductivity. The main advantage of finite element method is that it allows for a realistic representation of the complicated head volume conductor with its tissue conductivity inhomogeneities and especially anisotropies [11–21].

The primary sources in the brain activity are electrolytic currents within the dendrites of the large pyramidal cells of activated neurons in the human cortex. Even though one can formulate more integrated estimates of the source [22], most often the primary sources are formulated as a mathematical point current dipole [10, 23, 24]. To implement the point current dipole as a source in the brain, the FE method requires careful consideration of the singularity of the potential that inevitably arises at the source position.

One way to address this singularity is to use a "subtraction approach", which divides the total potential into an analytically known singularity potential and a singularity-free correction potential, which can then be approximated numerically using an FE approach [12–14, 16, 19–21]. For the correction potential, the existence and uniqueness for a weak solution in a zero-mean function space have been proven and FE convergence properties are known [20]. It has also been established that a full subtraction approach [21] leads to an order of magnitude more accurate solution than a common alternative, the projected subtraction approach [20], especially when considering sources that are close to a conductivity inhomogeneity. Another family of source representation methods, known as direct FE approaches to the total potential [11, 13, 15, 18, 19], are computationally less expensive, but also mathematically less sound under the assumption that a point dipole is a realistic source model.

Another general requirement for FE modeling of bioelectric fields is a volumetric mesh that represents the head geometry with tissue electric properties assigned to each element. An effective meshing strategy will balance acceptable forward problem accuracy against reasonable computation times and memory usage. Very high accuracies can be achieved by making use of a Constrained Delaunay Tetrahedralization (CDT) in combination with a full subtraction approach [21]. Adaptive methods, using local refinement around the source singularity [12, 14], are another potential utility but they preclude the use of fast transfer matrices [18, 25–27] and lose efficiency in solving the inverse problem (see discussion section in Chapter 4).

Solving the forward problem is rarely the ultimate goal in calculating bioelectric fields but rather a step towards solving the associated inverse problem. Thus the quest for numerical accuracy and efficiency of the forward solution requires some anticipation of the ultimate use in inverse solutions. The longtime state-of-the-art approach has been to solve an FE equation system for each anatomically and physiologically meaningful dipolar source (each source results in one FE right-hand side (RHS) vector) [12–16]. The use of standard direct (banded LU factorization for a 2D source analysis scenario [13]) or iterative (Conjugate Gradient (CG) without preconditioning [12] or Successive Over-Relaxation (SOR) [19]) FE solver techniques limit the overall resolution of the geometric model because of their computational cost. The preconditioned CG method has been used with standard preconditioners like Jacobi (Jacobi-CG) [18] or incomplete Cholesky without fill-in, IC(0)-CG [15], and algebraic multigrid (AMG-CG) [28].

One recent approach to achieve efficient computation of the FE-based forward problem is to pre-compute "transfer matrices" that encapsulate the relationship between source locations and sensor sites based only on the geometric and conductivity characteristics of the volume conductor, i.e., they are independent of the source. Techniques exist to construct transfer matrices for problem formulations based on EEG [18, 27] or combined EEG and MEG [25, 26]. Using this principle, for each head model, one only has to solve one large sparse system of equations for each of the possible sensor locations in order to compute the full transfer matrix. Each forward solution is then reduced to multiplication of the transfer matrix by an FE RHS vector containing the source load. Exploiting the fact that the number of sensors (typically up to about 600) is much smaller than the number of reasonable dipolar sources (tens of thousands), the transfer matrix approach is substantially faster than the state-of-the-art forward approach (i.e., solving an FE equation system for each source) and can be applied to inverse reconstruction algorithms in both continuous and discrete source parameter space for EEG and MEG. Still, the solution of hundreds of large linear FE equation systems for the construction of the transfer matrices is a major time consuming part of FE-based source analysis.

The first goal of this study was therefore to compare the numerical accuracy of the full subtraction approach [21] with the two direct approaches using partial integration [11, 13, 18] and Venant principle [15] in specifically-tuned CDT meshes of an anisotropic four-compartment sphere model for which quasi-analytical solutions exist [29]. We then examined the interplay of the source model approaches with three FE solver methods: a Jacobi-CG, an incomplete Cholesky CG (e.g., [30]), and an algebraic multigrid preconditioned CG (AMG-CG), the last of which has already shown to be especially well suited for problems with discontinuous and anisotropic coefficients [28, 31–34].

1.1.2 Estimate tissue conductivity with EEG source localization

The elecroencephalographic inverse problem is an attempt to reconstruct the underlying current source activity in the human brain by measuring the potential differences among the sensor electrodes on the head surface. The head volume conductor model, the significant factor of EEG source reconstruction, has an strong impact on the accurate solution of the bioelectric problem. The reconstruction is associated with a forward problem, which is defined as the simulation of the electroencephalogram (EEG) for a known current source in the brain. The volume conductor model contains two major components, the geometry and the electrical conduction properties of the head tissues, and the accuracy of both parameters has direct (but not fully predictable) impact on the accuracy of the source analysis [5–7]. The current challenges of creating patient specific models in practice does not allow this degree of customization for each routine case of clinical source analysis. Thus it is essential to identify the parameters that have the largest impact on solution accuracy and to attempt to customize them to the particular case.

The volume conductor model used in this study consisted of four individually and accurately shaped compartments, the scalp, skull, CSF, and brain, and was created from MR imaging of a normal subject. Magnetic Resonance (MR) or Computed Tomography (CT) imaging provides the geometry information for the brain, the cerebrospinal fluid (CSF), the skull, and the scalp [3, 7, 35, 36]. MRI has the advantage of being a completely safe and noninvasive method for imaging the head, while CT provides better definition of hard tissues such as bone. However, CT is not justified for routine physiological studies in healthy human subjects. In this study we used a combination of T1-weighted MRI, which is well suited for the identification of soft tissues (scalp, brain) and proton-density (PD) weighted MRI, enabling the segmentation of the inner skull surface [3]. This approach leads to an improved modeling of the skull thickness over standard (T1) weighted MRI, an important parameter for a successful application of the proposed low resolution conductivity estimation (LRCE) method in Chapter 5.

There is no imaging modality that can measure the absolute value of tissue conductivity. Diffusion tensor (DT) imaging is able to provide the directional preference of the electric conduction, however, it is not able to measure the value of the conductivity. There have been studies to get the tissue conductivity values. It is possible using cadaveric and animal tissue measurement to estimate tissue conductivity values. Baumann et al. [37] measured the conductivity of CSF and reported a value of 1.79 S/m which has been accepted in the biomagnetism community. By contrast, a value of skull conductivity remains disputed in the community. Various methods such as measurement of living tissues, electrical impedance tomography (EIT), and indirect estimation with evoked potential experiments have been proposed, but the reported values (relative to brain conductivity) are in the wide range of from 15 to 80 [38–45]. Considering that the skull conductivity is by far lowest of the head tissues, the accuracy of the skull tissue conductivity has more impact on the EEG forward problem than those of any other tissues. At this point, there is little hope that direct measurement will resolve these large discrepancies, some of which may originate in inter-patient differences or natural variations over time. We propose an approach that seeks to adjust the conductivity each individual case by making conductivity an additional parameter to be solved.

A growing body of evidence suggests that the quality and fidelity of the volume conductor model of the head plays a key role in solution accuracy [7, 36, 46], so that the choice of numerical method could drive the overall accuracy of source reconstruction. There is a wide range of approaches suitable for this problem including multi-layer sphere models [47], the boundary element method (BEM) [36, 48–51], the finite difference method (FDM) [52] and the finite element method (FEM) [3, 7, 53–56]. The FEM offers the most flexibility in assigning both accurate geometry and detailed conductivity attributes to the model, at the cost of both creating and computing on the necessary geometric model. The use of recently developed FEM transfer matrix (or lead field basis) approaches [6, 56, 57] and advances in efficient FEM solver techniques for source analysis [58] drastically reduce the complexity of the computations so that one major disadvantage of FEM modeling no longer exists. Lanfer *et al* [4] compared run-time and numerical accuracy of an FEM source analysis approach using the Venant dipole model [5] and the fast FE transfer matrix approach [57] with an ISA vertex collocation BE approach, i.e., a double layer collocation BE method using the isolated skull approach (ISA) [49] and linear basis functions with analytically integrated elements [50] in combination with BE transfer matrices [59] in an isotropic three layer sphere model. The reported numerical errors of the Venant FE approach for realistic eccentricities were in the same range as those of the BE approach, while, at the same time, the Venant FE forward computation was faster than the BE forward computation. Additionally, similar errors and run times were achieved with the Venant FE approach in anisotropic four compartment sphere models, showing the large flexibility of this approach.

In this study, we propose a Low Resolution Conductivity Estimation (LRCE) method using simulated annealing optimization in a realistically-shaped four compartment (scalp, skull, CSF and brain) finite element volume conductor model that individually optimizes the brain and the skull conductivity parameters. Like other source analysis approaches, the LRCE method uses a geometric model, in this case based on T1-/PD-MRI, and scalp EEG potentials as input. The method then determines the best combination of sources within the somatosensory cortex together with the two individually optimized brain and skull conductivity values over a discrete parameter space, i.e., for each source and for each tissue conductivity the user has to define a reasonable set of *a priori* values. We evaluated the accuracy of the LRCE method in simulation studies before applying it to tactile somatosensory evoked potentials with the focus on establishing the best values for the individual brain and skull conductivity. The results from the study will appear in more detail in Section 5.3

1.1.3 Estimate tissue conductivity with EEG/MEG combined modalities.

One of the recent trends in the community of brain source localization is the use of multiple functional modalities that include EEG/MEG [51, 60], fMRI/EEG [61], fMRI/MEG [62], fMRI/EEG/MEG [63], and the combination of EEG/MEG/fMRI/DOT (Diffuse Optical Tomography) [64]. The rational for these combined modalities in source localization is mainly due to the fact that not a single modality can recover all aspects of the functional source parameter and, accordingly, combining each one's advantage may maximize the accuracy of source estimation. For instance, fMRI has a very good spacial resolution ($1\tilde{3}$mm), while the temporal resolution is in the range of a second [65].

Combining fMRI with EEG or MEG, which both have a good temporal resolution, can give an improved source estimation. We propose a combination of MEG/EEG specifically to estimate the tissue conductivity.

The EEG has a strong sensitivity to electric conductivity that the MEG does not have. The relative insensitivity of MEG to the tissue conductivity results in more accurate source reconstruction in the face of conductivity variation, which can in turn justify the high measurement system cost. However, the MEG modality has a poor sensitivity to the radial component of any source; the extreme case of a purely radial source in a perfect sphere, the MEG does not sense any source activity because of the symmetry that leads to a cancellation of the magnetic field. This is the major weakness of the MEG modality, compared to EEG, which is equally sensitive to both radial and tangential source orientations.

The goal of MEG/EEG combined analysis is to use the strengths and compensate for the weaknesses of both modalities in order to maximize the localization accuracy. In our study, we used the combined MEG/EEG analysis in a novel way to estimate the tissue conductivity in order to also minimize source localization error. Our initial attempts to apply the LRCE approach to EEG measurement alone were successful only under conditions of high signal to noise ratio, conditions that are not always practicable in realistic settings. Thus it seemed using the information from MEG based source localization, it would be possible to stabilize the EEG based conductivity estimation even under low signal-to-noise conditions.

Recent study of Huang *et al* [66] introduced a combined MEG/EEG method to estimate the tissue conductivity ratio. He showed the feasibility of his method with simulation studies with spherical head and boundary element models. The simulation results suggested that the conductivity ratio between skull and CSF is not a constant, but rather a function of the absolute conductivity values. That is, the best fitted ratio changes depending on the assumed tissue conductivity values. Huang *et al*'s use of MEG and EEG shares common origins with our proposed method in that the MEG provided source location information and the conductivity ratio was estimated with the EEG, based on the least square fit between the tangential source component of the MEG and the tangential component of the EEG computed with different conductivities. In their study, the authors introduced a SVD based extraction method that decomposed the radial and the tangential components of the source parameter from the MEG gain matrix and used the tangential component to estimate the conductivity.

In this study, we extended the EEG based LRCE to the EEG/MEG combined analysis in order to more accurately estimate tissue conductivity. With the realistic FEM head model in hand, the combined methods should stabilize the application of the LRCE method for the estimation of tissue conductivities. Given the same FEM head model as in the EEG LRCE study, we performed simulation studies with a single somatosensory source. The MEG dipole fit method localized the source parameter and served as a stabilizing constraint to the EEG LRCE in order to estimate brain and skull conductivities. We apply the MEG/EEG combined method to real SEF/SEP (Somatosensory Evoked Field/Potential) data to estimate brain and skull conductivities of a subject. Besides using our new method for an improved source analysis of somatosensory evoked potentials, the major future perspective for the LRCE is to provide an individually optimized volume conductor model that can then be used in a second step for the analysis of clinical or cognitive EEG data.

1.2 Organization of the Dissertation

This thesis document consists of seven chapters including introduction, background, FEM model, forward accuracy study, EEG conductivity estimation, MEG/EEG combined analysis, and future study.

Chapter 1 has introduced the overall aims and the specific research topics of the thesis work. It also described the background information and the relevant previous researches for each topic.

Chapter 2 describes the technical background of the bioelectric forward and inverse problems. It includes the physics of the problem, components of the volume conductor, origin of the bioelectric source, EEG/MEG measurement, brain source localization, and optimized conductor model.

Chapter 3 formulates the bioelectric problem with the EEG/MEG modalities in the finite element domain. Here we describes the mathematical dipole source models and the iterative finite element solvers that served as a basis for the forward computation and inverse dipole fit method.

Chapter 4 reports on studies of the accuracy and the computational efficiency of a set of FEM solvers and dipole models based on a large number of forward computations to compare the choice of solver and dipole.

Chapter 5 describes a new method to estimate conductivity based on EEG data. The simulation results of the LRCE method are presented to show the estimation of brain and skull conductivities for both single source and two source models. Also shown are the results of the application to the real EEG data.

Chapter 6 presents a combined MEG/EEG conductivity estimation. This is a continuation of the work in Chapter 5 with an extension to the MEG modality in an attempt to stabilize the inverse solution process with a strong constraint. We describes the simulation studies and the real data application with a single somatosensory dipole and discusses utility and the feasibility of the method.

Chapter 7 summarizes the outcomes of the thesis research and discusses possible future studies.

CHAPTER 2

BACKGROUND

2.1 Bioelectric Problem

Bioelectric fields in the brain come from neuronal excitations that are essential to brain function. The excited neurons are the origin of electric fields and can be modeled as current dipoles. The resulting currents travel through a conducting medium, which is the head volume consisting of inhomogeneous tissues such as brain, CSF, skull, and scalp. In the low frequency band (frequencies below 1000 Hz) of neuronal activities, the capacitive component of tissue impedance, the inductive effect, and the electromagnetic propagation effect can be neglected so that the relationship between bioelectric fields and the underlying current sources in the brain can be represented by the quasi-static Maxwell equations and reduced to a Poisson's equations as follows.

$$\begin{aligned} \nabla \cdot (\sigma \nabla \Phi) &= \nabla \cdot \mathbf{j}^p \text{ in } \Omega, \qquad (2.1) \\ \sigma \frac{\partial \Phi}{\partial \mathbf{n}} &= 0 \text{ on } \Gamma = \partial \Omega, \end{aligned}$$

where $\mathbf{j}^p$ is the primary current source, Φ is an electric potential distribution in the head domain (Ω), σ is the electric tissue conductivity, Γ is the homogeneous Neumann boundary on the head surface, and $\mathbf{n}$ is the surface normal [48, 67]. The primary current $\mathbf{j}^p$ can be mathematically modeled by a dipole moment

$$\mathbf{j}^p = \mathbf{M}_0 \; \delta(\mathbf{x} - \mathbf{x}_0) \qquad (2.2)$$

at position $\mathbf{x}_0$ with the moment $\mathbf{M}_0$ composed of strength and direction.

With adequate knowledge of the bioelectric sources (primary current) and the electrical characteristics (tissue conductivity) of the volume conductor, it is possible to calculate the potentials from the brain by the Poisson's equation (Eq. 2.1). The EEG measures the electric potentials (Φ) at electrode locations on the scalp surface (Γ) as a result of the volume conduction. This process of computing head potentials from known sources is called the EEG forward problem (Figure 2.1).

It is well known that the current also generates magnetic field around the current conducting pathway. MEG is a modality that uses remotely located pickup coils to measures the magnetic field induced from the primary current activity in the head. Both the primary current and the volume current defined in the EEG forward problem are sources of magnetic field that MEG can detect. Based on the the quasi-static Maxwell equations, a magnetic potential A can be formulated as

$$\mathbf{A}(\mathbf{x}) = \frac{\mu}{4\pi} \int_{\Omega} \frac{\mathbf{j}^p(\mathbf{y}) - \sigma(\mathbf{y})\nabla\Phi(\mathbf{y})}{|\mathbf{x} - \mathbf{y}|} d\mathbf{y}, \tag{2.3}$$

where μ is magnetic permeability.

We can determine the magnetic flux (Ψ) through a magnetometer flux transformer γ based on Stokes theorem.

$$\Psi = \int_S \mathbf{B} dS = \oint_\gamma \mathbf{A}(\mathbf{x}) d\mathbf{x}, \tag{2.4}$$

where B is magnetic induction and S is surface enclosed by the transformer $\gamma \equiv \partial S$. Then the magnetic flux becomes

$$\begin{aligned} \Psi &= \Psi_{pri} + \Psi_{sec} \\ &= \frac{\mu}{4\pi} \oint_\gamma \int_\Omega \frac{\mathbf{j}^p(\mathbf{y})}{|\mathbf{x} - \mathbf{y}|} d\mathbf{y} \cdot d\mathbf{x} + \frac{\mu}{4\pi} \oint_\gamma \int_\Omega \frac{-\sigma(\mathbf{y})\nabla\Phi(\mathbf{y})}{|\mathbf{x} - \mathbf{y}|} d\mathbf{y} \cdot d\mathbf{x}. \end{aligned} \tag{2.5}$$

Here we can also see that the magnetic flux comes from two current sources, i.e., from the primary dipole current, $\mathbf{j}^p$, and the secondary volume current, $\sigma(\mathbf{y})\nabla\Phi(\mathbf{y})$. Replacing $\mathbf{j}^p$ with $\mathbf{M}_0\delta(\mathbf{x} - \mathbf{x}_0)$ and introducing $\mathbf{C}(\mathbf{y})$

$$\mathbf{C}(\mathbf{y}) = \oint_\gamma \frac{1}{|\mathbf{x} - \mathbf{y}|} d\mathbf{x}, \tag{2.6}$$

the magnetic flux can be simplified as

$$\Psi_{pri} = \frac{\mu}{4\pi} < \mathbf{M}_0, \mathbf{C}(\mathbf{x}_0) > \tag{2.7}$$

$$\Psi_{sec} = -\frac{\mu}{4\pi} \int_\Omega < \sigma(\mathbf{y})\nabla\Phi(\mathbf{y}), \mathbf{C}(\mathbf{y}) > d\mathbf{y}, \tag{2.8}$$

where $< \cdot, \cdot >$ is the scalar product.

When the conducting medium is an unbounded infinite homogeneous medium, the volume current has no contribution to the magnetic flux due to cancellation [48]. Accordingly, the secondary magnetic flux (Ψ_{sec}) goes to zero and MEG measures only the primary magnetic flux. Even with a special case of a simple bounded medium such as a sphere, we can measure only the primary magnetic flux (Ψ_{pri}) with radial MEG sensors because the secondary fluxes are canceled by the symmetry of the sphere [48]. In this case, the electric conductivity (σ) has no impact on the magnetic flux, since primary magnetic flux comes purely from the primary dipole sources. However, a volume conductor of realistic head geometry will generate both primary and secondary magnetic fluxes because the conductor is no longer a perfect sphere.

In the EEG and MEG bioelectric problems, it is also possible to carry out the reverse, i.e. calculate the sources from the known or measured electric potentials and magnetic fields (Figure 2.1). This reverse solution process is called the EEG and MEG inverse problem. The inverse problem was more clinical relevance than the forward problem and this is the focus of most neuroscience research. However, the practical challenge is that the inverse problem may not lead to unique solutions and even if unique solutions are possible, there is great instability of the solution due to the noise in EEG/MEG. Nevertheless, proper *a priori* information and regularization techniques can stabilize the inverse solution process.

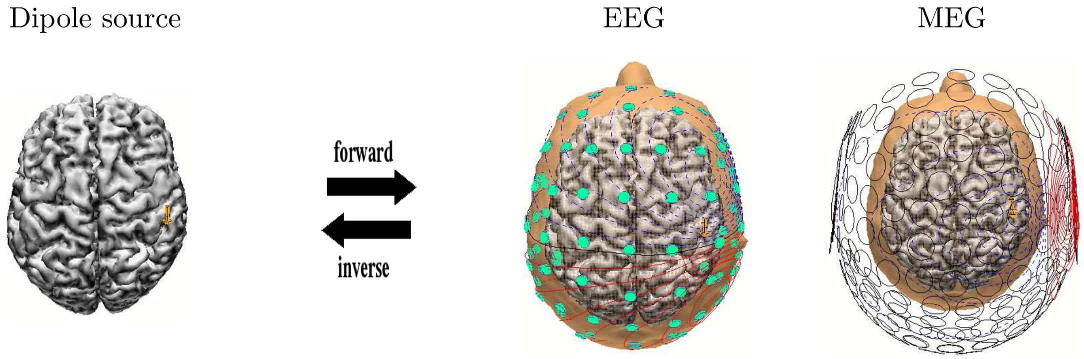

Figure 2.1. Forward and inverse problem in bioelectric study. Dipole sources in the cortex of the brain generate electric and magnetic fields that can be measured by EEG or MEG, respectively. Under appropriate conditions, it is possible to localize unknown source dipoles from the measured electric or magnetic fields (the inverse problem).

2.2 Modeling of Dipole Source

Action potentials are the fundamental means of communication and information transfer in the brain. However, the extracellular fields from action potentials (1-2 mm) do not last long enough to create measurable electric or magnetic fields at the scalp. Instead, it is the subthreshold depolarization and hyperpolarization that lead to measurable fields due to their longer duration (10-200 ms), despite their smaller amplitude. In addition, the electric source activity due to the action potential, which can be modeled as a quadrupole, has less effects on electrodes at the head surface because the potential distribution from the quadrupole is proportional to distance from the source as $1/r^4$, where that of the dipole is proportional to $1/r^2$. Specifically the origin of the bioelectric sources in the EEG and MEG is the subthreshold activity at the postsynaptic junction which create a dipolar field.

The anatomical origin of the sources is most likely the pyramidal cells in the gray matter of the cortex (regions III and IV in Figure 2.2 (a)). Figure 2.2 (b) shows a dipolar source in the apical dendrite of a single pyramidal cell. In reality, the dipolar source activity does not come from a single neuron, but a concentrated collection of such activities in the cortical region. Studies indicate that the primary dipole represents up to $10^5 \sim 10^6$ neuronal source activities and its strength ranges from the 10 nAm to 100 nAm, depending on the strength of each source. It is this equivalent current dipole (ECD) that forms the basis of EEG and MEG source analysis. The dipolar sources are rooted in the layer of gray matter and usually oriented (but not always) normal to the cortical surface. Because of the folding anatomy of cortex, the normal direction to the surface can be purely radial, purely tangential or mixture of two orientations with respect to the head surface (Figure 2.2 (c)). The current dipole source is then defined in terms of its position, orientation, and strength. The mathematical dipole in Eq.(2.2) has these components, i.e., source position x_0 and source moment M_0, that represents source direction and strength.

2.3 Modeling of Volume Conductor

Depending on the requirement on accuracy, computational cost and application, a specific volume conductor can be modeled for forward and inverse analysis. In addition, the specific model requires a corresponding numerical method. There is a wide range of modeling approaches including multi-layer sphere models[47], the boundary element

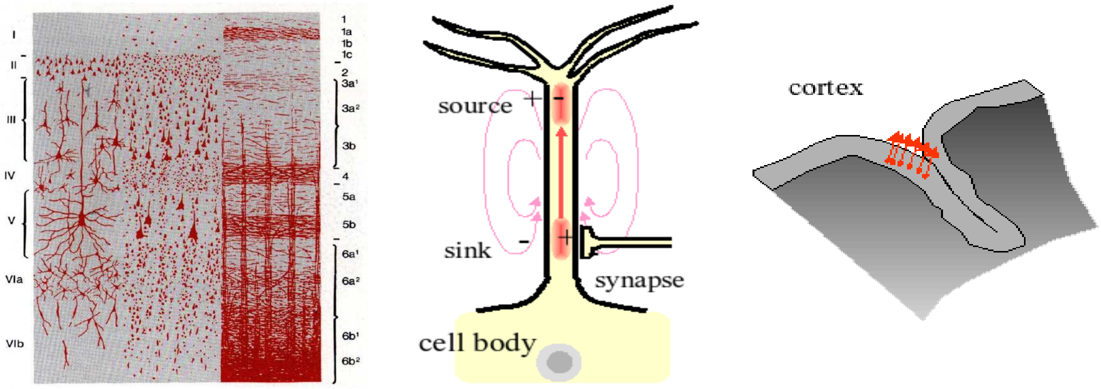

(a) (b) (c)

Figure 2.2. Dipole model of neuronal activity. (a) Structure of cerebral cortex. Pyramidal cells (regions III and IV) are responsible for the dipolar current source activity. The diagram is adapted from [1]. (b) Generation of dipolar source at the postsynaptic junction. One junction plays as a source and the other as a sink. (c) Dipole vectors aligned along the cortex column.

method (BEM) [36, 48, 51], the finite difference method [52] and the finite element method (FEM) [7, 53–56, 68] (Figure 2.3). These conductor models are based on how we model the head geometry on the one hand and how we define the head tissue inhomogeneity on the other hand. This accuracy of the head volume conductor model plays a significant role in the solution procedure, computational cost, and the solution accuracy [7, 36, 46]. Due to the simplification of its symmetry, a sphere model of the head has an analytical solution and hence low computational cost. However, the geometric simplification causes inaccurate results [46]. Recent growth in imaging technologies such as MRI and CT make it possible to create realistic head models. The boundary element method requires models based only on the surfaces and the resulting solutions are more accurate than those of the sphere model. However, the BEM requires a higher computing power due to the nature of this model, i.e., solving a large linear system of equations. The FEM offers the most flexibility in assigning both accurate geometry and detailed conductivity attributes to the model at the cost of both creating and computing on the resulting geometric model. The use of recently developed transfer matrix (or lead field bases) approaches [6, 56, 57] and advances in efficient FEM solver techniques for source analysis [58] drastically reduces the complexity of the computations so that the main disadvantage of FEM modeling no longer exists.

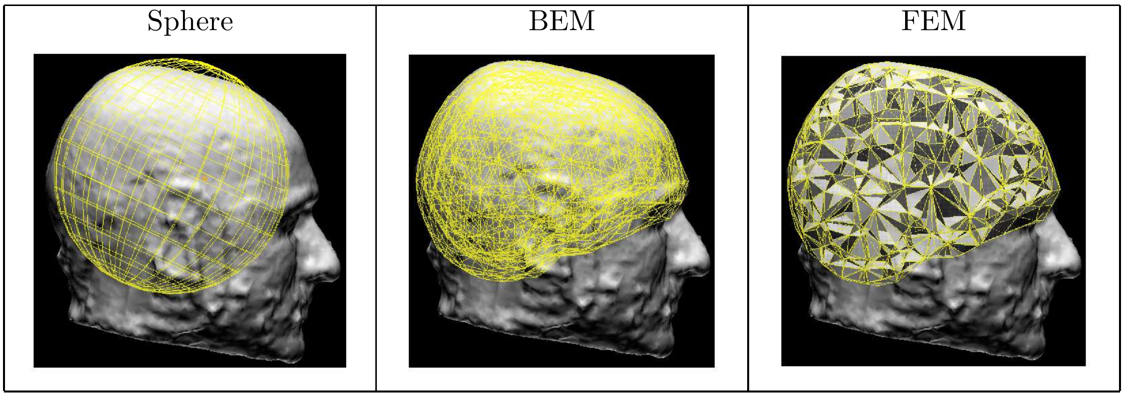

Sphere BEM FEM

Figure 2.3. Volume conductor modeling of human head depending on how to model head geometry, how to assign tissue conductivity, and how to solve the forward problem numerically. The volume conductors of sphere model, boundary element model, and finite element model are shown with the real head image.

2.3.1 Realistic Geometric Modeling

Current medical imaging techniques contribute to create an accurate volume conductor model and there are advantages and disadvantages to each modality. Both Magnetic Resonance (MR) and Computed Tomography (CT) imaging provide the anatomical information for the brain, the cerebrospinal fluid (CSF), the skull, and the scalp [7, 35, 36, 68]. MRI has the advantage of obtaining details of soft tissues such as gray and white matters, while CT provides better definition of hard tissues such as bone. MRI is completely safe for human use; however, CT is not justified for routine physiological studies in healthy human subjects because of the exposure to radiation. As an alternative, proton-density (PD) weighted MRI enables the segmentation of the inner skull surface. A combination of T1-weighted, which is well suited for the identification of soft tissues (scalp, brain) and PD-weighted MRI appropriately segment head compartments [3]. In addition, this approach leads to an improved modeling of the skull thickness over standard (T1) weighted MRI, an important parameter for a successful application of the forward and the inverse source analysis.

2.3.2 Tissue Conductivity

Determining the second component of the volume conductor model, the conductivities of the tissues, does not have the support of a technology as capable as MRI or CT. The electric conductivities of the head tissues vary across individuals and within the same individual due to variations in age, disease state and environmental factors. First attempts to measure the conductivities of biological tissues were *in vitro*, often using samples taken from animals [69]. The conductivity of human CSF has been measured by Baumann *et al* [37]. Latikka *et al* [38] investigated the conductivity of living intracranial tissues from nine patients under surgery. As the skull has considerably higher resistivity than the other head tissues—and thus could be expected to play a bigger role in the electric currents in the head—much attention focused on determining its conductivity. Rush and Driscoll measured impedances for a half-skull immersed in fluid[39, 70] and since then the brain:skull conductivity ratio of 80 has been commonly used in bioelectric source analysis [40]. A similar ratio of 72, averaged over six subjects, was reported recently using two different *in vivo* approaches[41], one method using the principles of electrical impedance tomography (EIT) and the other method based on an estimation through a combined analysis of the evoked somatosensory potentials/fields (SEP/SEF). However, those results remain controversial because other studies have reported the following ratios: 15 (based on *in vitro* and *in vivo* measurements)[42], 23 (averaged value over nine subjects estimated from combined SEP/SEF data) [43], 25 (estimated from intra- and extra-cranial potential measurements) [44], and 42 (averaged over six subjects using EIT measurements) [45]. Presumably these wide variations are due to the inter-personal difference, temporal variation, or disease states. Since the EEG forward problem has a strong dependency on the tissue conductivity, it is necessary to resolve such variations by customizing conductivities for each individual.

Table 2.1 shows the impact of incorrect skull conductivity on source localization error in a simulation study, performed with reference EEG data (SNR of 25dB). The data was created with two somatosensory sources and a skull conductivity of 1/25 of brain. The EEG data was fitted by the dipole fit method with a fixed skull conductivity values ranging from the 1/80 to 1/5 of brain. The results in Table 2.1 show the effects of an erroneous choice of the brain:skull conductivity ratio (80, 40, 15, 10, 8, 5) on the localization accuracy in comparison to the localization errors caused just by the the addition of noise when using the correct brain:skull ratio of 1:25. Incorrect skull conductivity within the source localization caused localization errors of 12-15 mm compared to 2-7.5 mm with the correct values.

Table 2.1. Localization error (mm) for a fixed brain:skull conductivity ratio using the simulated reference SEP data with a SNR ratio of 25dB.

σ_{brain}	tangential	source	radial	source
to σ_{skull}	right	left	right	left
80	12.70	10.82	13.13	15.23
40	3.76	11.23	7.51	8.28
25	2.01	3.33	7.38	7.51
15	3.18	10.73	6.74	10.04
10	2.25	10.72	7.10	10.86
8	7.10	10.72	10.09	10.77
5	3.33	20.53	9.99	18.13

2.4 Brain Source Localization Method

EEG and MEG brain source localization is inherently an inverse problem. That is, it aims to reconstruct the neural activities in the human brain using electric potential differences measured at the head surface and/or magnetic fields measured at sensors just above the head. In neuroscience, the inverse source localization provides source information of event-related brain activities such as SEP (Somatosensory Evoked Potential), VEP (Visual Evoked Potential), and AEP (Auditory Evoked Potential). The source information includes physical location of the source in the brain and the temporal changes of source orientation and magnitude. Clinically, the source localization can provide the geometric origin of brain functional abnormality such as epilepsy or Alzheimer's and Parkinson's diseases. Often combined with information from other functional modalities such as fMRI and PET, the bioelectric source information can assist neurologists to determine the origin of the abnormality and thus to plan further treatments such as embedding intracortical electrodes or open skull surgery. Accurate geometric source information definitely reduces the cost and complexity of pre-surgical planning.

Diverse source reconstruction methods have been developed during the past decade and these methods fall into two categories [65]. The first category is the parametric approach. It assumes that a few of current dipoles represents the source and needs to be estimated in terms of location and moment. This formulation leads to a nonlinear inverse problem since the forward solution depends nonlinearly on the source location and linearly on the source moment. In this category, there are three major solution methods, least squared error estimation [5], beamformer [71], and the multiple signal classification (MUSIC) [72]. The least squared error approach is to estimate the source parameters by minimizing a cost function defined as the difference between the forwardly simulated data and the actual measured data. The beamforming method is to spatially decompose the sensory signals into the data originated from a region of source activities and data from elsewhere. The MUSIC method is to extract subspaces that represent the signal and the noise by means of eigenvectors of measured data. The second category is the imaging approach. It assumes that the source is intracellular and normally constrained to the cortex surface. Then, the inverse process is to reconstruct only the time dependant source strength over the entire cortex or some surface surrounding the cortex. Since the only parameter to be searched is the source strength, the forward problem is linear. However, it is also a physically ill-posed problem that depends sharply on input to noise and requires some form of constraint or stabilizing (regularization).

2.5 Combined Modality of EEG and MEG

As mentioned in Section 2.1, EEG source analysis is strongly sensitive to tissue conductivity, and MEG analysis is not as sensitive to the conductivities. Figure 2.4 shows a simulation result of EEG and MEG dipole fit, respectively, for quasi-tangential and quasi-radial sources with a realistic FEM head model. From this, it is clear that the MEG source localization does not depend significantly on the skull conductivity, while EEG localization depends heavily on the conductivity. In the face of typical tissue conductivity variation, this benefit of MEG based approaches encourages the use of MEG measurement for more accurate source localization even though the MEG systems are much more expensive than EEG systems. Moreover, the MEG has a poor sensitivity to radial source components. When the source is mainly tangential, the MEG has a definite advantage over the EEG. When the source is purely or partially radial, the results of MEG source reconstruction need to be compensated by supplementary information for accurate source reconstruction. As for the radial sources, the EEG has the same sensitivity as the tangential sources. Accordingly, recent research tends to report the combined analysis of EEG and MEG, which compensates each other's weakness and maximize the solution accuracy.

2.6 Optimized Volume Conductor

Although it is feasible to have a subject specific head geometry, it is not usually practically possible to obtain a customized tissue conductivity for each subject. This

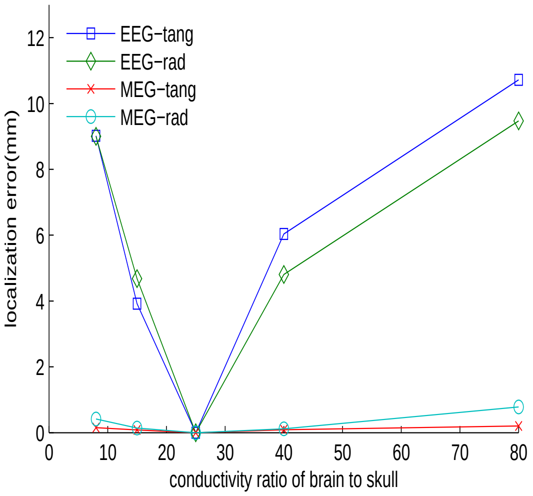

Figure 2.4. Localization error with respect to skull conductivity, given EEG and MEG data. x axis represents the conductivity ratio between skull conductivity ratio to brain (0.33 S/m). Source localization was performed by dipole fit method with simplex optimizer. The correct skull conductivity ratio is 25.

is partly due to the fact that the tissue conductivity is not measurable with current medical modalities. Mere assumption of the conductivity from the reported values can significantly deteriorate the solution accuracy in source analysis. The recent study of Gutiérrez *et al* [73] took the conductivity variation into consideration during the source analysis and used the maximum-likelihood and maximum a posterior(MAP) techniques to estimate the tissue conductivity ratio and the source parameter simultaneously with four layer sphere model. Gutiérrez' *et al*'s approach to resolve conductivity uncertainty was not able to generate an optimized volume conductor model at full scale because of the unrealistic sphere head model used in their study. Therefore, it is necessary to identify critical parameters related to the solution accuracy and to customize those parameters to each individual case. The outcome of the customized parameters and the volume conductor model could improve the quality of routine clinical evaluations. The core of this thesis is to seek methods to customize tissue conductivities for each individual by means of the experimental data from the EEG and the MEG modalities. Such an approach can generate a subject-specific optimized volume conductor model with regard to the tissue conductivities and the head geometry. Practically, combined with the general advantages of a realistic head geometry model, the success of the conductivity optimization suggests a three step procedure for cognitive and clinical applications. First, one could construct a realistic FEM head model from individual T1- and PD-MR images. Second, one could collect and use ERP (Event Related Potential) such as SEP/SEF data of the subject to create a customized volume conductor model that would be optimized for realistic conductivity values together with the realistic FEM geometry. Third, with this volume conductor model in place, recorded potentials from more complex and clinically interesting sources could drive the inverse source localization. In the clinical situation requiring an accurate source localization, this customized conductor model could play an important role in increasing the localization accuracy.

CHAPTER 3

FINITE ELEMENT METHOD IN BIOELECTRIC PROBLEM

As described in the Section 2.3, the FEM volume conductor model has the benefits over other conductor models in terms of flexible accommodation of realistic head geometry and inhomogeneous tissue conductivity. In this chapter, the bioelectric problem is reformulated to a form compatible with the finite element method.

3.1 FEM Formulation of EEG/MEG Forward Problem

We defined EEG forward problem by the quai-static Maxwell equation in Chapter 2.1,

$$\begin{aligned} \nabla \cdot (\sigma \nabla \Phi) &= \nabla \cdot \mathbf{j}^p \text{ in } \Omega, && (3.1)\\ \sigma \frac{\partial \Phi}{\partial \mathbf{n}} &= 0 \text{ on } \Gamma = \partial\Omega && (3.2)\\ \mathbf{j}^p &= \mathbf{M}_0 \; \delta(\mathbf{x} - \mathbf{x}_0), \end{aligned}$$

where $\mathbf{j}^p$ is the primary current source, Φ is an electric potential distribution in the head domain (Ω), σ is the electric tissue conductivity, Γ is the homogeneous Neumann boundary on the head surface, $\mathbf{n}$ is the surface normal, $\mathbf{x}_0$ is a dipole location, and $\mathbf{M}_0$ is a dipole moment defined by a dipole strength and a direction [48, 67].

The mathematical representation of the EEG forward problem must be reformulated to solve using the numerical approximation method of FEM. For this, we use standard piecewise linear basis functions $\varphi_i(\mathbf{x}) = 1$ for $\mathbf{x} = \xi_i$, where ξ_i is the i-th FE node, and $\varphi_j(\mathbf{x}) = 0$ for all $j \neq i$. The potential is projected into the FE space, i.e., $\Phi(\mathbf{x}) \approx \Phi_h(\mathbf{x}) = \sum_{j=1}^{n} \varphi_j(\mathbf{x}) \underline{u}_j$, where n is the number of FE nodes. Standard variational and FE techniques for equations (3.1) yield the linear system

$$\begin{aligned} K \cdot \underline{u} &= \underline{j} \\ K_{ij} &= \int_\Omega < \nabla\varphi_i, \sigma\nabla\varphi_j > \mathrm{d}x, \; 1 \leq i, \; j \leq n, && (3.3)\\ \underline{j} &= \int_\Omega (\nabla \cdot \mathbf{j}^p) \; \varphi_j \; \mathrm{d}x, \end{aligned}$$

where K is the stiffness matrix (n×n), $\underline{u}$ the potential coefficient vector for Φ_h (n×1), $\underline{j}$ the primary source right-hand-side vector (n×1), and $< \cdot, \cdot >$ the scalar product [5, 74].

Based on the quasi-static Maxwell equations in Chapter 2.1, we also defined the primary magnetic flux, Ψ_{pri}, and the secondary magnetic flux, Ψ_{sec}, for MEG forward problem,

$$\Psi_{pri} = \frac{\mu}{4\pi} < \mathbf{M}_0, \mathbf{C}(\mathbf{x}_0) > \tag{3.4}$$

$$\Psi_{sec} = -\frac{\mu}{4\pi} \int_{\Omega} < \sigma(\mathbf{y}) \nabla \Phi(\mathbf{y}), \mathbf{C}(\mathbf{y}) > d\mathbf{y}, \tag{3.5}$$

where $\mathbf{C}(\mathbf{y}) = \oint_{\gamma} \frac{1}{|\mathbf{x}-\mathbf{y}|} d\mathbf{x}$.

For the MEG forward problem, the primary magnetic flux in Eq. (3.4) can be easily evaluated analytically when the integration of $\mathbf{C}$ on the coil geometry is computed numerically. The secondary magnetic flux in Eq. (3.5) can be represented by means of FEM approach as follows:

$$\begin{aligned} S \cdot \underline{u} &= \underline{\Psi}_{sec} \\ S_{ij} &= -\frac{\mu}{4\pi} \int_{\Omega} < \sigma \nabla \varphi_j, \ \mathbf{C}_i > dx, \ 1 \leq j \leq N, \\ \underline{\Psi}_{sec} &= -\frac{\mu}{4\pi} \int_{\Omega} < \sigma \nabla \Phi_h, \mathbf{C}_i > dx, \ 1 \leq i \leq M, \end{aligned} \tag{3.6}$$

where S is the secondary flux matrix (m×n), $\underline{\Psi}_{sec}$ is the secondary flux vector (m×1), and m is the number of MEG sensors.

3.2 FEM Dipole Model

One of the key questions for the finite element approach to the bioelectric forward problem is the appropriate treatment of the source singularity introduced into the differential equation by the formulation of the mathematical dipole (2.2). Three different FEM approaches for modeling the source singularity are known from the literature: a subtraction approach[53, 75], a Partial Integration direct method [56], and a Venant direct method [5]. Here we describe each FEM dipole approach.

3.2.1 Full subtraction approach

The subtraction approach [53, 75–77] splits the total potential Φ into two parts,

$$\Phi = \Phi_0 + \Phi_{\text{corr}}, \tag{3.7}$$

where the singularity potential, Φ_0, is defined as the solution for a dipole in an unbounded homogeneous conductor with constant conductivity σ_0. $\sigma_0 \in \mathbb{R}^{3\times 3}$ is the conductivity at the source position, which is assumed to be constant in a non-empty subdomain Ω_0 around $\mathbf{x}_0$, in the following called the *homogeneity condition.* The solution of Poisson's equation under these conditions for the singularity potential

$$\nabla \cdot (\sigma_0 \nabla \Phi_0) = \nabla \cdot \mathbf{j}^p \tag{3.8}$$

can be formed analytically for the mathematical dipole $\mathbf{j}^p = \mathbf{M}_0\, \delta(\mathbf{x}-\mathbf{x}_0)$ in Eq.(2.2) [77] as

$$\Phi_0(\mathbf{x}) = \frac{1}{4\pi\sqrt{\det \sigma_0}} \frac{\langle \mathbf{M}_0, (\sigma_0)^{-1}(\mathbf{x}-\mathbf{x}_0)\rangle}{\langle (\sigma_0)^{-1}(\mathbf{x}-\mathbf{x}_0), (\mathbf{x}-\mathbf{x}_0)\rangle^{3/2}}. \tag{3.9}$$

Subtracting (3.8) from (2.1) yields a Poisson equation for the correction potential

$$-\nabla \cdot (\sigma \nabla \Phi_{\mathrm{corr}}) = -\nabla \cdot ((\sigma_0 - \sigma)\nabla \Phi_0) \quad \text{in } \Omega, \tag{3.10}$$

with inhomogeneous Neumann boundary conditions at the surface:

$$\langle \sigma \nabla \Phi_{\mathrm{corr}}, \mathbf{n}\rangle = -\langle \sigma \nabla \Phi_0, \mathbf{n}\rangle \quad \text{on } \Gamma. \tag{3.11}$$

The Neumann boundary condition for the correctional potential is not zero at the surface, but the correctional contribution from the infinity unbounded homogeneous medium.

The advantage of (3.10) is that the right-hand side is free of any source singularity, because of the homogeneity condition — the conductivity $\sigma_0 - \sigma$ is zero in Ω_0. Existence and uniqueness of the solution and FE convergence properties are shown for the correction potential in Wolters *et al* [75]. For the numerical approximation of the correction potential, we use the FE method with piecewise linear basis functions φ_i. When projecting the correction potential into the FE space, i.e., $\Phi_{\mathrm{corr}}(\mathbf{x}) \approx \Phi_{\mathrm{corr},h}(\mathbf{x}) = \sum_{j=1}^{N_h} \varphi_j(\mathbf{x}) \underline{u}_{\mathrm{corr},h}^{[j]}$, and applying variational and FE techniques to (3.10) and (3.11), we finally arrive at a linear system [77]

$$K_h \underline{u}_{\mathrm{corr},h} = \underline{j}_{\mathrm{corr},h}, \tag{3.12}$$

with the stiffness matrix

$$K_h^{[i,j]} = \int_\Omega \langle \sigma \nabla \varphi_j, \nabla \varphi_i \rangle dx, \tag{3.13}$$

for $K_h \in \mathbb{R}^{N_h \times N_h}$, and the right-hand side vector $\underline{j}_{\mathrm{corr},h} \in \mathbb{R}^{N_h}$ with entries

$$\underline{j}_{\mathrm{corr},h}^{[i]} = \int_\Omega \langle (\sigma_0 - \sigma)\nabla \Phi_0, \nabla \varphi_i(x)\rangle dx - \int_{\partial\Omega} \varphi_i(x) \langle n(x), \sigma_0 \nabla \Phi_0(x)\rangle dx. \tag{3.14}$$

We then solve for the coefficient vector $\underline{u}_{\mathrm{corr},h} = (\underline{u}_{\mathrm{corr},h}^{[1]}, \ldots, \underline{u}_{\mathrm{corr},h}^{[N_h]}) \in \mathbb{R}^{N_h}$ and, using (3.7), compute the total potential. Drechsler *et al* provided the theoretical reasoning and a validation in a four-compartment sphere model with anisotropic skull for the fact that second order integration is necessary and sufficient for the right-hand side integration in Equation (3.14) [77]. Direct comparisons with the projected subtraction approach have shown that the full subtraction approach is an order of magnitude more accurate for dipole sources close to a conductivity discontinuity [75, 77].

3.2.2 The partial integration direct approach

Multiplying both sides of Equation (2.1) by a linear FE basis function φ_i and integrating over the head domain leads to a partial integration direct approach for the total potential [56, 76, 78] expressed as

$$\int_\Omega \nabla \cdot (\sigma \nabla \Phi)\, \varphi_i dx = \int_\Omega \nabla \cdot \mathbf{j}^p \varphi_i dx.$$

Integration by parts, applied to both sides of the above equation, yields

$$-\int_\Omega \langle \sigma \nabla \Phi, \nabla \varphi_i \rangle dx + \int_\Gamma \langle \sigma \nabla \Phi, \mathbf{n} \rangle \varphi_i d\Gamma = -\int_\Omega \langle \mathbf{j}^p, \nabla \varphi_i \rangle dx + \int_\Gamma \langle \mathbf{j}^p, \mathbf{n} \rangle \varphi_i d\Gamma.$$

Using the homogeneous Neumann boundary condition from Equation (2.1) and the fact that the current density vanishes on the head surface, we arrive at

$$\int_\Omega \langle \sigma \nabla \Phi, \nabla \varphi_i \rangle dx = \int_\Omega \langle \mathbf{j}^p, \nabla \varphi_i \rangle dx = \langle \mathbf{M}_0, \nabla \varphi_i (\mathbf{x}_0) \rangle.$$

Setting $\Phi(\mathbf{x}) \approx \Phi_h(\mathbf{x}) = \sum_{j=1}^{N_h} \varphi_j(\mathbf{x}) \underline{u}_h^{[j]}$, leads to the linear system

$$K_h \underline{u}_h = \underline{j}_{\mathrm{PI},h}, \tag{3.15}$$

with the same stiffness matrix as in (3.13) and the right-hand side vector $\underline{j}_{\mathrm{PI},h} \in \mathbb{R}^{N_h}$ with entries

$$\underline{j}_{\mathrm{PI},h}^{[i]} = \begin{cases} \langle \mathbf{M}_0, \nabla \varphi_i (\mathbf{x}_0) \rangle & \text{if } i \in \textsc{NodesOfEle}(\mathbf{x}_0), \\ 0 & \text{otherwise.} \end{cases} \tag{3.16}$$

The function $\textsc{NodesOfEle}(\mathbf{x}_0)$ determines the set of nodes of the element which contains the dipole at position $\mathbf{x}_0$. Note that while the right-hand side vector (3.14) is fully populated, $\underline{j}_{\mathrm{PI},h}$ has only $|\textsc{NodesOfEle}|$ non-zero entries. Here, $|\cdot|$ denotes the number of elements in the set $\textsc{NodesOfEle}$. For the linear basis functions φ_i considered here, the right-hand side (3.16) and thus the computed solution for the total potential in (3.15) will be constant for all $\mathbf{x}_0$ within a finite element. Figure 3.1 shows the schematic plot of the partial integration dipole from a two dimensional finite element problem.

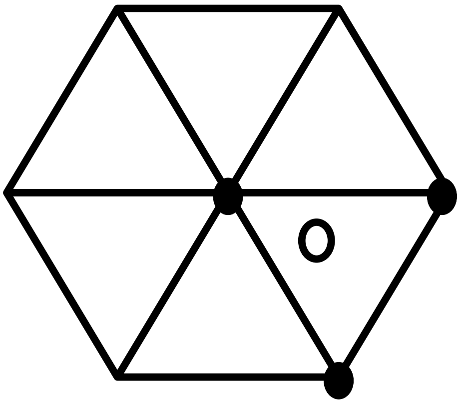

Figure 3.1. Partial integration dipole method. The small circle is the mathematical dipole location. The block dots are the nodes at which the dipole source moment is evaluated.

3.2.3 The Venant direct approach

The Venant dipole approach is based on Venant's principle that the detailed configuration of the applying load (dipole source in our case) does not have a significant influence on the result (forward potentials) when the observation (measurement) is made some distance away from the load. The mathematical dipole at a given location can be distributed to the selected neighboring nodes such that the resulting moment of the distribution becomes the same as that of the original dipole moment. Due to this distribution of the load, it is also called the blurred dipole model. Based on this principle, Buchner *et al* has implemented the mathematical dipole in the finite element space [5]. Detailed derivation is in Appendix B.

With $\Phi(\mathbf{x}) \approx \Phi_h(\mathbf{x}) = \sum_{j=1}^{N_h} \varphi_j(\mathbf{x}) \underline{u}_h^{[j]}$, we can derive the linear system

$$K_h \underline{u}_h = \underline{j}_{\text{Venant},h} \tag{3.17}$$

with the same stiffness matrix as in (3.13). The right-hand side vector $\underline{j}_{\text{Venant},h} \in \mathbb{R}_h^N$ has only C non-zero entries and is determined by

$$\underline{j}_{\text{Venant},h}^{[i]} = \begin{cases} \underline{j}_0^{[c]} & \text{if } c \in \{1, \ldots, C\} : i = \textsc{glob}(c), \\ 0 & \text{otherwise} \end{cases} \tag{3.18}$$

for a source at location $\mathbf{x}_0$. The function GLOB determines the global index i to each of the local indices c. Figure 3.2 shows the schematic plot of the Venant dipole approach.

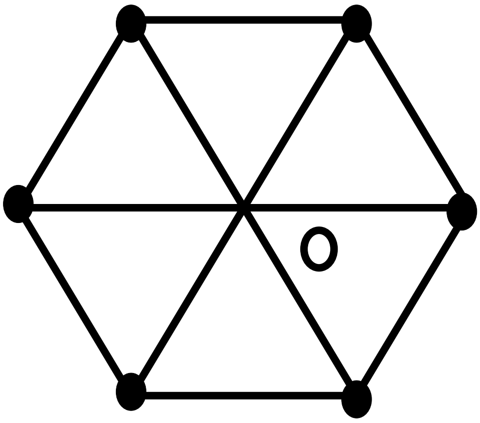

Figure 3.2. Venant dipole approach. The small circle is the mathematical dipole location. The block dots are the nodes where the dipole source moment is distributed.

3.3 FEM Solvers

The computational complexity in solving large system of linear equations derived from the FEM is often represented by a so-called condition number. The solution of hundreds of large scale systems of equations (3.12), (3.15) or (3.17) with the same symmetric positive definite (SPD) stiffness matrix (3.13) is the major time consuming task of the inverse source localization process that requires many calls to solve the forward linear systems of equations. The spectral condition of a SPD matrix, K_h, is equal to

$$\kappa_2(K_h) = \frac{\lambda_{\max}}{\lambda_{\min}}$$

with $\lambda_{\max}$ the largest and $\lambda_{\min}$ the smallest eigenvalues of K_h. The condition number behaves asymptotically as $\mathcal{O}(h^{-2})$ where h is the mesh size and condition numbers of more than 10^7 have been computed for FE problems in EEG and MEG source analysis [68]. Large condition numbers are the reason for slow convergence of common iterative solvers [79, 80] and any effective solution approach for the inverse problem has to minimize the effects of this poor conditioning.

The Preconditioned Conjugate Gradient (PCG) iterative solver shown in Algorithm 1 (see, e.g.,[79–81]) can provide efficient procedures for such problems. Note that, in theory, the convergence speed of the PCG is independent of the right-hand side $\underline{j}_h$ of the linear equation system [79]. A well-defined preconditioner, $C_h \in \mathbb{R}^{N_h \times N_h}$, is able to reduce $\kappa_2(C_h^{-1}K_h)$ for the preconditioned equation system $C_h^{-1}K_h\underline{u}_h = C_h^{-1}\underline{j}_h$. For detailed mathematical discourse, refer to Hackbusch *et al* [79].

Algorithm 1 PCG : $(K_h, \underline{u}_h, \underline{j}_h, C_h, \textsc{accuracy}) \rightarrow (\underline{u}_h)$

```
$\underline{r}_h = \underline{r}_h^0 = \underline{j}_h - K_h\underline{u}_h$
SOLVE $C_h\underline{w}_h = \underline{r}_h$
$\underline{s}_h = \underline{w}_h$
$\gamma^0 = \gamma = \gamma_{\text{OLD}} =< \underline{w}_h, \underline{r}_h >$
while $\left(\gamma/\gamma^0 = \left(\frac{||\underline{r}_h||_{C_h^{-1}}}{||\underline{r}_h^0||_{C_h^{-1}}}\right)^2 = \left(\frac{||K_h\underline{e}_h||_{C_h^{-1}}}{||K_h\underline{e}_h^0||_{C_h^{-1}}}\right)^2 = \left(\frac{||\underline{e}_h^i||_{K_hC_h^{-1}K_h}}{||\underline{e}_h^0||_{K_hC_h^{-1}K_h}}\right)^2 > \textsc{accuracy}^2\right)$ do
  $\underline{v}_h = K_h\underline{s}_h$
  $\alpha = \gamma/ < \underline{s}_h, \underline{v}_h >$
  $\underline{u}_h = \underline{u}_h + \alpha\underline{s}_h$
  $\underline{r}_h = \underline{r}_h - \alpha\underline{v}_h$
  SOLVE $C_h\underline{w}_h = \underline{r}_h$
  $\gamma =< \underline{w}_h, \underline{r}_h >$
  $\beta = \gamma/\gamma_{\text{OLD}}$ , $\gamma_{\text{OLD}} = \gamma$
  $\underline{s}_h = \underline{w}_h + \beta\underline{s}_h$
end while
```

As indicated in Algorithm 1, the PCG method is stopped after the k^{th} iteration if the relative error, i.e., $\underline{e}_h^k = \underline{u}_h^k - \underline{u}_h^*$ in the controllable $K_hC_h^{-1}K_h$-energy norm is below a given ACCURACY. In Chapter 4, we describe three preconditioners for the CG method and compare their performance.

3.4 Brain Source Inverse Problem

As stated earlier, the attempt to identify or reconstruct source parameters that are responsible for a given electric potential distribution or magnetic field distribution is inherently inverse problem. The ill-posed nature of the problem leads to numerical instability, which requires that *a prior* source information and regularization stabilize any solution. Another challenge in solving inverse problem in FEM bioelectric problems is the computational cost, which arises because the inverse solution requires iterative calls to forward simulation. Thus, it is practically important to reduce the computational cost in order to use the FEM approach with high resolution meshes. The recently developed transfer matrix approach (or lead field basis approach) [56, 57] has substantially reduced the computational cost so that, when computed on modern computers, FEM approaches have become feasible.

3.4.1 Transfer Matrix Approach

In general, one is interested in solving for the source parameter from the given electric potential and/or magnetic field distributions at predefined EEG and/or MEG sensor locations. This mean that it is not necessary to solve the FE linear system of equations Eq. (3.3) & (3.6) for $\underline{u}$ at all FE nodes. For EEG based solutions, we can solve for the potential vector u_{EEG} only for those elements at electrode locations, which is much smaller than $\underline{u}$, by the following transfer matrix approach. Define u_{EEG} as the following

$$u_{EEG} = R \cdot \underline{u}, \tag{3.19}$$

where $R((e-1) \times n)$ is a matrix that restricts the potential vector at all FE nodes to the potential vector at the electrode locations (either by a simple restriction or by interpolation, if electrode locations do not directly correspond to FE nodes), e is the number of sensors, and n is the number of FEM nodes. We can rewrite the Eq. (3.19) with Eq. (3.3) as

$$u^{EEG} = R(K^{-1})J = (RK^{-1})J = T_{EEG}J, \tag{3.20}$$

where T_{EEG} is called as the EEG transfer matrix (or lead field basis matrix). With the EEG transfer matrix, T_{EEG}, a simple matrix-vector multiplication yields the electric potentials u_{EEG} at EEG sensor locations from the source J. The EEG transfer matrix equation can be rewritten by multiplying the stiffness matrix K from the right and transposing, resulting in

$$KT_{EEG}^{T} = R^{T} \tag{3.21}$$

and can be solved with a described PCG method such as AMG-CG.

One can also apply the transfer matrix approach to the computation of MEG secondary flux.

$$\underline{\Pi}_{sec} = S \cdot \underline{u} = S(K^{-1}J) = (SK^{-1})J = T_{MEG}J \tag{3.22}$$

Solving the following equation with the PCG method will determine the MEG transfer matrix T_{MEG}.

$$KT_{MEG}^{T} = S^{T} \tag{3.23}$$

3.4.2 Dipole Fit Method

The non-uniqueness of the EEG inverse problem described in Section 2.1 requires a combination of a viable forward problem, anatomical information, and *a priori* constraints on some aspect(s) of the solution. Here, we described a dipole fit procedure that restricts the number of active sources to a small application dependent number, k [82, 83]. In addition, we define a set of r discrete permissable source locations, or an influence source space that is constrained to nodes of the geometric model that lay within the cortical gray matter. Given this source space, the e scalp electrode locations, and a fixed volume conductor, we have used the fast FE forward computation methods in Section 5.2.1 to compute an lead field matrix, L, which maps sources directly to electrode potentials:

$$L \cdot J = \Phi_{sim}, \tag{3.24}$$

where J is a current source vector of dimension $3r \times 1$ defined at the discrete source space and Φ_{sim} is the simulated potential vector of dimensions $e \times 1$. L has dimensions $e \times 3r$ because we do not use the normal constraint, i.e., sources on the discrete source space can have orientations in any direction.

Since the potential depends linearly on the source moment (dipole direction and strength) and nonlinearly on the source location, we used a two phase approach for source localization [5, 84]. We started with k initial source locations and applied a linear least squares fit to the EEG data that determines uniquely the source orientation and strength, J_s ($3k \times 1$). The numerical solver employed a TSVD (Truncated Singular Value Decomposition) with a threshold for the minimization [84], based on a cost function, g_f, that is the L_2 norm of the difference between the simulated potential, Φ_{sim}, and the measured EEG potential, Φ_{EEG} ($e \times 1$):

$$g_f = min \left\| \Phi_{EEG} - \Phi_{sim} \right\|_2 = \underset{J_s}{min} \left\| \Phi_{EEG} - L_s \cdot J_s \right\|_2 \tag{3.25}$$

In this equation, L_s ($e * 3k$) indicates the reduced lead field matrix for the current choice of source locations $s = (s_1, \cdots, s_k)$ with s_i the i-th source location ($1 \leq i \leq k$). The lead field matrix L can be computed by means of the transfer matrix approach described in the previous section.

The following algorithm summarizes the general procedure of the dipole fit method.

- Define the discrete influence space with r nodes.
- Fix the number, k, of sources to be fitted.
- Precompute the lead field matrix, L, with the given conductivity, σ.
- **Repeat:**

  - Allow an optimizer to choose a set of source locations, $s = (s_1, \cdots, s_k)$
  - Compute a cost function, $g_f = min\|\Phi_{EEG} - L_s(\sigma)J_s\|_2$, with respect to source moments, J_s.

- **Until** cost function meets a tolerance criteria or the number of iterations exceeds a limit.
- Accept the source locations as an optimal configuration.

This same approach also applies to reconstructing sources from MEG measurements.

CHAPTER 4

ACCURACY AND RUN-TIME STUDY OF FEM SOLVER AND DIPOLE MODEL

4.1 Introduction

Accuracy and run-time play an important role in medical diagnostics and research as well as in the field of neuroscience. In Electroencephalography (EEG) based source reconstruction, a current distribution in the human brain is localized noninvasively from measured potentials on the head surface (the EEG inverse problem). As part of the reconstruction, numerical modeling techniques are used to simulate head surface potentials for candidate dipolar current sources in the human cortex, the so-called EEG forward problem.

In this chapter, we describe a comprehensive comparison of the efficiency of algebraic multigrid (AMG), incomplete Cholesky (IC) and Jacobi preconditioners for the conjugate gradient (CG) method for iteratively solving the finite element (FE) method based EEG forward problem. We also evaluate the interplay of the three solvers with three different dipole source presentation, a full subtraction approach and two direct potential approaches, the Venant and the partial integration method. The examination was performed in a four-compartment sphere model with anisotropic skull layer, where quasi-analytical solutions allowed for an exact quantification of computational speed and numerical error. Specifically-tuned constrained Delaunay tetrahedral FE meshes led to high accuracies for both the full subtraction and the direct potential approaches. Best accuracies were achieved by the full subtraction approach if the homogeneity condition was fulfilled. It is shown that the AMG-CG achieves an order of magnitude higher computational speed than the CG with the standard preconditioners with an increasing advantage as mesh size decreased. Our goal was to broaden the application of accurate and fast high-resolution FE volume conductor modeling in source analysis routine by providing objective comparisons of candidate numerical methods.

The following subsections summarized the three preconditioners (Jacobi, IC, and AMG) used in this study.

4.1.1 Jacobi Preconditioning

The condition number of a symmetric matrix K_h is at least as large as the ratio of the maximal and minimal diagonal element, since the smallest(largest) eigenvalue is upper(lower) bounded by the smallest(largest) diagonal element [85] . The diagonal elements corresponding to the head skull compartment are much smaller than those of the outside skull compartment, since the skull conductivity is relatively much smaller than the external boundary at the scalp and the internal boundary at the CSF compartment. With properly scaled large diagonal elements, it is possible to reduce condition number. The Jacobi preconditioner, which takes the diagonal entities of the stiffness matrix, i.e.,

$$C_h := \mathrm{diag}(K_h^{11}, \cdots, K_h^{NN}) \tag{4.1}$$

scales down the stiffness matrix and improves the condition of the system matrix. The scaling preserves the symmetry of K_h, maintaining the SPD character of the matrix. With the simple scaling of the diagonal elements, the condition number of the system may be substantially lowered. For detailed mathematical discourse, refer to Hackbusch *et al* [79].

4.1.2 Incomplete Cholesky Preconditioning

Cholesky decomposition can decompose the the stiffness matrix K_h into $L_h L_h^T$. Due to the large fill-in, the decomposed matrix is not a proper candidate for preconditioning. Alternatively, $C_h := L_0 L_0^T$ by the Incomplete Cholesky decomposition (IC) can be used for the preconditioner, where L_0 is the Cholesky decomposition of the scaled stiffness matrix $\tilde{K}_h$, which is restricted to the same non-zero-pattern as the lower triangular part of $\tilde{K}_h$. However, a problem remains because the decomposition does not gurantee that the result is SPD. In this case, certain preprocessing is required. For a detailed description of the incomplete Cholesky decomposition, refer to Schwarz [81, p.266] and Hackbusch *et al* [79, Theorem 8.5.15 and Remarks 8.5.16,17]. As a result, the incomplete Cholesky preconditioner can be expresse as

$$C_h := L_0 L_0^T \approx K_h, \tag{4.2}$$

where L_0 is a lower triangular matrix computed by the incomplete Cholesky decomposition. Forward and backward substitution solves the preconditioning operation $C\underline{w} = \underline{r}$ in the PCG algorithm.

4.1.3 Algebraic Multigrid Preconditioning

Although the above preconditioners reduce the condition number of the system and make it possible to solve the system practically, the major disadvantage is that the convergence rate, i.e., the factor by which the error is reduced in each iteration, depends on the mesh size h. Finer mesh size means that the convergence rate approaches 1 and a higher number of iterations is required to achieve a given accuracy. It has been proved that the Geometric Multi-Grid (GMG) has an h independent convergence rate ($\rho < 1$) and an h-independent condition number [79] as

$$\kappa_2(C_h^{-1}K_h) \leq \frac{1}{1-\rho^m}, \tag{4.3}$$

with C_h the preconditioner resulting from m steps of the GMG method.

The purpose of MG (Multigrid) is to reduce the low and high frequency components of the error by a combination of a coarse grid correction and a smoothing operation of the error components. Unlike the GMG (Geometric Multigrid), AMG dose not build a coarse grid physically, but operates based on virtual grids. Since it is difficult to construct coarse grids for a head model with conductivity inhomogeneity and anisotropy, AMG give a large benefit over the GMG for a multi-compartment head model. Detailed algorithm and implementation are described by several authors [58, 68, 79, 86–88]. The success of the AMG-CG solver in the FEM has had a great impact on the brain source analysis in terms of reducing computational cost.

4.2 Methods

4.2.1 Validation platform

The numerical examinations of the theory presented above were carried out in a four-layer sphere model with anisotropic skull compartment whose parameterization is shown in Table 4.1 and Figure 4.1. For the choice of these parameters, we closely followed previous studies by Marin *et al* [16] and Hallez *et al* [27]. We assigned isotropic conductivity values to scalp, CSF, and brain compartment, and assigned an anisotropic conductivity value to skull compartment.

Table 4.1. Parameterization of the anisotropic four-layer sphere model with sphere dimension and conductivity.

Medium	Scalp	Skull	CSF	Brain
Outer shell radius	92mm	86mm	80mm	78mm
Tangential conductivity	0.33S/m	0.042S/m	1.79S/m	0.33S/m
Radial conductivity	0.33S/m	0.0042S/m	1.79S/m	0.33S/m

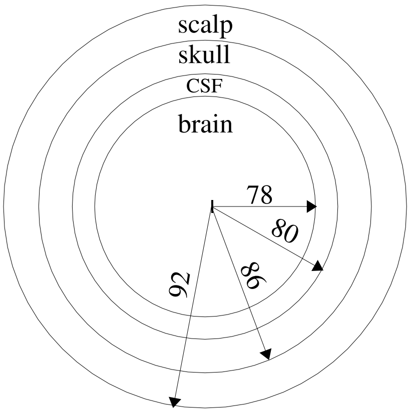

Figure 4.1. Diagram of four compartment sphere model. The dimension of radius is *mm*

Forward solutions were computed for dipoles of 1 nAm amplitude located on the y axis at depths of 0% to 98.7% (in 1 mm steps) of the brain compartment (78 mm radius) using both radial (directed away from the center of the model) and tangential (directed parallel to the scalp surface) dipole orientations. *Eccentricity* is defined here as the percent ratio of the distance between the source location and the model midpoint divided by the radius of the inner sphere (78 mm). The most eccentric source position considered was only 1 mm below the CSF compartment. Figure 4.2 shows the eccentric sources on the center cut plane of the brain compartment. To achieve error measures which were independent of the specific choice of the sensor configuration, we distributed 748 electrodes in a regular fashion over the outer sphere surface. All simulations ran on a Linux-PC with an Intel Pentium 4 processor (3.2GHz) using the SimBio-NeuroFEM software environment [89].

4.2.2 Analytical solution in an anisotropic multilayer sphere model

De Munck and Peters [29] have derived series expansion formulas for a mathematical dipole in a multi-layer sphere model, denoted here as the *analytical solution.* The model

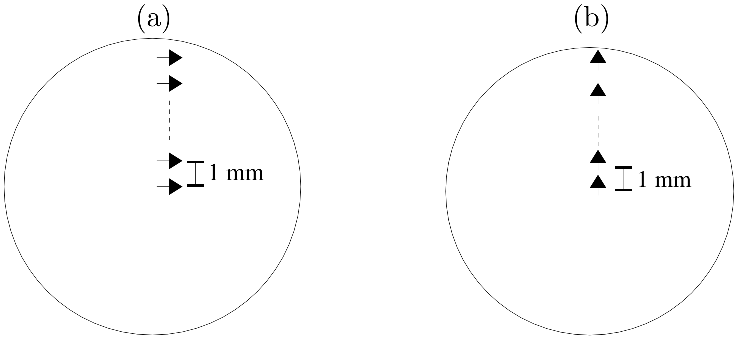

Figure 4.2. (a) Tangential sources on the center cut plane of the brain compartment . (b) Radial sources on the center cut plane of the brain compartment

consisted of S shells with radii $r_S < r_{S-1} < \ldots < r_1$ and piecewise constant radial, $\sigma^{\text{rad}}(r) = \sigma_j^{\text{rad}} \in \mathbb{R}^+$, and tangential conductivities, $\sigma^{\text{tang}}(r) = \sigma_j^{\text{tang}} \in \mathbb{R}^+$, within each layer $r_{j+1} < r < r_j$. It was assumed that the source at position x_0 with radial coordinate $r_0 \in \mathbb{R}$ was in a more interior layer than the measurement electrode at position $x_e \in \mathbb{R}^3$ with radial coordinate $r_e = r_1 \in \mathbb{R}$. The spherical harmonics expansion for the mathematical dipole (2.2) was expressed in terms of the gradient of the monopole potential to the source point. Using an asymptotic approximation and an addition-subtraction method to speed up the series convergence yields

$$\phi_{\mathtt{ana}}(x_0, x_e) = \frac{1}{4\pi}\langle \mathbf{M}, S_0 \frac{x_e}{r_e} + (S_1 - \cos\omega_{0e} S_0)\frac{x_0}{r_0}\rangle$$

with ω_{0e} the angular distance between source and electrode, and with

$$S_0 = \frac{F_0}{r_0}\frac{\Lambda}{(1 - 2\Lambda\cos\omega_{0e} + \Lambda^2)^{3/2}} + \frac{1}{r_0}\sum_{n=1}^{\infty}\left\{(2n+1)R_n(r_0, r_e) - F_0\Lambda^n\right\} P_n'(\cos\omega_{0e}) \quad (4.4)$$

and

$$S_1 = F_1\frac{\Lambda\cos\omega_{0e} - \Lambda^2}{(1 - 2\Lambda\cos\omega_{0e} + \Lambda^2)^{3/2}} + \sum_{n=1}^{\infty}\left\{(2n+1)R_n'(r_0, r_e) - F_1 n\Lambda^n\right\} P_n(\cos\omega_{0e}). \quad (4.5)$$

The coefficients R_n and their derivatives, R_n', were computed analytically and the derivative of the Legendre polynomials, P_n, were determined by means of a recursion formula. We refer to Munck *et al* [29] for the derivation of the above series of differences and for the definition of F_0, F_1, and Λ. Here, it was only important that the latter terms were independent of n and that they could be computed from the given radii and conductivities of layers between source and electrode and of the radial coordinate of the source. The computations of the series (4.4) and (4.5) were stopped after the k-th term if the following criterion was fulfilled

$$\frac{t_k}{t_0} \le \upsilon, \qquad t_k := (2k+1)R'_k - F_1 k \Lambda^k. \tag{4.6}$$

In the following simulations, a value of 10^{-6} was chosen for υ in (4.6). Using the asymptotic expansion, no more than 30 terms were needed for the series computation at each electrode.

4.2.3 Tetrahedral mesh generation.

The FE meshes of the four-layer sphere model were generated by the software TetGen [2] which used a *Constrained Delaunay Tetrahedralization* (CDT) approach [90]. This meshing procedure starts with the preparation of a suitable boundary discretization of the model in which for each of the layers and for a given triangle `edge` length, nodes are distributed in a regular fashion and connected through triangles. This yields a valid triangular surface mesh for each of the layers. Meshes of different layers do not intersect each other. The CDT approach is then used to construct a tetrahedralization conforming to the surface meshes. It first builds a Delaunay tetrahedralization starting with the vertices of the surface meshes. The CDT then uses a local degeneracy removal algorithm combining vertex perturbation and vertex insertion to construct a new set of vertices which includes the input set of surface vertices. In a last step, a fast facet recovery algorithm is used to construct the CDT [90]. This approach is combined with two further constraints to the size and shape of the tetrahedra, the first of which is important for the generation of quality tetrahedra. If R denotes the radius of the unique circumsphere of a tetrahedron and L its shortest edge length, the so-called *radius-edge ratio* of the tetrahedron can be defined as

$$\texttt{radius/edge ratio} = \frac{R}{L}. \tag{4.7}$$

The radius-edge ratio can distinguish almost all badly-shaped tetrahedra except one type of tetrahedra, so-called *slivers*. A sliver is a very flat tetrahedron which has no small edges, but can have arbitrarily large dihedral angles (close to π). For this reason, an additional mesh smoothing and optimization step is required to remove the slivers and improve the overall mesh quality.

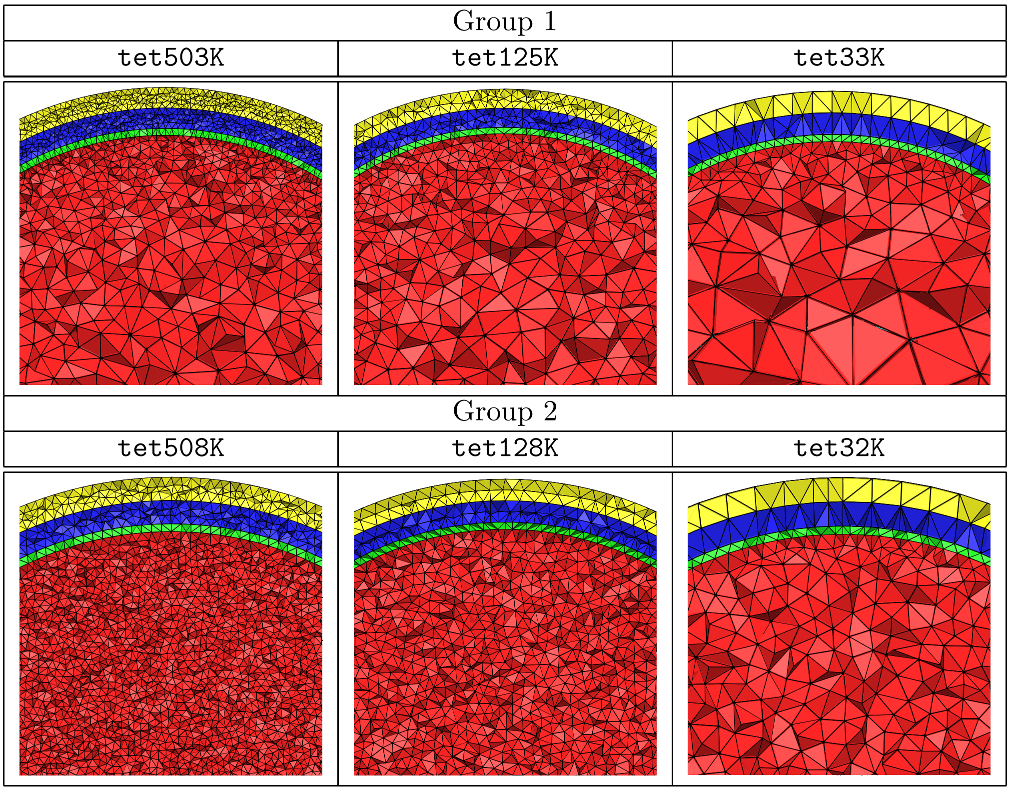

Figure 4.3. Cross-sections of the six tetrahedral meshes of the four compartment sphere model. The corresponding parameterizations of the models are shown in Table 4.2. Visualization was done using the software TetView [2].

A second constraint can be used to restrict the volume of the generated tetrahedra in a certain compartment. We follow the formula for regular tetrahedra:

$$\texttt{volume} = \frac{\sqrt{2}}{12} \cdot \texttt{edge}^3. \tag{4.8}$$

Table 4.2 shows the number of `nodes` and `elements` of the six tetrahedra models used for the solver run-time comparison and accuracy tests. `factor` indicates the ratio of the number of nodes of the most highly resolved to both other models within each group. Additionally, the table contains the chosen `radius/edge ratio` (see Equation (4.7)), the average `edge` length of the four triangular surface meshes, the corresponding `volume` constraints (see Equation (4.8)) for the tetrahedra and the compartments where the volume constraint was not applied. The most highly resolved meshes `tet503K` and `tet508K`, of both groups had approximately the same resolution, while the others were chosen to have a `factor` of 4 coarser resolution with regard to the number of nodes. The meshes of group 1 concentrated the nodes in the outer three compartments because no

Table 4.2. The six tetrahedra models used for the solver time comparison and accuracy tests. The table shows the number of `nodes` and `elements` of each mesh and `factor` indicates the ratio of the number of nodes of the most highly resolved to both other models within each group. Additionally, the chosen `radius/edge ratio` (see Equation (4.7)), the average `edge` length of the four triangular surface meshes, the corresponding `volume` constraint (see Equation (4.8)) and the compartments where the volume constraint was not applied are indicated.

	Group 1			Group 2		
Model	`tet503K`	`tet125K`	`tet33K`	`tet508K`	`tet128K`	`tet32K`
`nodes`	503,180	124,624	32,509	508,435	127,847	31,627
`elements`	3,068,958	733,022	187,307	3,175,737	781,361	190,060
`factor`	1	4.04	15.48	1	3.98	16.08
`radius/edge ratio`	1.0	1.0	1.1	1.0	1.0	1.1
`edge` (in mm)	1.75	2.7	5.2	2.42	3.9	6.87
`volume` (in mm^3)	0.63	2.32	16.57	1.67	6.99	38.21
no volume constraint in	brain	brain	brain	/	/	/

volume constraint was applied for the inner brain compartment, while the nodes in the meshes of group 2 were distributed in a regular way throughout all four compartments. The meshes of group 1 were thus preferentially beneficial to the full subtraction approach, since the entries of the volume integral in Equation (3.14) are zero ($(\sigma(x) - \sigma_0) = 0$ for all x in the brain compartment) so that a coarse resolution can be expected to have no impact on the overall numerical accuracy, but will reduce the computational cost. In contrast, the meshes of group 2 were beneficial to both direct potential approaches. Figure 4.3 shows samples from the six tetrahedra models that were generated using the parameterizations from Table 4.2.

For modeling the skull anisotropy, we built a Smooth Surface Model (SSM) by eroding the outer skull surface by half of its thickness and triangulated the surface with an edge length of 10 mm [75]. Then we took the surface normal as the radial component of the anisotropic tensor and assigned it a conductivity 0.0042 S/m, while the tangential component has 0.042 S/m accordingly.

4.2.4 Error criteria

We compared numerical solutions with analytical solutions using three common error criteria [12, 14, 16, 19, 91]. The *relative (Euclidean) error* (RE) is defined as

$$\mathrm{RE} := \frac{||\underline{\phi}_{\mathtt{num}} - \underline{\phi}_{\mathtt{ana}}||_2}{||\underline{\phi}_{\mathtt{ana}}||_2}, \tag{4.9}$$

where $\underline{\phi}_{\mathtt{ana}}, \underline{\phi}_{\mathtt{num}} \in \mathbb{R}^{\mathrm{m}}$ denote the analytical and the numerical solution vectors, respectively, at the $\mathrm{m} = 748$ measurement electrodes. We furthermore defined

$$\mathrm{RE}(\%) := 100 \cdot \mathrm{RE}, \quad \mathrm{maxRE}(\%) := \max_j \left(\mathrm{RE}(\%)_j\right) \tag{4.10}$$

where j is the source eccentricity. In order to better distinguish between the topography (driven primarily by changes in dipole location and orientation) and the magnitude error (indicating changes in source strength), Meijs et al. [91] introduced the *relative difference measure* (RDM) and the *magnification factor* (MAG), respectively. For the RDM, we can show that

$$\mathrm{RDM} := ||\frac{1}{||\underline{\phi}_{\mathtt{ana}}||_2}\underline{\phi}_{\mathtt{ana}} - \frac{1}{||\underline{\phi}_{\mathtt{num}}||_2}\underline{\phi}_{\mathtt{num}}||_2 = \sqrt{2\left(1 - \cos\angle(\underline{\phi}_{\mathtt{ana}}, \underline{\phi}_{\mathtt{num}})\right)}. \tag{4.11}$$

It therefore holds that $0 \leq \mathrm{RDM} \leq 2$, so that we can furthermore define

$$\mathrm{RDM}(\%) := 100 \cdot \frac{\mathrm{RDM}}{2}, \quad \mathrm{maxRDM}(\%) := \max_j \left(\mathrm{RDM}(\%)_j\right). \tag{4.12}$$

The MAG is defined as

$$\mathrm{MAG} := \frac{||\underline{\phi}_{\mathtt{num}}||_2}{||\underline{\phi}_{\mathtt{ana}}||_2}$$

so that error is minimum at $\mathrm{MAG} = 1$ and we therefore defined

$$\mathrm{MAG}(\%) = |1 - \mathrm{MAG}| \cdot 100, \quad \mathrm{maxMAG}(\%) := \max_j \left(\mathrm{MAG}(\%)_j\right). \tag{4.13}$$

With $\mathrm{maxRE}(\%)^k$, we denote the maximal relative error in percent over all source eccentricities for an accuracy level of $\textsc{accuracy} = 10^{-k}$. The so-called *plateau-entry* for an iterative solver is then defined as the first k at which the condition is true.

$$\frac{\left|\mathrm{maxRE}(\%)^k - \mathrm{maxRE}(\%)^{k+1}\right|}{\mathrm{maxRE}(\%)^{k+1}} < 0.05 \tag{4.14}$$

4.2.5 FEM and solver parameter settings

With the FEM sphere models in hand, we carried out forward computations for each set of parameters. The parameters included FEM solver, relative solver accuracy, dipole source model, source location, source direction, FEM mesh resolution, and mesh constraint of brain. The setup times for the preconditioners were neglected in all calculations of computational cost because this step must be performed only once per head model. The relative solver accuracy was limited to the discrete set of *accuracy levels* ACCURACY $= 10^{-k}$ with $k \in \{0, \ldots, 9\}$. The parameters used in the accuracy and the run-time studies are summarized in the Table 4.3. The total number of FEM forward simulations performed in the study was 84,240.

Table 4.3. Parameters used in the accuracy and the run-time study.

Item		Parameter
Solver	Methods	Jacobi-CG/IC(0)-CG/AMG-CG
	Accuracy	$1 \sim 10^{-9}$ (in step of 10^{-1})
Source	Model	Venant/partial integration/subtraction
	Locations	78 (in steps of 1mm)
	Orientations	radial/tangential
FEM mesh	Resolutions	fine/middle/coarse
	Brain mesh constraints	regular/coarsest possible

4.2.6 Realistic FEM head model

We also built a 3D realistic head model from the MR images of a 32 years old male subject. We used T1- and PD-MRI for registration and segmentation of the image [7, 36, 46, 68, 92], resulting in 4 compartments of scalp, skull, CSF, and brain. We created regular tetrahedral finite element meshes based on the Delaunay criterion [68, 93] by CURRY [94] software. This resulted in models with 245 K nodes and 1,503 K tetrahedral elements with isotropic conductivity assigned to each compartment. Scalp and brain had the same conductivity of 0.33 S/m. Skull had 0.0042 S/m and CSF had 1.79 S/m. Figure 4.4 shows cross sections from the realistic FEM model.

Using the realistic head model, we computed forward potentials numerically on 71 evenly spaced electrodes on the head surface for 96 quasi-tangential and 96 quasi-radial sources located in the brain. We used three dipole models (subtraction, Venant, partial integration) and three FE solvers (AMG-, IC(0)-, Jacobi-CG) with a set of the relative accuracies (from 10^{-9} to 10^{0}). Since it is unable to have an analytic solution for the realistic head model, we used the potentials computed with the relative accuracy of 10^{-9} as the reference potentials used in the error measure of RE. For instance, RE was calculated as

$$\mathrm{RE} := \frac{||\underline{\phi}_{\mathtt{num}} - \underline{\phi}_{10^{-9}}||_2}{||\underline{\phi}_{10^{-9}}||_2}. \tag{4.15}$$

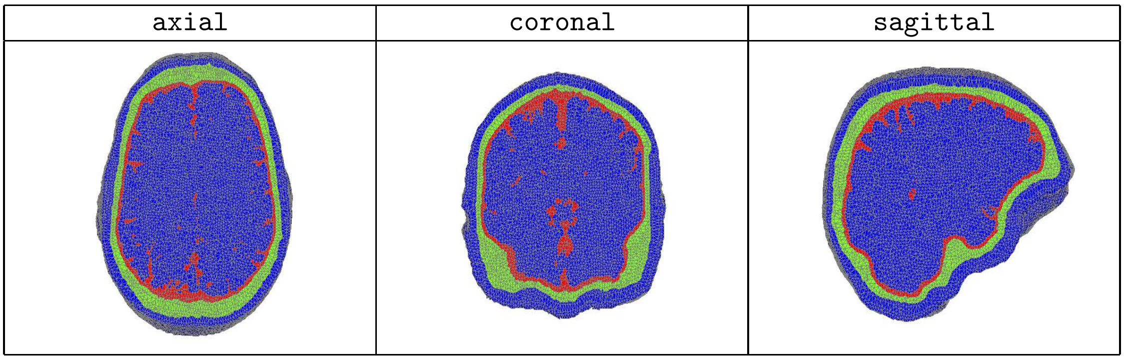

Figure 4.4. Cut plane view of the realistic FEM head model. Colors indicate the four compartments of scalp, skull, CSF, and brain.

4.3 Results

4.3.1 Numerical error versus potential approach

In a first study, we compared the numerical accuracy of the full subtraction approach (Section 3.2.1) with the two direct methods: Venant (Section 3.2.3) and partial integration (Section 3.2.2). Figure 4.5 shows the $RE(\%)$ for the different source eccentricities for the two finest models `tet503K` of group 1 (left) and `tet508K` of group 2 (right) (see Figure 4.3 and Table 4.2) with regard to the full subtraction (top row), the Venant (middle row) and the partial integration approach (bottom row). The results were computed with the AMG-CG and the necessary ACCURACY in Algorithm 1 for the plateau-entry (4.14) is indicated for both source orientation scenarios. In Table 4.4, the maximal errors over all source eccentricities at the AMG-CG plateau-entry (4.14) are shown for all tetrahedra models, both source orientation scenarios, and the three dipole modeling approaches.

Figure 4.5 clearly shows the advantages of the full subtraction approach whose error curves are smooth, while Venant and partial integration show an oscillating behavior at generally larger error values. With RDM and MAG errors below 1% over all source eccentricities and for both orientation scenarios (see Table 4.4), the full subtraction approach performed best for all source eccentricities for model `tet503K` (its mesh resolution was sufficiently high and the FE nodes were concentrated in the compartments CSF, skull and skin), where both direct approaches showed oscillations with a relatively high magnitude. As the results for model `tet508K` showed, the oscillation magnitudes for the direct approaches could be strongly reduced by means of distributing the FE nodes in a regular way over all four compartments, hence decreasing the mesh size in the brain compartment. Nevertheless, even for model `tet508K`, the full subtraction approach was

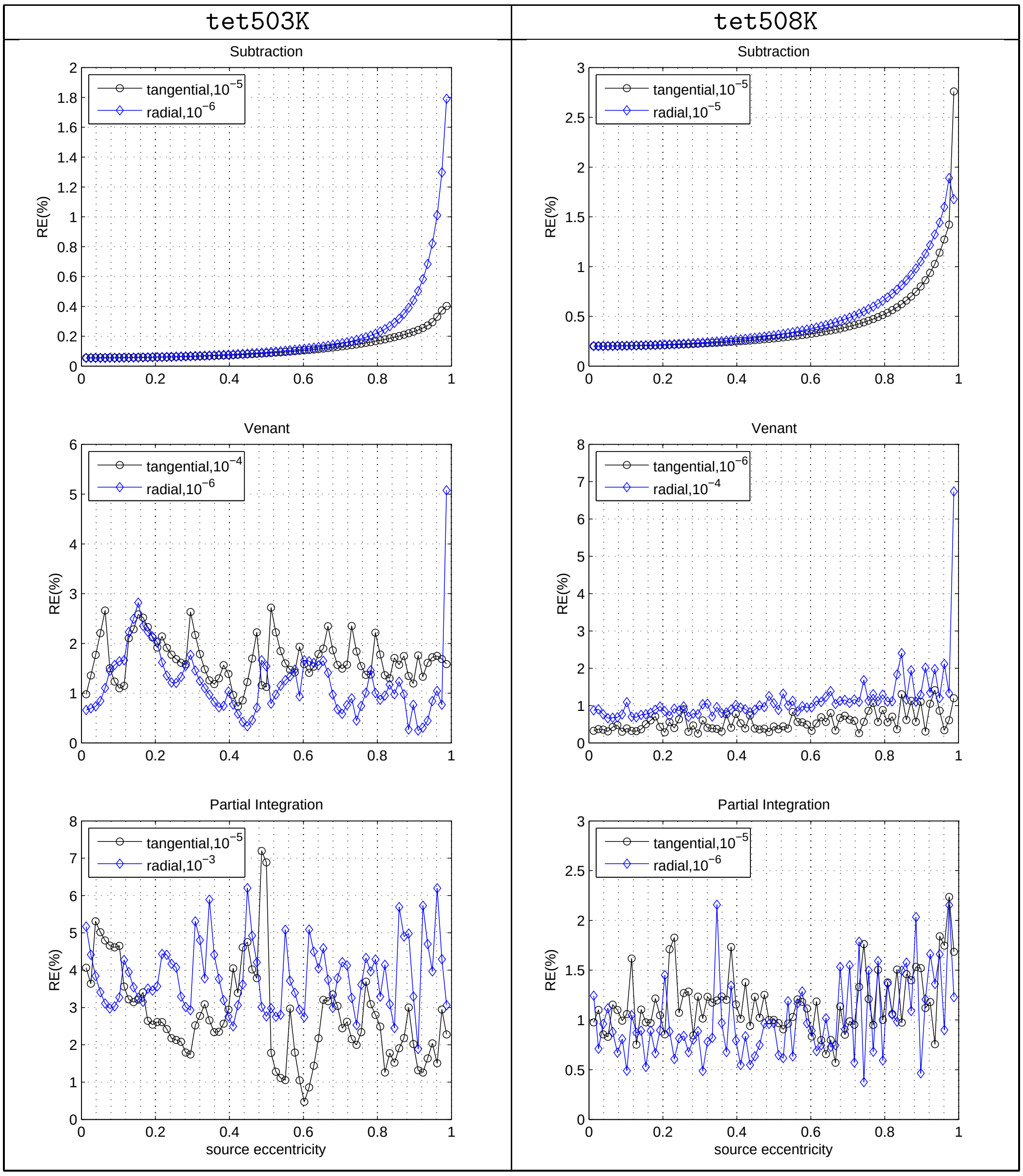

Figure 4.5. $RE(\%)$ versus source eccentricity for the two most highly resolved models `tet503K` of group 1 (left) and `tet508K` of group 2 (right) using the full subtraction (top row), the Venant (middle row) and the partial integration (bottom row) potential approaches. The necessary ACCURACY in Algorithm 1 for the plateau-entry (4.14) of the AMG-CG is indicated for both source orientation scenarios.

the most accurate method for nearly all source eccentricities. It was only outperformed by partial integration for the source that was only 1 mm below the CSF compartment. As both Figure 4.5 and Table 4.4 show, the partial integration approach performed well as long as the mesh was sufficiently fine in the brain compartment. The oscillation

Table 4.4. Values of maxRE(%), maxRDM(%) and maxMAG(%) errors for the full subtraction (Sub), the Venant (Ven) and the partial integration (PI) approach for all six tetrahedra models (see Figure 4.3 and Table 4.2) and both source orientation scenarios at the AMG-CG plateau-entry (4.14).

<table>
<tr><td colspan="10">Group 1</td></tr>
<tr><td colspan="10">Tangential source</td></tr>
<tr><td>Model</td><td colspan="3"><code>tet503K</code></td><td colspan="3"><code>tet125K</code></td><td colspan="3"><code>tet33K</code></td></tr>
<tr><td>Approach</td><td>Sub</td><td>Ven</td><td>PI</td><td>Sub</td><td>Ven</td><td>PI</td><td>Sub</td><td>Ven</td><td>PI</td></tr>
<tr><td>maxRE(%)</td><td>0.403</td><td>2.719</td><td>7.195</td><td>4.192</td><td>2.722</td><td>6.603</td><td>12.543</td><td>10.246</td><td>10.367</td></tr>
<tr><td>maxRDM(%)</td><td>0.202</td><td>1.311</td><td>3.450</td><td>1.322</td><td>1.296</td><td>3.304</td><td>6.020</td><td>4.920</td><td>4.674</td></tr>
<tr><td>maxMAG(%)</td><td>0.149</td><td>1.840</td><td>1.810</td><td>3.217</td><td>1.395</td><td>2.142</td><td>2.863</td><td>3.307</td><td>4.066</td></tr>
<tr><td colspan="10">Radial source</td></tr>
<tr><td>Model</td><td colspan="3"><code>tet503K</code></td><td colspan="3"><code>tet125K</code></td><td colspan="3"><code>tet33K</code></td></tr>
<tr><td>Approach</td><td>Sub</td><td>Ven</td><td>PI</td><td>Sub</td><td>Ven</td><td>PI</td><td>Sub</td><td>Ven</td><td>PI</td></tr>
<tr><td>maxRE(%)</td><td>1.791</td><td>5.077</td><td>6.200</td><td>2.522</td><td>16.867</td><td>5.517</td><td>33.860</td><td>22.810</td><td>19.898</td></tr>
<tr><td>maxRDM(%)</td><td>0.820</td><td>1.408</td><td>2.846</td><td>1.066</td><td>1.662</td><td>2.727</td><td>17.184</td><td>6.730</td><td>9.958</td></tr>
<tr><td>maxMAG(%)</td><td>0.708</td><td>5.035</td><td>3.426</td><td>1.372</td><td>16.804</td><td>1.827</td><td>6.338</td><td>19.344</td><td>7.729</td></tr>
<tr><td colspan="10">Group 2</td></tr>
<tr><td colspan="10">Tangential source</td></tr>
<tr><td>Model</td><td colspan="3"><code>tet508K</code></td><td colspan="3"><code>tet128K</code></td><td colspan="3"><code>tet32K</code></td></tr>
<tr><td>Approach</td><td>Sub</td><td>Ven</td><td>PI</td><td>Sub</td><td>Ven</td><td>PI</td><td>Sub</td><td>Ven</td><td>PI</td></tr>
<tr><td>maxRE(%)</td><td>2.760</td><td>1.414</td><td>2.235</td><td>6.206</td><td>3.457</td><td>3.654</td><td>17.000</td><td>17.977</td><td>11.113</td></tr>
<tr><td>maxRDM(%)</td><td>0.874</td><td>0.599</td><td>0.965</td><td>2.202</td><td>1.665</td><td>1.814</td><td>6.721</td><td>8.715</td><td>5.031</td></tr>
<tr><td>maxMAG(%)</td><td>2.121</td><td>0.753</td><td>1.110</td><td>4.277</td><td>1.011</td><td>1.243</td><td>9.542</td><td>4.474</td><td>4.296</td></tr>
<tr><td colspan="10">Radial source</td></tr>
<tr><td>Model</td><td colspan="3"><code>tet508K</code></td><td colspan="3"><code>tet128K</code></td><td colspan="3"><code>tet32K</code></td></tr>
<tr><td>Approach</td><td>Sub</td><td>Ven</td><td>PI</td><td>Sub</td><td>Ven</td><td>PI</td><td>Sub</td><td>Ven</td><td>PI</td></tr>
<tr><td>maxRE(%)</td><td>1.890</td><td>6.738</td><td>2.157</td><td>7.660</td><td>19.413</td><td>5.054</td><td>21.111</td><td>20.232</td><td>21.000</td></tr>
<tr><td>maxRDM(%)</td><td>0.804</td><td>1.131</td><td>1.051</td><td>1.212</td><td>1.893</td><td>2.141</td><td>10.616</td><td>9.120</td><td>9.188</td></tr>
<tr><td>maxMAG(%)</td><td>1.183</td><td>6.608</td><td>1.101</td><td>7.404</td><td>19.329</td><td>2.836</td><td>8.831</td><td>10.577</td><td>8.617</td></tr>
</table>

magnitudes of the Venant approach were generally even slightly smaller than for the partial integration approach, with only one exception (the result for the radial source 1 mm below the CSF compartment, shown in the middle row of Figure 4.5). The main reason for the outlier was that for the source 1 mm below the CSF, monopoles were positioned in the CSF compartment, which had a strong effect on the MAG for the radially oriented source.

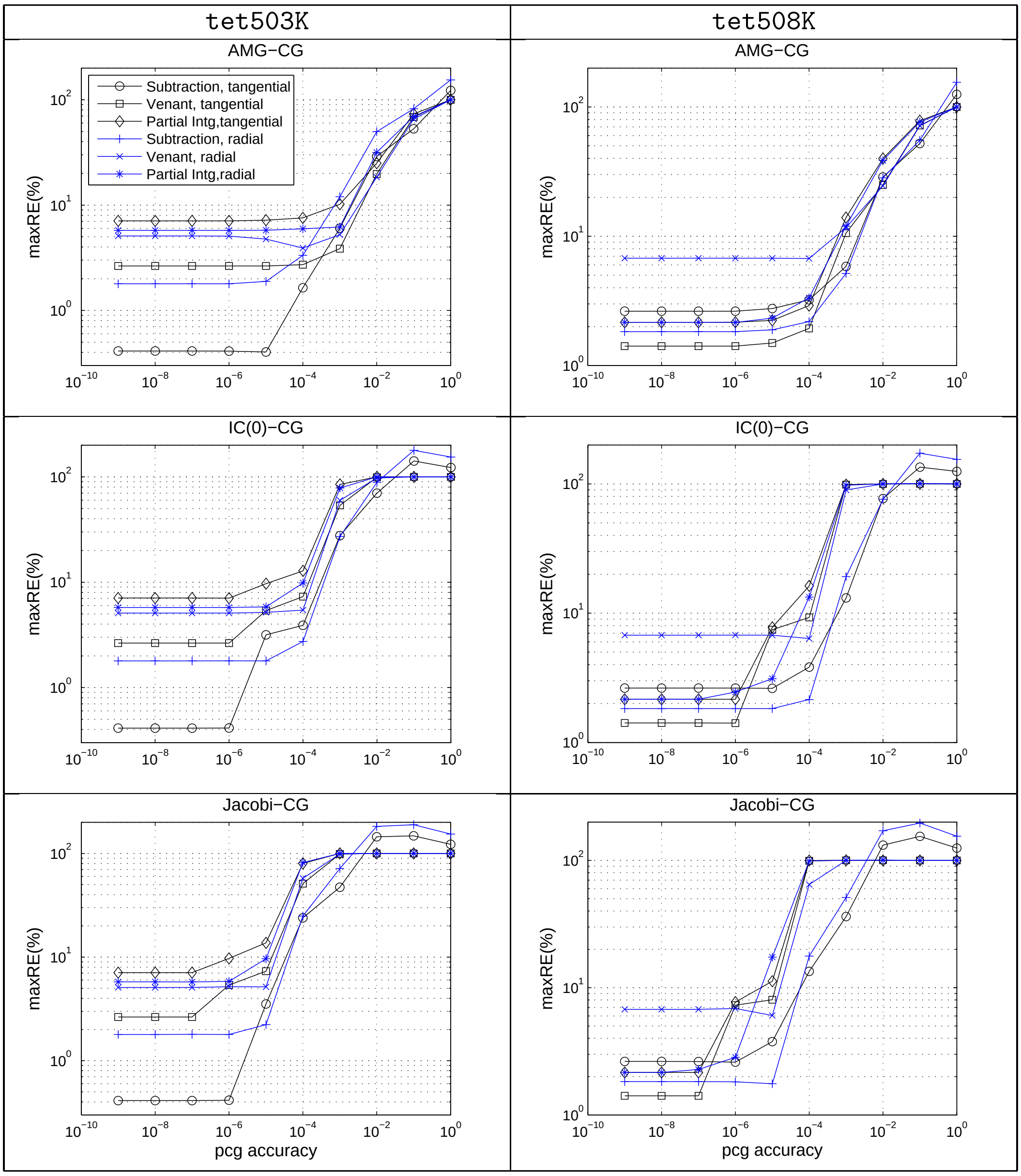

Figure 4.6. maxRE(%) versus PCG solver ACCURACY (see Algorithm 1 and Section 4.2.5) for models `tet503K` of group 1 (left column) and `tet508K` of group 2 (right column) for the AMG-CG (top row), the IC(0)-CG (middle row) and the Jacobi-CG (bottom row). Source orientations and potential approaches can be distinguished by their specific labels. The plot is in log-log scale.

4.3.2 Numerical error versus PCG accuracy

Figure 4.6 shows the numerical error maxRE(%) versus the PCG solver ACCURACY from Algorithm 1 for the discrete set of accuracy levels from 10^0 to 10^{-9}. Results for the high-resolution model `tet503K` of group 1 are shown in the left and from the high-resolution model `tet508K` of group 2 in the right column for the AMG-CG (top row), the IC(0)-CG (middle row) and the Jacobi-CG (bottom row).

Table 4.5. Maximally needed $k \in \{0, \ldots, 9\}$ for a PCG ACCURACY $= 10^{-k}$ for the plateau-entry (4.14) over all three potential approaches.

Group 1						
	Tangential source			Radial source		
Solver	AMG-CG	IC(0)-CG	Jacobi-CG	AMG-CG	IC(0)-CG	Jacobi-CG
tet503K	5	6	7	6	5	6
tet125K	5	5	6	5	5	6
tete33K	4	5	6	3	3	5

Group 2						
	Tangential source			Radial source		
Solver	AMG-CG	IC(0)-CG	Jacobi-CG	AMG-CG	IC(0)-CG	Jacobi-CG
tet508K	6	6	7	6	7	8
tet128K	4	5	6	4	4	6
tete32K	3	5	6	3	4	5

The PCG accuracy measures the error in the solution vector of the FE linear equation system (3.12) (correction potential), (3.15) and (3.17) (total potential). For the full subtraction approach, maxRE(%) was thus not equal to 100 for ACCURACY $= 10^0$ because $\underline{\phi}_{\mathtt{num}}$ is equal to the analytically computed singularity potential $\underline{\Phi}_0$ from Equation (3.9). Because the PCG accuracy is measured in the $K_h C_h^{-1} K_h$-energy norm, the plateau-entry (4.14) differs for different preconditioners C_h. As shown in Figure 4.6 for the high-resolution models and as collected in Table 4.5 for all six tetrahedra models, the maximally needed k (for a PCG accuracy of ACCURACY $= 10^{-k}$) decreased when the preconditioning quality increased (except for the radial source orientation in model `tet503K`, see Fig. 4.6). Furthermore, as Table 4.5 shows, a higher PCG accuracy was needed for the plateau-entry when the mesh resolution increased.

4.3.3 Numerical error versus solver time

In a last study, we compared solver wall-clock time versus numerical accuracy for the three different CG preconditioners: AMG, IC(0), and Jacobi. The time for the setup of the preconditioner was not included because this step was carried out only once per head model.

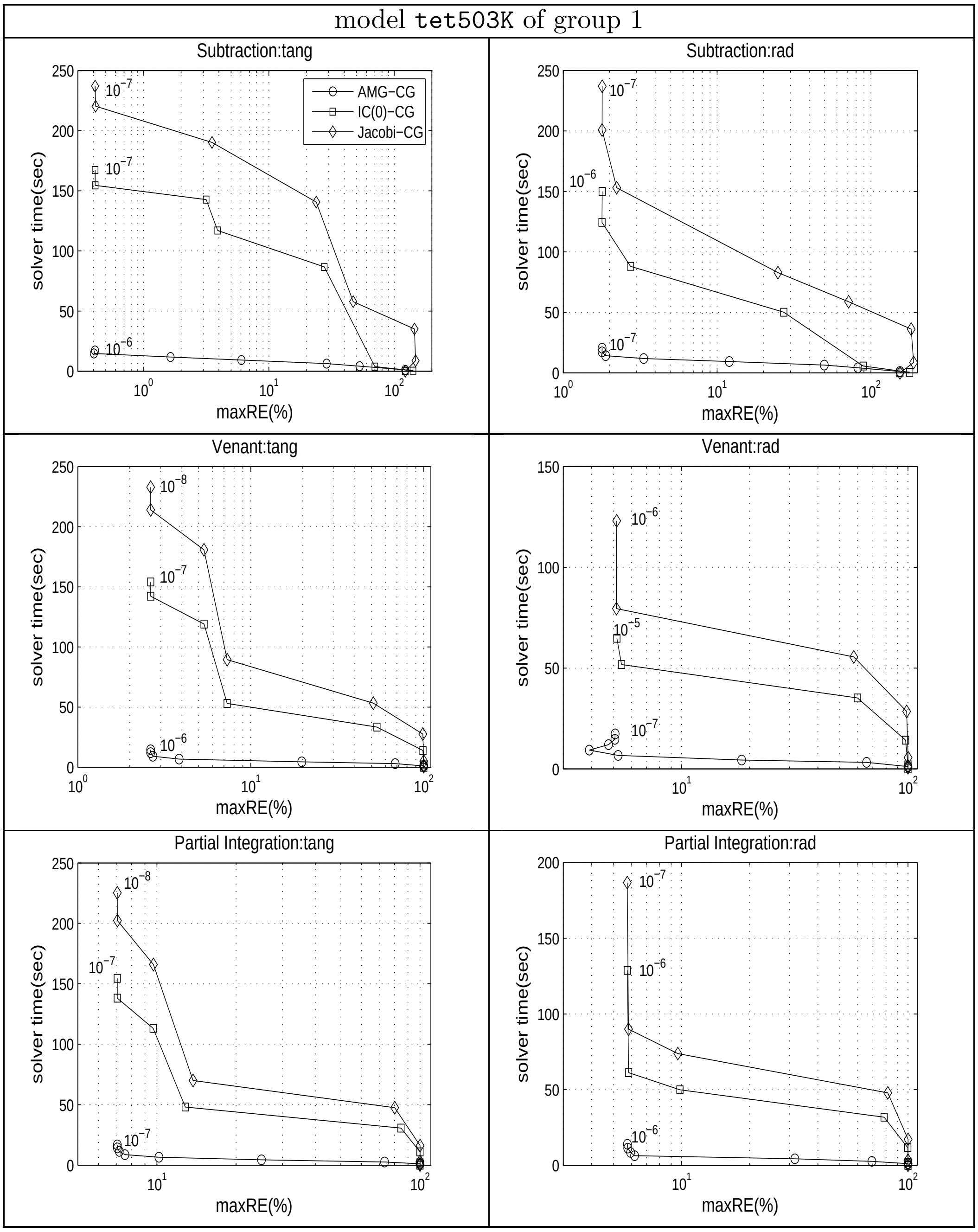

Figure 4.7. Solver time versus maxRE(%) for models `tet503K` of group 1 for tangentially and radially oriented sources for the potential approaches full subtraction (top), Venant (middle), and partial integration (bottom). Results are presented for the three different CG preconditioners AMG, IC(0) and Jacobi. Each marker represents a PCG ACCURACY $= 10^{-k}$ level and the largest examined level is indicated. The x-axis is in log scale.

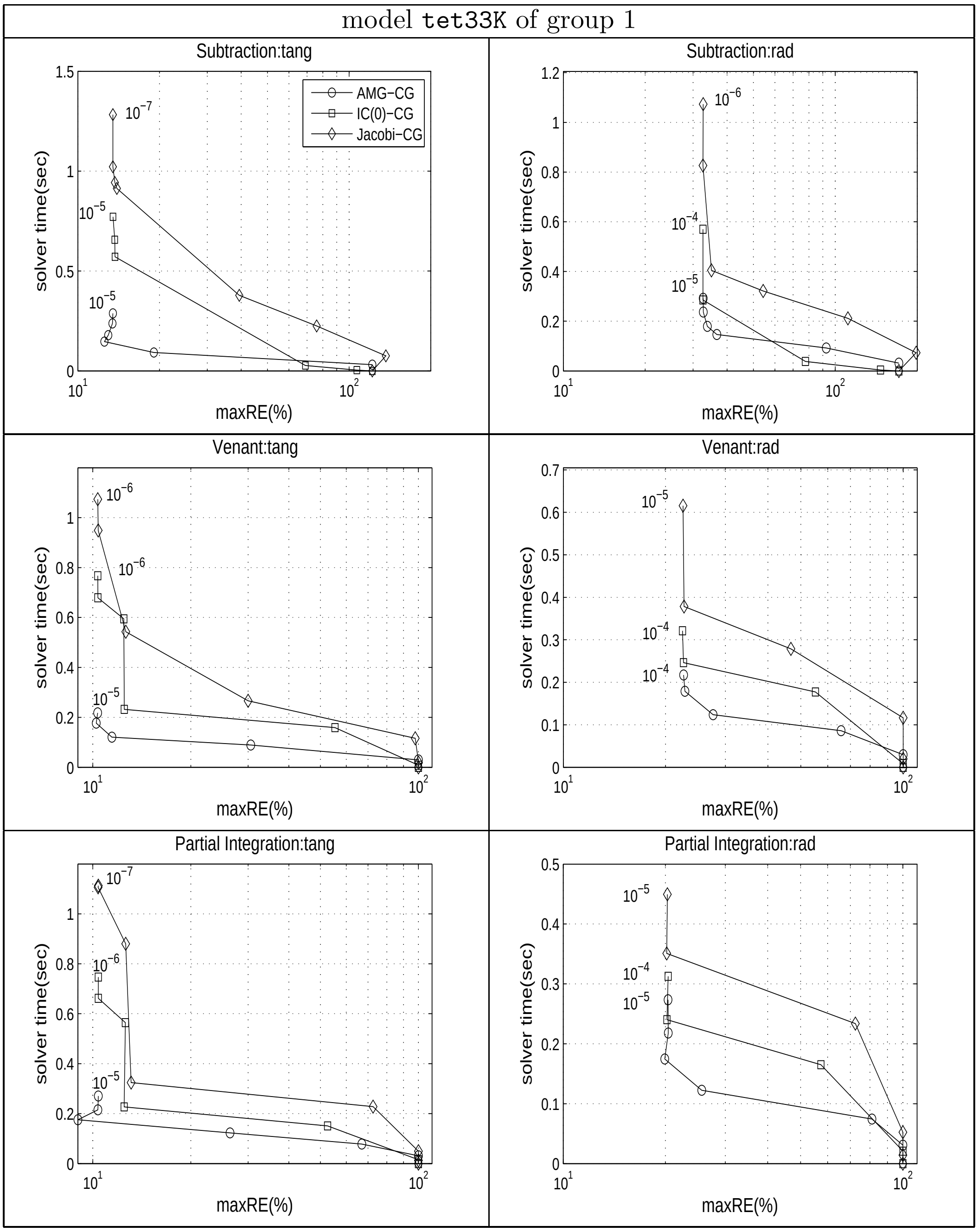

Figure 4.8. Solver time versus maxRE(%) for models `tet33K` of group 1 for tangentially and radially oriented sources for the potential approaches full subtraction (top), Venant (middle), and partial integration (bottom). Results are presented for the three different CG preconditioners AMG, IC(0) and Jacobi. Each marker represents a PCG ACCURACY $= 10^{-k}$ level and the largest examined level is indicated. The x-axis is in log scale.

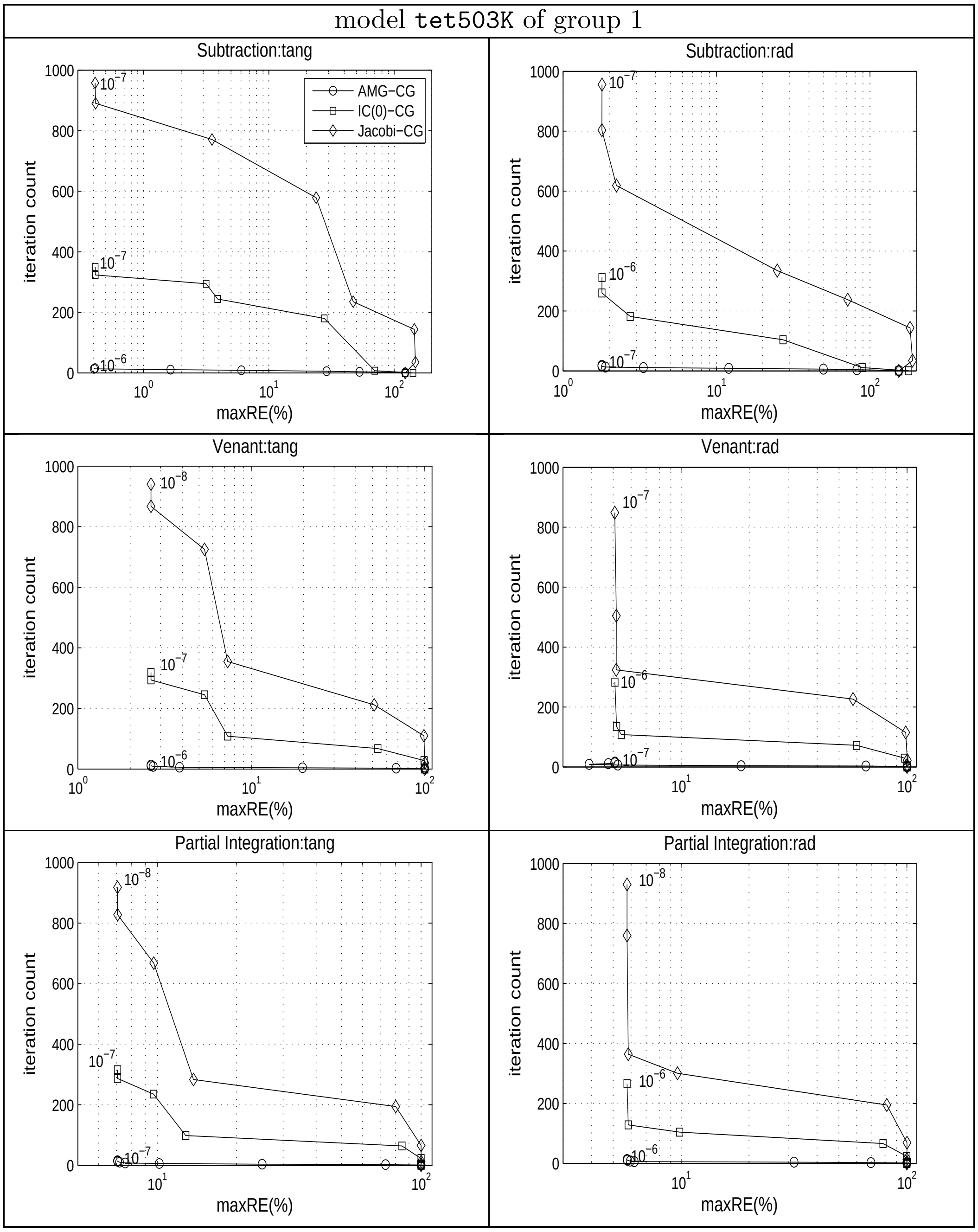

Figure 4.9. Solver iteration count versus maxRE(%) for models `tet503K` of group 1 for tangentially and radially oriented sources for the potential approaches full subtraction (top), Venant (middle), and partial integration (bottom). Results are presented for the three different CG preconditioners AMG, IC(0) and Jacobi. Each marker represents a PCG ACCURACY $= 10^{-k}$ level and the largest examined level is indicated. The x-axis is in log scale.

In Figure 4.7 and 4.8, the solver time is shown versus the maxRE(%) for different levels of PCG accuracy for models `tet503K` and `tet33K` of group 1. In Figure 4.9, the total iteration count of each solver is shown for `tet503K` model. The largest examined PCG ACCURACY level 10^{-k} is indicated in the figure. Please note that this level does not necessarily correspond to the plateau-entry level. In most cases results are presented up to one level higher.

Table 4.6. Average solver time (sec.) and iteration count (iter) over all source eccentricities, source orientations and potential approaches for plateau-entry (4.14). For all tetrahedra models of groups 1 and 2, results are presented for the three different CG preconditioners AMG, IC(0) and Jacobi. The gain factor indicates the performance gain of the AMG-CG relative to the Jakobi-CG.

Group 1						
	`tet503K`		`tet125K`		`tet33K`	
Solver	Time	Iter	Time	Iter	Time	Iter
AMG-CG	12.25	11.20	1.87	9.04	0.18	5.89
IC(0)-CG	112.03	233.43	8.40	128.39	0.45	72.63
Jacobi-CG	167.82	679.43	16.98	414.00	0.76	229.52
gain factor	13.70	60.66	9.08	45.8	4.22	38.97

Group 2						
	`tet508K`		`tet128K`		`tet32K`	
Solver	Time	Iter	Time	Iter	Time	Iter
AMG-CG	9.18	10.40	1.36	7.27	0.15	5.81
IC-CG	72.41	215.05	5.20	98.96	0.31	52.84
Jacobi-CG	99.60	578.04	9.62	331.15	0.47	161.68
gain factor	10.85	55.58	7.07	45.55	3.13	27.83

Table 4.6 contains results for all tetrahedra models of groups 1 and 2, average solver times and iteration counts over all source eccentricities and source orientations and potential approaches for a plateau-entry (4.14). Figure 4.7, 4.8, 4.9 and Table 4.6 clearly show the superiority of the AMG preconditioner over the other approaches. In all cases, even for the low-resolution grids `tet33K` and `tet32K`, the AMG-CG was the fastest solver, followed by the IC(0)-CG and the Jacobi-CG. The main result of Table 4.6 is the so-called *gain factor*, which is defined here as the result (solver time or iteration count) for the Jacobi-CG divided by the result for the AMG-CG. The gain factors clearly showed that the higher the mesh-resolution, i.e., the higher the condition number of the corresponding FE stiffness matrix, the larger the difference in performance between AMG-CG, IC(0)-

CG, and Jacobi-CG. An increasing mesh-resolution led to a strong increase in the number of iterations of IC(0)-CG (factor of 3.2 between `tet503K` and `tet33K` and 4.1 between `tet508K` and `tet32K`) and Jacobi-CG (factor of 3.0 between `tet503K` and `tet33K` and 3.6 between `tet508K` and `tet32K`), while the number of AMG-CG iterations was only slightly increasing (factor of 1.9 between `tet503K` and `tet33K` and 1.8 between `tet508K` and `tet32K`). This clearly shows the stronger h-dependence of the IC(0) and Jacobi preconditioners.

4.3.4 Realistic FEM head model

Figure 4.10 shows the maxRE for the realistic volume conductor model with respect to three solvers and three dipole models both in the quasi-tangentially and quasi-radially oriented positions. The curves in the figure had a plateau like that of sphere model, which means that the higher solver accuracy beyond the plateau entry did not improve the RE accuracy. When the relative accuracies were large, the solver may have been stopped without an iteration and the solution became the initial value of zero. In this case the RE error becomes 100% based on the formula in Eq. 4.9 and Eq. 4.10. That is, the denominator and the nominator in Eq. 4.9 are the same and the RE becomes one and accordingly RE(%) becomes 100%. The partial integration and the Venant dipole approach produced results that fell into this category. Even though the solver may be stopped without an iteration for large errors, the RE could be more than 100% in the subtraction dipole method because the numerical solution involves a solution for the homogeneous infinite medium and a solution for the correction to the bounded medium. The solution process of the correctional potential used the numerical solver and the homogeneous solution used the analytic formula. The analytic portion of the solution was used for the calculation of RE when the solver was stopped without iteration in the large accuracies.

Table 4.7 shows the average solver time and iteration count over all eccentricities with respect to three solvers and three dipole models. The solver time and iteration count in the table was at the relative accuracy in the plateau entry. As in the case of sphere model, the AMG-CG solver was the fastest for all dipole models. The AMG-CG solver was 8.7 times, on average, faster than that of the slowest Jacobi-CG solver for all dipole models and orientations.

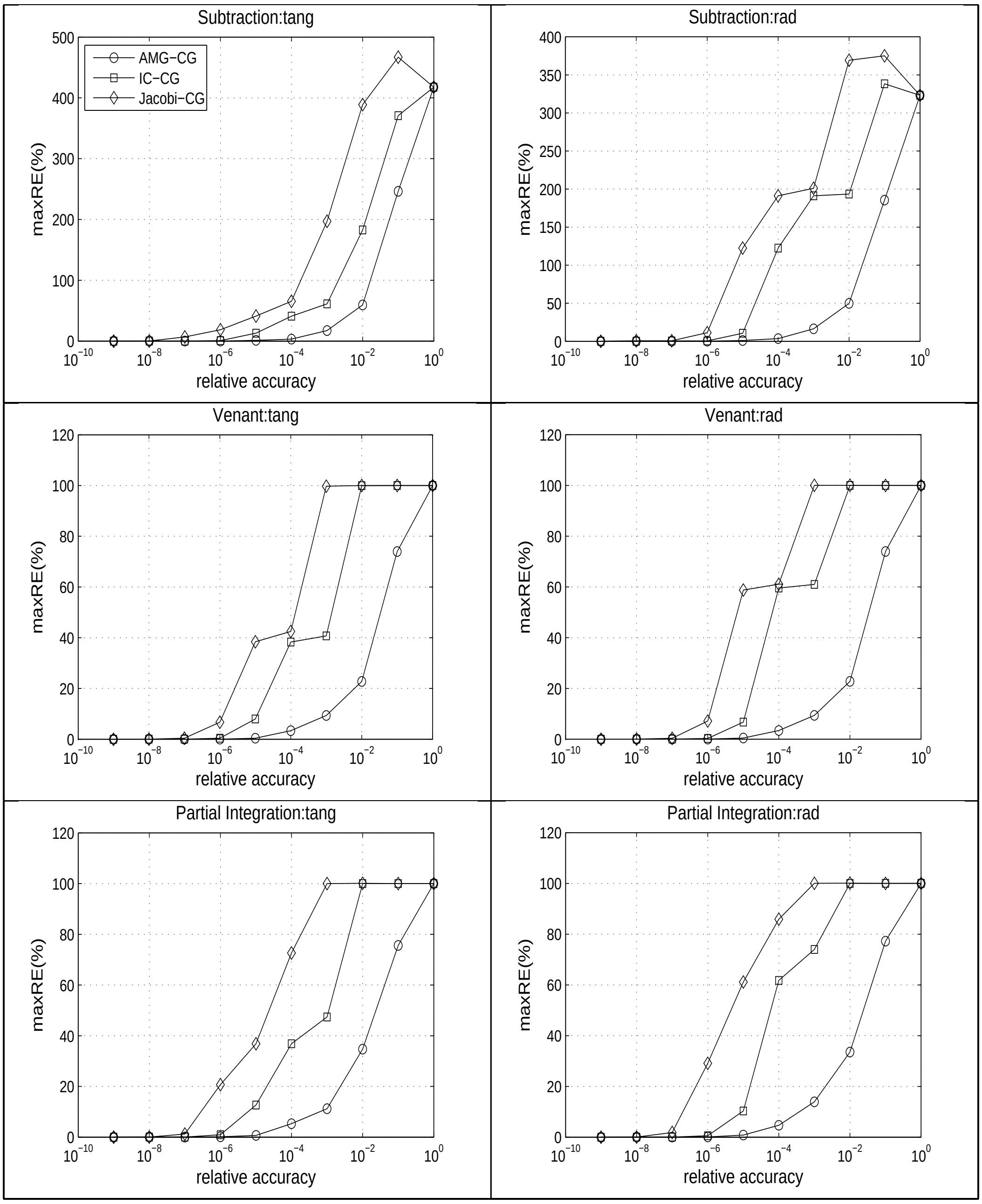

Figure 4.10. Maximal RE for solvers (AMG-CG, IC(0)-CG, and Jacobi-CG) and dipole models (subtraction, Venant, and partial integration) with quasi-tangential and quasi-radial sources in a realistic four tissue head model. The left colum is for a quasi-tangential source and the right is for a quasi-radial source. The relative accuracy on the x axis is the relative error in $KC^{-1}K$ energy norm. The x axis uses a log scale.

Figure 4.11 shows an potential map with isopotential lines and shading on a sagittal cut of the head. The forward potential was computed for the Venant quasi-tangential

Table 4.7. Average solver time (sec) and average iteration count at the largest relative accuracy that leads to maxRE error within 1% for AMG-CG, IC(0)-CG, and Jacobi-CG with subtraction, Venant, and partial integration models, given the realistic volume conductor model. The gain factor indicates the performance gain of the AMG-CG relative to the Jakobi-CG.

Quasi-tangential source									
dipole model	subtraction			Venant			partial int.		
	acc	time	iter	acc	time	iter	acc	time	iter
AMG-CG	10^{-6}	2.81	12.69	10^{-5}	2.19	9.99	10^{-5}	2.08	9.44
IC(0)-CG	10^{-6}	9.41	201.9	10^{-6}	8.97	194.8	10^{-6}	8.66	188.7
Jacobi-CG	10^{-8}	20.51	997.7	10^{-7}	18.54	893.6	10^{-8}	20.68	961.8
gain factor		7.30	78.6		8.47	89.4		9.94	101.9

Quasi-radial source									
dipole model	subtraction			Venant			partial int.		
	acc	time	iter	acc	time	iter	acc	time	iter
AMG-CG	10^{-5}	2.29	10.42	10^{-5}	2.24	10.21	10^{-5}	2.09	9.49
IC(0)-CG	10^{-6}	9.22	199.7	10^{-6}	8.91	194.6	10^{-6}	8.69	190.2
Jacobi-CG	10^{-7}	19.11	904.8	10^{-7}	18.61	893.7	10^{-8}	20.24	957.5
gain factor		8.34	86.8		8.30	87.5		9.68	104.1

source in the right somatosensory, using the AMG-CG solver with a relative accuracy of 10^{-5}.

4.4 Discussion and conclusion

The goals of this technical study of finite element (FE) based solution techniques for the elecroencephalographic forward problem were twofold. The first aim was to compare three efficient iterative FE solver techniques under realistic conditions that still allowed quasi-analytical solutions. The second aim was to evaluate three different numerical formulations of the current dipole, which is the bioelectric source most commonly used to represent neural electrical activity. A major motivation of such studies is the special need to achieve high accuracy and efficiency with FE based approaches for this problem. The many advantages of this approach are often hindered by unacceptable computational costs so that improved efficiency will provide substantial progress to the field.

When using the $K_hC_h^{-1}K_h$-energy norm stopping criterion for the PCG algorithm applied on meshes with up to 500 K nodes, relative solver accuracies of 10^{-6} for AMG-CG, 10^{-7} for IC(0)-CG and 10^{-8} for Jacobi-CG were necessary and sufficient to fall below the discretization error. The AMG-CG achieved an order of magnitude higher computational

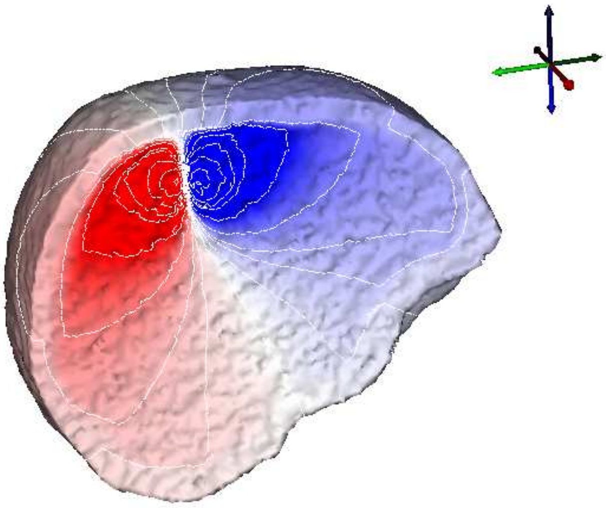

Figure 4.11. Potential map on the head surface and the sagittal cut with iso-potential lines. The source is at the right somatosensory cortex with quasi tangential orientation. The potential was computed with AMG-CG solver, Venant dipole model, and the relative accuracy of 10^{-5}.

speed than the CG with the standard preconditioners with this acceleration increasing as the mesh size decreased.

We generated two groups of Constrained Delaunay tetrahedral FE meshes, tuned for the specific needs of the different potential approaches. In Group 1 using the full subtraction approach [21], FE nodes were concentrated in the CSF, skull and skin, while the brain compartment was meshed as coarsely as possible. Group 2 was tuned for the needs of both direct potential approaches [11, 13, 15, 18], which profit more from a regular distribution of FE nodes over all four compartments and especially higher resolution at the source positions.

With regard to the numerical error, in the tuned FE meshes with about 500 K nodes, we achieved high accuracies—in the range of a few percent maximal relative error (maxRE)—over all source eccentricities for both the full subtraction and the two direct potential approaches. With a maximal relative difference measure (maxRDM) and a maximal magnification factor (maxMAG) of less than 1% over all source eccentricities for sources up to 1 mm below the CSF compartment (model `tet503K`, maximal examined eccentricity of 98.7%), the full subtraction approach performed consistently better than both direct approaches. Our results clearly illustrate the advantages of the full subtraction approach as long as the homogeneity condition is fulfilled, i.e., as long as the distance of the source to the next conductivity inhomogeneity is large enough or the resolution of the FE mesh at the nearest conductivity inhomogeneity to the source is fine enough. A theoretical reasoning for this finding is given in [20]. While error curves oscillated for both direct approaches, they were smooth for the full subtraction approach.

Schimpf et al. [19] investigated different FE potential approaches in a four-layer sphere model with isotropic skull and sources up to 1 mm below the CSF compartment. In their report, a regular 1 mm cube model was used (thus a much higher FE resolution than used in this study) and a maxRDM of 7% and a maxMAG of 25% were achieved with a subtraction approach, which performed best in their comparison. Awada et al. [13] implemented a two-dimensional subtraction approach and compared its numerical accuracy with a partial integration method in a two-dimensional multi-layer sphere model. A direct comparison with our results is therefore difficult, but the authors concluded that the subtraction method was more accurate than the direct approach. In a locally refined (around the source singularity) tetrahedral mesh with 12,500 nodes of a four-layer sphere model with anisotropic skull and first order FE basis functions in a subtraction approach, Bertrand et al. [12] reported a maxRDM of above 20% and a maxMAG up to 70% for a maximal eccentricity of 97.6%. Van den Broek [14] used a subtraction approach in a locally refined (around the source singularity) tetrahedral mesh with 3,073 nodes of a three-layer sphere model with anisotropic skull. For the maximal examined eccentricity of 94.2%, they reported a maxRDM of up to 50%.

However, the right-hand side (RHS) vector is expensive to compute and is densely populated (i.e., N_h non-zeros) for the full subtraction approach (3.14) and sparse with just some few ($|\textsc{NodesOfEle}|$ for partial integration (3.16), and C for Venant (3.18)) non-zero vector entries for the direct approaches, which has implications for the computational effort when using the fast FE transfer matrix approach for EEG and MEG [18, 25–27], which limits the total number of FE linear equation systems to be solved for any inverse method to the number of sensors, m. After solving m FE linear equation systems to compute the transfer matrix, each forward problem can be solved by a single multiplication of the RHS vector with the transfer matrix [26], resulting in a computational effort of $2 \times m \times P$ operations with $P = N_h$ for the full subtraction, $P = |\textsc{NodesOfEle}|$ for partial integration and $P = C$ for the Venant approach. Note that the transfer matrix approach cannot be used if the mesh is adapted according to varying source positions within the inverse problem. We therefore attempted to avoid local mesh refinement techniques such as those used elsewhere [12, 14].

In conclusion, the AMG-CG achieved an order of magnitude higher computational speed than Jacobi-CG or incomplete Cholesky-CG for the FEM based EEG forward and inverse problem. Our results corroborate the theoretical results that the higher the FE resolution, the greater the advantage of using MG preconditioning. The AMG-CG together with the fast transfer matrix approach enables resolutions which seemed to be impracticable before. In the comparison of dipole modeling approaches, highest accuracies were achieved with the full subtraction approach in CDT meshes, where nodes were concentrated in the compartments CSF, skull and skin.

CHAPTER 5

LOW RESOLUTION CONDUCTIVITY ESTIMATION WITH EEG SOURCE LOCALIZATION

5.1 Introduction

Bioelectric source analysis in the human brain from scalp Electroencephalography signals is sensitive to geometry and conductivity properties of the different head tissues. In this chapter we describe a Low Resolution Conductivity Estimation (LRCE) method using simulated annealing optimization on high-resolution finite element models that individually optimizes a realistically-shaped volume conductor with regard to the tissue conductivities. As input data, the method needs T1- and PD-weighted magnetic resonance images to produce a volume conductor model and scalp potential data. Our simulation studies showed that for realistic signal-to-noise somatosensory evoked potentials, the LRCE method was able to simultaneously reconstruct both the brain and the skull conductivity together with the underlying dipole source in somatosensory cortex and provided an improved source analysis result. Furthermore, using scalp potentials with a high signal-to-noise ratio, the LRCE method was even able to simultaneously reconstruct a pair of dipole sources together with the brain and the skull conductivity. The new method was then applied to measured tactile somatosensory evoked potentials. The LRCE estimated the brain conductivity to be 0.48 S/m, which is higher than the commonly used value of 0.33 S/m. The skull conductivity was fitted to the value of 0.004 S/m, which is in the range of the commonly used value. With these results, we have shown the viability of an approach that computes its own conductivity values and thus reduces the dependence on assigning values from the literature and likely produces a more robust estimate of current sources. Using the LRCE method, the individually optimized (with regard to both geometry and conductivity) volume conductor model can in a second step be used for the analysis of clinical or cognitive data acquired from the same subject.

5.2 Methods

5.2.1 Transfer matrix approach with Venant dipole

As described in the Chapter 3, we used the finite element (FE) method for the numerical approximation of equations (2.1) in combination with the reference electrode. Chapter 4 contains the results of a comparison of three different FE approaches for modeling the source singularity: a subtraction approach [53, 75], a Partial Integration direct method [56], and a Venant direct method [5]. Based on the results of this comparison, in this LRCE study we used the Venant approach, which for sufficiently regular meshes, yields suitable accuracy over all realistic source locations [74, 75]. This approach has the additional advantage of high computational efficiency when used in combination with the FE transfer matrix approach described in Section 3.4.1 [57].

With these assumptions, Eq. 3.3 then becomes

$$\mathrm{K} \cdot \underline{u} \quad = \quad \underline{J}^{Ven} \tag{5.1}$$

where K is the stiffness matrix with dimension $n \times n$, $\underline{u}$ is the potential coefficient vector with $(n \times 1)$, and $\underline{J}^{Ven}$ is the Venant approach right-hand-side source vector $(n \times 1)$ [5, 74]. A key goal of this study was to pursue solutions that achieve high computational efficiency. Let us assume that there are e electrodes that directly correspond to FE nodes on the surface of the head model (when not directly corresponding, potentials at electrodes need interpolation among those of neighboring nodes). It is then straightforward to determine the restriction matrix $\mathrm{R} \in \mathbb{R}^{(e-1)\times n}$ in Section 3.4.1, which has only one non-zero entry with the value 1 in each row and which maps the potential vector $\underline{u}$ at nodes onto the potential vector $\underline{\Phi}_{EEG}$ at the $(\mathrm{e}-1)$ non-reference EEG electrodes:

$$\mathrm{R}\,\underline{u} =: \underline{\Phi}_{EEG}. \tag{5.2}$$

With the following definition of the $((e-1) \times n)$ *transfer matrix* for the EEG, T,

$$\mathrm{T} := \mathrm{R}\,\mathrm{K}^{-1}, \tag{5.3}$$

a direct mapping of an FE right-hand side vector onto the unknown electrode potentials is given as:

$$\mathrm{T}\,\underline{J}^{Ven} \overset{(5.3)}{=} \mathrm{R}\,\mathrm{K}^{-1}\underline{J}^{Ven} \overset{(5.1)}{=} \mathrm{R}\underline{u} \overset{(5.2)}{=} \underline{\Phi}_{EEG}. \tag{5.4}$$

Note that $\underline{J}^{Ven}$ has only C non-zero entries (with C being the number of neighbors of the closest FE node to the source) so that T $\underline{J}^{Ven}$ only amounts in $2 \cdot (e-1) \cdot C$ operations. Thus the resulting combination of the transfer matrix approach with the Venant method leads to implementations that are especially efficient, an essential feature for our study.

The inverse FE stiffness matrix K^{-1} from (5.1) exists, but its computation is a difficult task, since the sparseness of K will be lost while inverting. By means of multiplying equation (5.3) with the symmetric matrix K from the right side and transposing both sides, we obtain

$$\mathrm{K}\mathrm{T}^{tr} = \mathrm{R}^{tr}. \tag{5.5}$$

The FE transfer matrix can thus be computed by means of iteratively solving (S − 1) large sparse FE linear equation systems. Note that a fast FE transfer matrix for the Magnetoencephalography (MEG) forward problem can be derived in a similar way [6, 57]. To solve numerically the resulting linear FE equations, we employed an algebraic multigrid preconditioned conjugate gradient (AMG-CG) method [58], solved to a relative error of 10^{-9} in the controllable $\mathrm{K}P^{-1}\mathrm{K}$-energy norm (with P^{-1} the matrix resulting from one V-cycle of the AMG).

5.2.2 Globally minimizing the cost function

Since the volume conduction properties are incorporated in the lead field matrix L_r, the free nonlinear optimization parameters in this case are only the source locations. Optimization methods such as the Nelder-Mead simplex approach [95], the Levenberg-Marquardt algorithm [96], and Simulated Annealing (SA) from combinatorial optimization [97] are all able to update the source locations based on the previous source location and misfit value. The optimization procedure continues until the cost function meets a predefined tolerance criterion or a maximum allowable number of iterations. The challenge of local optimizers such as the Nelder-Mead simplex and the Levenberg-Marquardt algorithm lies in determining the initial estimation of multiple parameters in the presence of multiple local minima; a global optimizer such as SA is generally more effective in localizing multiple parameters because it eliminates the need for high quality initial estimates [84, 98–100]. We used an SA method that follows the Metropolis algorithm for the stochastic optimization process [101]. The energy (the cost function in our case) for the assigned parameters in each iteration was compared with a previous energy and when the energy state was smaller than the previous $\Delta E < 0$, the parameters were always accepted. When the energy was larger than the previous $\Delta E > 0$, the acceptance of the parameters depended on the probability based on the Metropolis criterion (6) [97]. This stochastic acceptance test prevents the search from getting trapped in local minima as long as the cooling schedule is slow enough [102, 103].

The following equation describes the process:

$$\begin{aligned} P(\Delta E, \mathrm{t}) &= \exp^{-(\Delta E/\mathrm{t})} \\ \mathrm{t} &= f_{\mathrm{t}} \cdot \mathrm{t}_{previous}, \end{aligned} \tag{5.6}$$

where t is a so-called temperature factor that regulates the acceptance probability. Throughout the optimization process, t decreases according to a cooling rate f_{t}. When the cooling is slow enough, SA has been shown to converge to the global minimum of a given cost function in a large search space [102, 103]. Initially the temperature is set to a high value, resulting in the acceptance of most new parameters and as the temperature decreases, it is less likely for new parameters to be accepted. This enables the search to focus on the vicinity of the minima at the later stages of the optimization process.

5.2.3 Low resolution conductivity estimation

The proposed LRCE method adds electrical tissue conductivities as additional optimization parameters to the cost function to the already parameterized source locations. Here the set of optimization parameters including the conductivities was

$$X = \{s, \sigma\} = \{\vec{s}_1, \vec{s}_2, \cdots, \vec{s}_{\mathrm{k}}, \sigma_1, \sigma_2, \cdots, \sigma_{\mathrm{L}}\}, \tag{5.7}$$

where L is the number of tissue compartments and σ_{l} is the conductivity parameter for the l-th tissue compartment ($1 \leq \mathrm{l} \leq \mathrm{L}$). Each source location $\vec{s}_{\mathrm{i}}$ ($1 \leq i \leq k$) was allowed to vary within the defined discrete influence space as described in Section 3.4. The conductivity σ_{l} of tissue compartment l was allowed to have its value from a predefined discrete set of possible conductivity values

$$\sigma_{\mathrm{l}} \in \{\sigma_{h_{\mathrm{l}}}, 1 \leq h_{\mathrm{l}} \leq H_{\mathrm{l}}\}. \tag{5.8}$$

Here, H_{l} is the number of possible conductivity values for tissue compartment l. Theoretically one could choose H_{l} to be a large number (high resolution) for each tissue, but this would strongly increase computational costs and might be rather unrealistic given the limited SNR in measured EEG data. Therefore, we confined each tissue to a rather small set of conductivity values (e.g., the different measured values for the considered head tissue that can be found in the literature).

Given the influence source space and the electrode locations, we precomputed a set of lead field matrices and collected them in Λ, which corresponded to all possible combinations of conductivity values for all tissue compartments of interest. This resulted in the number $\prod_{\mathrm{l}=1}^{\mathrm{L}} H_{\mathrm{l}}$ of lead field matrices in Λ.

$$\Lambda = \{L\left(\sigma_{h_1}, \ldots, \sigma_{h_{\mathrm{L}}}\right) : 1 \leq h_{\mathrm{l}} \leq H_{\mathrm{l}}, 1 \leq \mathrm{l} \leq \mathrm{L}\}, \tag{5.9}$$

with $L\left(\sigma_{h_1}, \cdots, \sigma_{h_{\mathrm{L}}}\right)$ being the $(\mathrm{e} \times 3\mathrm{r})$ lead field matrix for the specific choice of conductivities. Here, we describe an extension to the EEG transfer matrix approach, described in Section 5.2.1, aimed at enhancing the computation of Λ. During each iteration of the SA method, the set of optimization parameters includes not just a new estimate of the bioelectric source, but a new configuration of both sources and conductivities in which we allow changing the value of only one parameter chosen randomly per iteration. By limiting the choice of conductivities to a discrete set of values, we maintain computational efficiency by applying the associated precomputed lead field matrix from the set Λ. The total number of possible configurations for sources and conductivities is

$$\begin{pmatrix} \mathrm{r} \\ \mathrm{k} \end{pmatrix} \cdot \prod_{\mathrm{l}=1}^{\mathrm{L}} H_{\mathrm{l}}. \tag{5.10}$$

The SA optimizer searches for an optimal configuration of dipole source locations r and tissue conductivities σ that ensure the best fit to the measured data:

$$g_f = \underset{s,\sigma}{min} \, \|\underline{\Phi}_{EEG} - \underline{\Phi}_{sim}(s,\sigma)\|_2 = \underset{s,\sigma}{min} \, \|\underline{\Phi}_{EEG} - L_s(\sigma) \cdot \underline{J}_s\|_2 \tag{5.11}$$

The following summarizes the general procedure of the low resolution conductivity estimation.

- Define the discrete influence space with r nodes.
- Fix the number k of sources to be fitted.
- For all L tissue compartments, define a discrete set of conductivity values, i.e., fix all $\sigma_{h_{\mathrm{l}}}, 1 \leq h_{\mathrm{l}} \leq H_{\mathrm{l}}, 1 \leq \mathrm{l} \leq \mathrm{L}$
- Precompute the set of lead field matrices Λ corresponding to each of the possible conductivity combinations.

- **Repeat:**
  - Allow SA optimizer to choose a configuration of source locations $s = (\vec{s}_1, \vec{s}_2, \cdots, \vec{s}_\mathrm{k})$ and conductivities $\sigma = (\sigma_1, \cdots, \sigma_\mathrm{L})$
  - Get lead field matrix $L_s(\sigma)$ for the chosen source and conductivity configuration.
  - Compute its cost function value, $g_f = min\|\underline{\Phi}_{EEG} - L_s(\sigma)\underline{J}_s\|_2$ with respect to source moments $\underline{J}_s$.
- **Until** cost function value meets a tolerance criterion or the number of iterations exceeds a limit.

5.2.4 Realistic head model

To carry out the LRCE analysis requires the construction of detailed realistic head models, in this case from MRI image data. Here we used the same realistic head model of Wolters *et al* [3] and summarized the steps for constructing the head model. The approach emphasizes accurate modeling of the skull thickness, as the influence of this parameter is closely related to the influence of skull conductivity and therefore is important for a successful application of the presented LRCE algorithm.

In order to create an accurate geometric model of human head, we used multiple MR imaging modalities, both T1-weighted MRI and PD-weighted MRI. T1-MRI is a good modality to segment tissue boundaries such as scalp, outer skull, and gray matter. On the other hand, PD-MRI is a good modality to segment the inner skull boundary, since the amount of water proton in the CSF is much higher than that of the skull bone and this large difference resulted in a high contrast between the two substances. Combining two imaging data made it possible to construct more accurate skull thickness than the imaging data of a single modality. We collected the imaging data from a healthy 32 years old male subject by a 3 Tesla whole body MRI scanner (Medspec 30/100, Bruker, Ettlingen/Germany). An inversion recovery MDEFT sequence [104] and 3D FLASH protocol [105] were carried out for T1- and PD-MRI, respectively. For the detailed parameters used in the processing, refer to Wolters *et al* [3]. The final imaging resolution is 1 x 1 x 1.5 mm^3 in both T1- and PD-MRI.

A registration between the T1- and the PD-MR imaging data was performed to align the images and to correct the changes of subject's position. This registration used a voxel-similarity based affine registration without pre-segmentation, using a cost-function based on mutual information described in Wolters *et al* [3]. Based on the registered images, image segmentation was carried out by an Adaptive Fuzzy C-Means classification method [3, 35] and a deformable model algorithm [3]. Since a portion of the head that the EEG electrodes do not cover has a weak influence on source localization, the segmentation procedures did not attempt to model the portion, but removed it from the model based on a cutting protocol in Fuchs *et al* [5] and Buchner *et al* [51]. As a result, a four compartment (scalp, skull, CSF, and brain) head model was created for the use of LRCE study. Figure 5.1 shows the inner skull boundary extracted from the bimodal MRI, compared with a boundary from a method that used only the T1-MRI. Figure 5.2 shows a region of image voxels in which PD-MRI based segmentation improved the skull thickness.

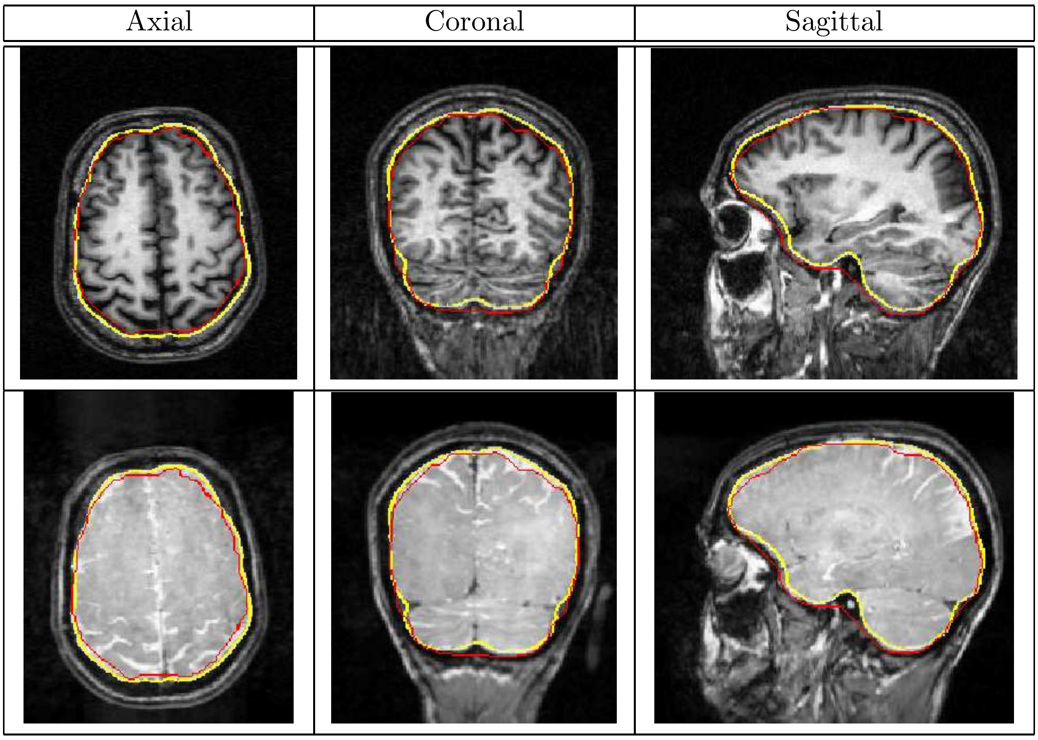

Figure 5.1. Segmentation of the inner skull surface: Comparison of the results using the bimodal T1- and PD-MRI data set (in yellow) with the inner skull estimation approach using exclusively the T1-MRI (in red) on underlying T1-MRI (top row) and PD-MRI (bottom row). The images are adapted from [3]

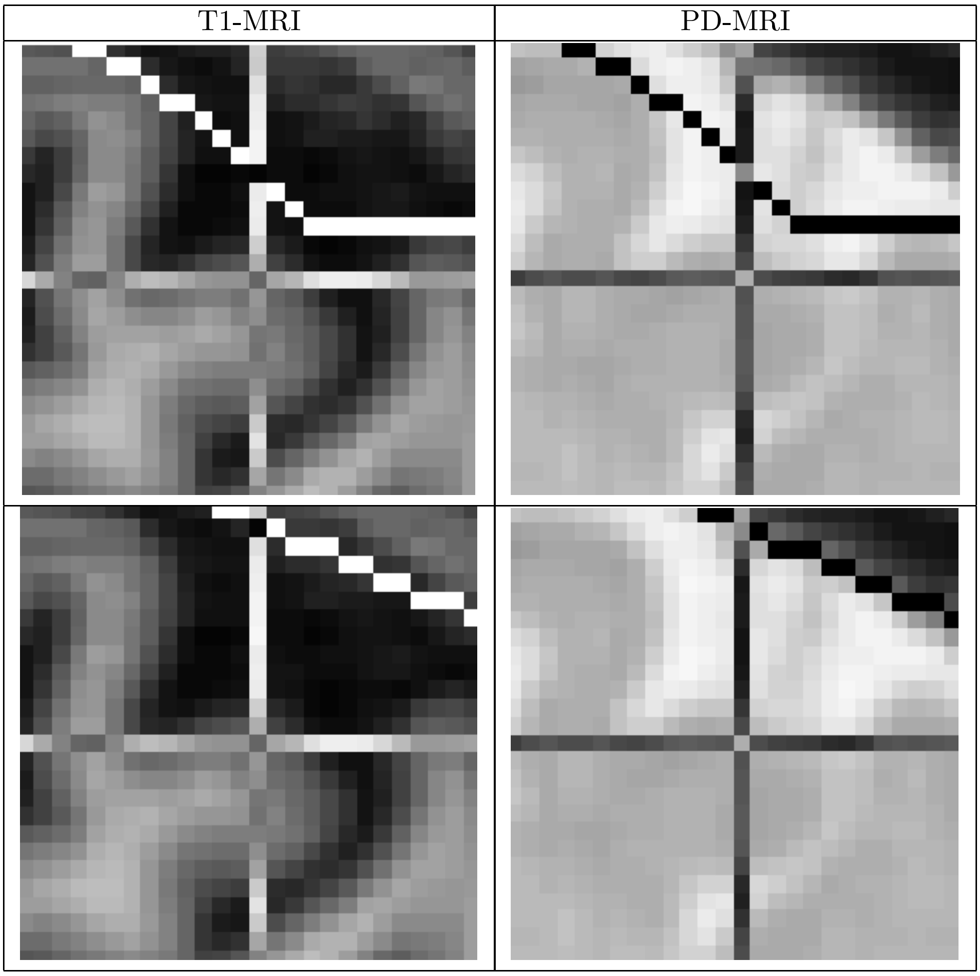

Figure 5.2. Segmentation of the inner skull surface: Images represents the parietal area of the neurocranial roof. Diagonal line on each image indicates the boundary between CSF and skull. While the images on the top row are overlapped with the skull-CSF boundary line segmented only by T1-MRI, the images on the bottom row are overlapped with that of PD-MRI. The CSF layer extracted by PD-MRI is thicker than being segmented by means of the T1-MRI based estimation procedure. The images are adapted from [3]

5.2.5 Volume conductor FE mesh generation

Given the segmented information from the above procedures, we generated finite element mesh that represents the geometric and electric properties of the head volume conductor. We used the commercially available CURRY software [94] to create a tetrahedral tessellation of the four compartment head model. CURRY generates meshes based on the the Delaunay-criterion that results in the regular tetrahedra elements [3, 5]. The finite element volume conductor model had n = 245,257 nodes and 1,503,357 tetrahedra elements, shown in Figure 5.3. The color in Figure 5.3 indicates different electric tissue conductivities.

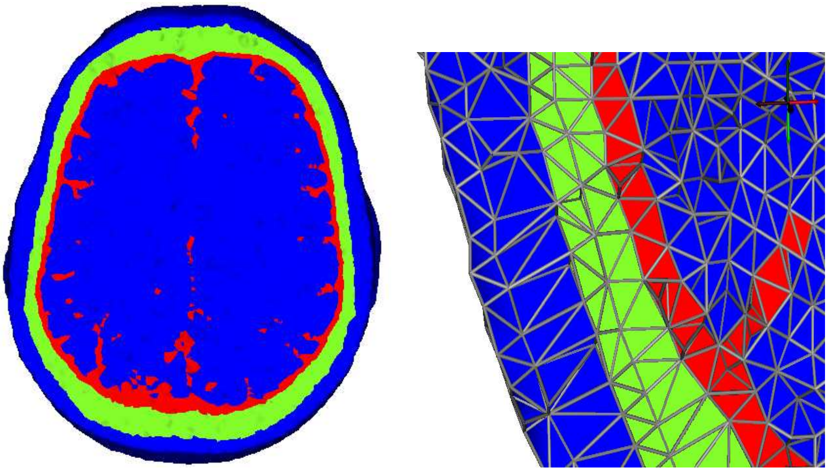

Figure 5.3. Top row: Four compartment (scalp, skull, CSF and brain) realistic finite element head model. Cross-section through the FE model without (left) and with (right) visualization of the element edges.

5.2.6 Influence space mesh generation

An influence source space that represented the brain gray matter in which dipolar source activities occur was extracted from a surface 2 mm beneath the outer cortical boundary. The influence space was tessellated with a 2 mm mesh resulting in r = 21,383 influence nodes and 42,916 triangular elements shown in Figure 5.4. Since any influence mesh is only a rough approximation of the real folded surface and does not appropriately model the cortical convolutions and deep sulci, no normal-constraint was used, i.e., the dipole sources were not restricted to be oriented perpendicular to the source space. Instead, dipole sources in the three Cartesian directions were allowed.

5.2.7 Setup of the LRCE simulation studies

To validate the new LRCE approach, we carried out simulation studied with a reference volume conductor using isotropic conductivity values of 0.33 (see [106] and references therein), 0.0132 [44], 1.79 [37], and 0.33 S/m (see [106] and references therein) were assigned to the scalp, skull, CSF, and brain compartment, respectively. The results was a brain:skull ratio of 25 for the reference volume conductor. For the modeling of the

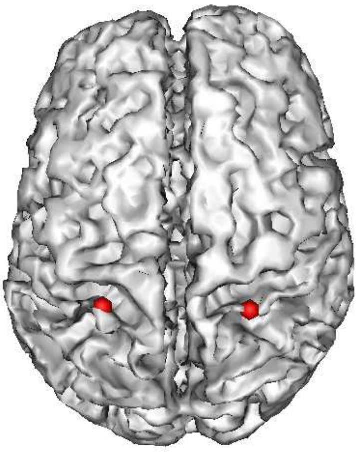

Figure 5.4. The cortical influence source space is extracted from 2mm under the brain outer surface. The region of somatosensory dipole sources are indicated by red dots.

EEG, 71 electrodes were placed on the reference volume conductor surface according to the international 10/10 EEG system.

Two reference dipole sources were positioned on influence nodes in area 3b of the primary somatosensory cortex (SI) in both hemispheres, as shown in Figure 5.4. Two source orientation scenarios were considered, in which both dipoles were either oriented quasi-tangentially or quasi-radially with regard to the inner skull surface. In both scenarios, the two sources were simultaneously active using current densities of 100 nAm. Another experiment consisted of just a single source in the left SI with quasi-tangential or quasi-radial direction and a source strength of 100 nAm. Forward potential computations were carried out for the different scenarios using the direct FE approach as described in Section 5.2.1. Noncorrelated Gaussian noise was then added such that the signal-to-noise-ratio,SNR were 40, 25, 20, and 15 dB ($SNR(dB) := 20*\log_{10}(SNR)$ with $SNR := \frac{1}{\mathrm{S}}\sum_{i=1}^{\mathrm{S}}\left|\frac{\underline{\Phi}_{EEG}^{[i]}}{\underline{\epsilon}^{[i]}}\right|$, where $\underline{\Phi}_{EEG}^{[i]}$ is the noisy signal and $\underline{\epsilon}^{[i]}$ the noise at electrode i). Figure 5.5 shows the potential maps for the two-sources experiment for both orientation scenarios, the quasi-tangential (top row) and the quasi-radial orientations (bottom row) for different SNR values.

5.2.8 SEP measurement

We then measured somatosensory evoked potentials (SEP) in order to estimate subject-specific conductivity values by applying our LRCE approach to real empirical EEG data.

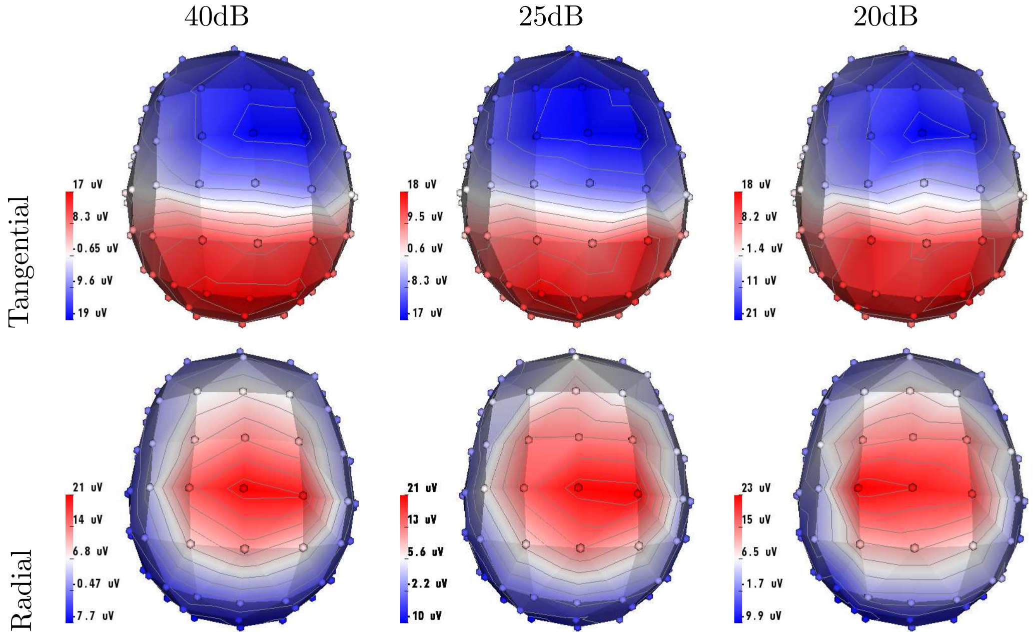

Figure 5.5. Simulated noisy (40, 25, and 20dB from left to right) reference data for the two-sources and two-orientation scenarios in the reference volume conductor model (σ_{brain}:σ_{skull} = 25). The top row shows the maps of the simultaneously active quasi-tangentially oriented somatosensory sources and the bottom row the maps of the simultaneously active quasi-radially oriented sources. The potential maps are linearly interpolated over the electrodes (white spheres). Gray lines indicate isopotentials and the map scale is in microvolt.

A tactile stimulus that evokes the SEP results in an activation of single dipole in a somatosensory cortex. When we use the SEP data as an input to the LRCE method, we can predict the number of active source to inversely fit. This application of the LRCE to the SEP data is intended to localize the single somatosensory evoked dipole and to estimate the subject-specific tissue conductivity.

Tactile somatosensory stimuli were presented to the right index finger of the right-handed subject from Section 5.2.4 using a balloon diaphragm driven by bursts of compressed air. We compensated for the delay between the electrical trigger and the arrival of the pressure pulse at the balloon diaphragm as well as the delay caused by the inertia of the pneumatic stimulation device (half-way displacement of the membrane), together 52 ms in our measurements. Following standard practice [83], the stimuli were presented at 1 Hz (±10% variation to avoid habituation effects). A 63 EEG channel system following the standard 10% EEG system recorded the raw time signals for the SEP study. Two

EOG (Electro-oculo-graphy) electrodes were furthermore used for horizontal and vertical eye movement control. The collection protocol consisted of three runs of 10 minutes each EEG data with a sampling rate of 1200 samples/sec using a real time low pass filter of 0-300 Hz. The BESA software [107] was then used for a rejection of noise-contaminated epochs (e.g., epochs containing eye movements detected by means of the EOG channels) and for averaging the non-contaminated epochs within each run. In order to optimize the SNR, the SEP data were furthermore averaged over the three averaged runs. The baseline-corrected (from -35 ms to 0 ms pre-stimulus) averaged EEG dataset was filtered using a 4th order butterfly digital filter with a bandwidth of 0.1 to 45 Hz. When using the prestimulus interval between -20 ms and 0 ms for the determination of the noise level and the peak of the first tactile component at 35.3 ms as the signal, we achieved a SNR of 24 dB. Finally, by means of a channel-selection procedure (exclusion of 20 ipsilateral electrodes with poor SNR), we were able to even increase the SNR to 26.4 dB. A butterfly- and a position-plot of the SEP data is shown in Fig. 5.6.

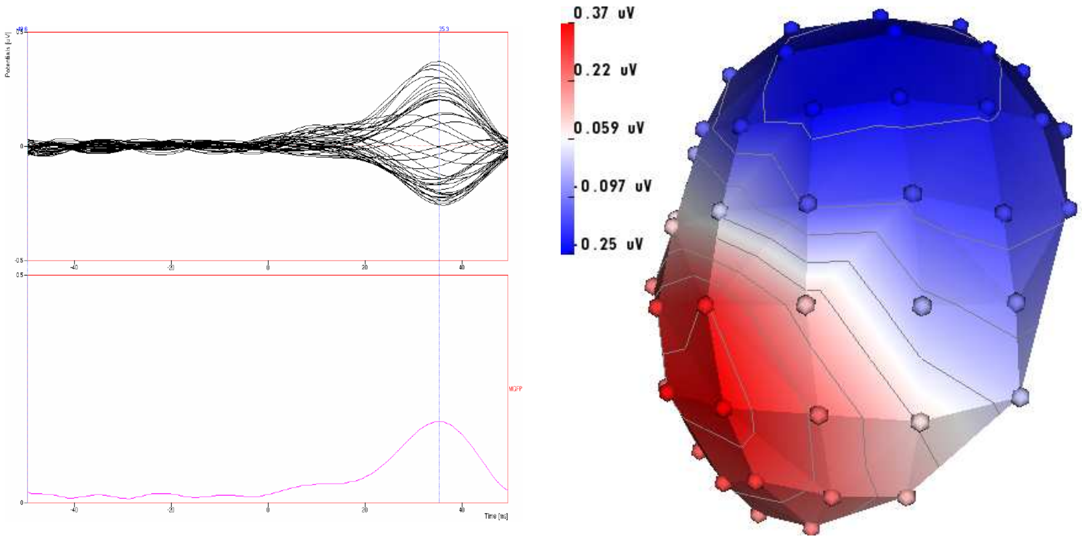

Figure 5.6. First tactile SEP component at the 43 selected electrodes. Selection was performed in order to optimize the SNR. (Left) Butterfly plot (Right) Interpolated potential map of P35 component on the selected electrodes. Gray lines indicate isopotentials.

5.2.9 Measures of Estimation Quality

There are two measures used in this study, localization error and explained residual variance. The localization error is defined as the Euclidian distance between the reference source locations used in computing simulated EEG and the fitted source locations resulted from conductivity estimation. The residual variance, v, of the goal function was calculated as the percentile misfit between the noisy reference potential and the fitted potential that was computed from the fitted source parameters and conductivities. The explained variance is then defined as $100\% - v$.

5.3 Results

We performed simulation studies with various scenarios including brain and skull conductivity estimation with two-source localization, brain and skull conductivity estimation with single source localization, and skull only conductivity estimation with two-source localization. We then applied our LRCE method to the real SEP data set of a subject in order to estimate the actual tissue conductivity of the subject.

5.3.1 Simultaneous reconstruction of brain and skull conductivity and a pair of somatosensory sources

For this studies, we performed the LRCE procedure as described in Section 5.2.7 with an inverse two-dipole fit on the discrete influence space, while allowing skull and brain conductivity to vary as free discrete optimization parameters. The permitted brain conductivities (σ_{brain}) were 0.12, 0.33 [106], and 0.48 S/m with scalp and brain conductivities set to be equal. For each brain conductivity, the skull conductivity (σ_{skull}) was allowed to vary so as to achieve brain:skull ratios of 80, 40, 25, 15, 10, 8, and 5. The CSF conductivity remained fixed at 1.79 S/m. Keeping the CSF conductivity fixed avoided possible problems that are due to the ambiguity between source strength and overall conductivity. This resulted in a total of 21 conductivity configurations.

$$\begin{aligned}
X &= \{s_{left_{somato}},\ s_{right_{somato}},\ \sigma_{skull},\ \sigma_{brain}\} \\
\sigma_{brain} &\in \{0.12,\ 0.33,\ 0.48\ S/m\} \\
\sigma_{skull} &\in \{\sigma_{brain}/r,\ where\ r = 80, 40, 25, 15, 10, 8, 5\} \\
\sigma_{scalp}/\sigma_{brain} &= \ 1,\ \ \sigma_{CSF} =\ 1.79\ S/m
\end{aligned}$$

Following Equation (5.10), the total number of possible source and conductivity configurations in this simulation was thus approximately 4.8 billion. For the SA optimization, we used a very slow cooling schedule with the cooling rate (f_{t}) of 0.99 in order to make sure that the search reached the global minimum of the cost function. The current acceptance probability was determined by setting the current temperature, t_i, at 99% of the previous

Table 5.1. Results of the LRCE algorithm when applied to the simultaneous reconstruction of the brain and the skull conductivity together with a pair of active sources in the somatosensory cortex. Part I: Localization error and estimated conductivity.

Reference SEP	Localization error(mm)		Estimated conductivity		Goal function
(tangential)	right dipole	left dipole	$\sigma_{brain}(S/m)$	$\sigma_{brain} : \sigma_{skull}$	expl. var.(%)
Noise free	0	0	0.33	25	100
40dB	2.246	2.246	0.33	25	99.76
25dB	3.175	10.721	0.12	10	99.06
20dB	13.436	10.388	0.48	15	97.44
Reference SEP	Localization error(mm)		Estimated conductivity		Goal function
(radial)	right dipole	left dipole	$\sigma_{brain}(S/m)$	$\sigma_{brain}/\sigma_{skull}$	expl. var.(%)
Noise free	0	0	0.33	25	100
40dB	3.013	3.013	0.33	25	99.44
25dB	6.430	7.379	0.48	25	96.57
20dB	5.218	12.462	0.48	25	92.76

Table 5.2. Results of the LRCE algorithm when applied to the simultaneous reconstruction of the brain and the skull conductivity together with a pair of active sources in the somatosensory cortex. Part II: Error in dipole moments. The reference moments are (0 100 0) for the tangential and (0 0 -100) for the radial dipole.

Reference SEP	tangential	
	right dipole	left dipole
noise free	(0 100 0)	(0 100 0)
40dB	(5.1 114.4 10.5)	(-4.1 81.9 -0.9)
25dB	(-7.1 44.3 -10.4)	(-9.0 87.5 49.8)
20dB	(-2.0 192.9 59.8)	(1.8 64.6 13.8)
Reference SEP	radial	
	right dipole	left dipole
noise free	(0 0 -100)	(0 0 -100)
40dB	(-3.7 1.4 -116.9)	(6.1 -5.4 -87.7)
25dB	(11.0 -10.9 -88.7)	(33.3 -6.6 -120.3)
20dB	(16.3 -9.9 -117.5)	(-24.5 -30.0 -149.1)

temperature, i.e., $t_{i+1} = 0.99 * t_i$. The maximum number of SA iterations was set to 50 million.

Table 5.1 contains the LRCE source localization and conductivity estimation results for the simulated reference SEP data. As the table shows, besides appropriately localizing both sources, the LRCE was able to accurately select the reference conductivity values of the brain and the skull compartment in the cases of noise free and low-noise (40 dB SNR) SEP data. However, for the noisy data with a SNR of 25 or lower, neither the somatosensory sources nor the brain and the skull conductivity values could be selected correctly. Table 5.2 additionally presents the LRCE reconstruction errors in the corresponding dipole moments.

5.3.2 Simultaneous reconstruction of brain and skull conductivity and a single source in the left somatosensory cortex

In the second set of simulations, we first generated noise-free and noisy reference data for a single dipole source in the left somatosensory cortex and then performed a single dipole fit with skull and brain conductivity as two additional free optimization parameters in the LRCE. We used the same scalp, skull, CSF, and brain conductivity values as in the previous simulation:

$$\begin{aligned} X &= \{s_{left_{somato}},\ \sigma_{skull},\ \sigma_{brain}\} \\ \sigma_{brain} &\in \{0.12,\ 0.33,\ 0.48\ S/m\} \\ \sigma_{skull} &\in \{\sigma_{brain}/r,\ where\ r = 80, 40, 25, 15, 10, 8, 5\} \\ \sigma_{scalp}/\sigma_{brain} &= \ 1,\ \ \sigma_{CSF} = \ 1.79\ S/m \end{aligned}$$

The number of possible source and conductivity configurations was 449K, which was also used as the maximum number of SA iterations and the cooling rate (f_{t}) was set to 0.99.

As shown in Table 5.3, the conductivity was accurately estimated for reference data with 40dB and 25dB SNR and the localization errors were acceptable. For 20dB, the localization was still acceptable, but the brain conductivity was no longer correctly reconstructed, while the skull to brain conductivity ratio was still correct. Still higher noise levels led to unacceptable results. Table 5.4 additionally presents the LRCE reconstruction errors in the corresponding dipole moments.

5.3.3 Simultaneous reconstruction of the brain:skull conductivity ratio and a pair of somatosensory sources

Using the reference volume conductor model and the reference SEP data from Section 5.2.7, we carried out a third set simulations, in which only skull conductivity was allowed to vary with fixed conductivity values for brain (0.33 S/m), scalp (0.33 S/m), and CSF (1.79 S/m). The brain:skull conductivity ratio was chosen as follows:

Table 5.3. Results of the LRCE algorithm when applied to the simultaneous reconstruction of the brain and the skull conductivity together with a single source in the left somatosensory cortex. Part I: Localization error and estimated conductivity.

Reference SEP	Localization error	Estimated conductivity		Goal function
(tangential)	(mm)	$\sigma_{brain}(S/m)$	$\sigma_{brain} : \sigma_{skull}$	expl. var.(%)
Noise free	0	0.33	25	100
40dB	0	0.33	25	99.85
25dB	2.245	0.33	25	96.73
20dB	4.141	0.48	25	95.76
15dB	9.420	0.12	25	83.39

Reference SEP	Localization error	Estimated conductivity		Goal function
(radial)	(mm)	$\sigma_{brain}(S/m)$	$\sigma_{brain}/\sigma_{skull}$	expl. var.(%)
Noise free	0	0.33	25	100
40dB	0	0.33	25	99.94
25dB	2.246	0.33	25	98.40
20dB	4.140	0.12	25	90.04
15dB	10.769	0.48	10	78.95

Table 5.4. Results of the LRCE algorithm when applied to the simultaneous reconstruction of the brain and the skull conductivity together with a single source in the left somatosensory cortex. Part II: Error in dipole moments. The reference moments were (0 100 0) for the tangential and (0 0 -100) for the radial dipole.

Reference SEP	tangential	radial
noise free	(0 100 0)	(0 0 -100)
40dB	(1.6 100.0 1.8)	(0.2 -0.1 -100.0)
25dB	(-0.7 101.9 -4.5)	(1.6 -7.0 -98.7)
20dB	(-16.2 105.6 6.0)	(-0.6 1.9 -88.0)
15dB	(-3.8 59.7 -4.8)	(-33.5 -32.8 -98.4)

$$\begin{aligned} X &= \{s_{left_{somato}},\ s_{right_{somato}},\ \sigma_{skull}\} \\ \sigma_{brain} &= \sigma_{scalp} = 0.33\ S/m,\ \sigma_{CSF} = 1.79\ S/m \\ \sigma_{skull} &\in \{\sigma_{brain}/r,\ where\ r = 80, 40, 25, 15, 10, 8, 5\} \end{aligned}$$

Table 5.5. Results of the LRCE algorithm when applied to the simultaneous reconstruction of the brain:skull conductivity ratio and a pair of active sources in the somatosensory cortex. Part I: Localization error and estimated conductivity.

Reference SEP	Localization error(mm)		Estimated	Goal function
(tangential)	right dipole	left dipole	$\sigma_{brain}/\sigma_{skull}$	expl. var.(%)
Noise free	0	0	25	100
40dB	2.236	2.246	25	99.76
25dB	2.008	3.329	25	99.04
20dB	6.025	5.941	25	97.43
15dB	17.596	41.099	15	64.31
Reference SEP	Localization error(mm)		Estimated	Goal function
(radial)	right dipole	left dipole	$\sigma_{brain}/\sigma_{skull}$	expl. var.(%)
Noise free	0	0	25	100
40dB	3.013	3.013	25	99.44
25dB	7.379	7.511	25	96.55
20dB	5.218	10.676	25	92.72
15dB	24.639	13.209	5	89.14

Table 5.6. Results of the LRCE algorithm when applied to the simultaneous reconstruction of the brain:skull conductivity ratio and a pair of active sources in the somatosensory cortex. Part II: Error in dipole moments. The reference moments were (0 100 0) for the tangential and (0 0 -100) for the radial dipole.

Reference SEP	tangential	
	right dipole	left dipole
noise free	(0 100 0)	(0 100 0)
40dB	(5.1 114.4 10.5)	(-4.1 81.9 -0.9)
25dB	(5.4 107.9 0.7)	(2.1 91.5 9.7)
20dB	(10.3 124.0 20.2)	(-16.3 98.6 3.1)
15dB	(18.8 119.4 -4.6)	(33.6 78.6 -9.5)
Reference SEP	radial	
	right dipole	left dipole
noise free	(0 0 -100)	(0 0 -100)
40dB	(-3.7 1.4 -116.9)	(6.1 -5.4 -87.7)
25dB	(15.6 -6.6 -83.3)	(29.3 2.8 -102.8)
20dB	(14.1 -2.1 -105.1)	(-27.9 -21.7 -135.5)
15dB	(-0.6 -17.9 -139.7)	(-0.5 -3.2 -31.8)

The total number of possible source and conductivity configurations for this scenario was 1.6 billion and again we used a cooling rate of $(f_{\mathrm{t}}) = 0.99$ and a maximum number of SA iterations of 10 million.

Table 5.7. Localization error(mm) for a fixed brain:skull conductivity ratio using the simulated reference SEP data with a SNR ratio of 25dB. Explained residual variance in %.

σ_{brain} to σ_{skull}	Tangential source			Radial source		
	right	left	expl. var.	right	left	expl. var.
80	12.702	10.816	98.562	13.131	15.230	95.924
40	3.757	11.228	98.960	7.514	8.281	96.445
25	2.008	3.329	99.042	7.379	7.511	96.548
15	3.175	10.725	99.038	6.736	10.041	96.452
10	2.246	10.722	98.993	7.101	10.862	96.297
8	7.101	10.722	98.692	10.093	10.769	96.093
5	3.330	20.531	98.892	9.992	18.131	96.281

As shown in Table 5.5, for both source orientation scenarios, the LRCE estimated the skull conductivity correctly down to a 20 dB SNR, while acceptable source localization errors were only achieved down to 25 dB SNR. The LRCE reconstruction failed to give acceptable results for both the source positions and the brain:skull conductivity ratio only at 15 dB SNR or above. Table 5.6 additionally presents the LRCE reconstruction errors in the corresponding dipole moments.

5.3.4 Simulation with a fixed conductivity and a pair of somatosensory sources

In a last set simulations, volume conductors with fixed skull conductivity values from the set of σ_{skull} were used. For these fixed volume conductors, only the two somatosensory sources were reconstructed on the discrete influence space using the simulated annealing optimizer with reference EEG data at a SNR of 25dB. The results in Table 5.7 show the effects of an erroneous choice of the brain:skull conductivity ratio (80, 40, 15, 10, 8, 5) on the localization accuracy in comparison to the localization errors caused just by the addition of noise when using the correct brain:skull ratio of 1:25. Incorrect skull conductivity within the source localization caused large localization errors. As expected, the correct skull conductivity ($\sigma_{brain}/\sigma_{skull} = 25$) gave the smallest localization errors and the highest explained variance for both source orientation scenarios.

5.3.5 Application of LRCE to the SEP data

To apply this approach to measured data, we carried out an analysis based on LRCE of the post stimulus P35 component of the averaged SEP data at the peak latency of 35.3ms as indicated in Figures 5.6. The detailed, four-compartment (scalp, skull, CSF, and brain) finite element model with improved segmentation of the skull geometry described in Section 5.2.4 was used as the volume conductor. Because of the limiting SNR of 26.4 dB for the SEP data and based on our simulation results from Section 5.3.2, we focused on the simultaneous reconstruction of the contralateral somatosensory P35 source in combination with the estimation of both the brain and the skull conductivities. Accordingly, we assigned fixed isotropic conductivities to scalp (0.33 S/m) and CSF (1.79 S/m). Again, the source space from Section 5.2.6 was used as the influence space for simulated annealing optimization together with brain:skull conductivity ratios of 140, 120, 100, 80, 72, 60, 42, 25, 23, 15, 10, 8 and 5.

$$\begin{aligned}
X &= \{s_{somato},\ \sigma_{brain},\ \sigma_{skull}\} \\
\sigma_{scalp} &= \ 0.33\ S/m,\ \sigma_{CSF} = \ 1.79\ S/m \\
\sigma_{brain} &\in \{0.12,\ 0.33,\ 0.48,\ 0.57\ S/m\} \\
\sigma_{skull} &= \{\sigma_{brain}/r,\ where\ r = 140, 120, 100, 80, 72, 60, 42, 25, 23, 15, 10, 8, 5\}
\end{aligned}$$

The total number of possible source and conductivity configurations, as well as the maximum of SA iterations was 1,026K and we again chose an SA cooling rate of $(f_{\mathrm{t}}) = 0.99$. Applying the LRCE approach resulted in the contralateral somatosensory source shown

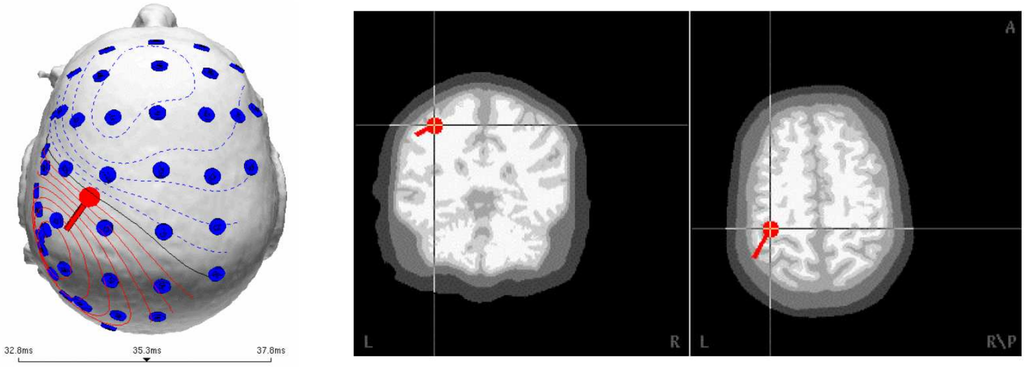

Figure 5.7. Source reconstruction result for the first tactile SEP component at the peak latency of 35.3ms.

in Fig. 5.7, with a brain conductivity of 0.48S/m, and a brain:skull conductivity ratio of 120, i.e., a skull conductivity of 0.004 S/m, with an explained variance of 98.98%. While the value of skull conductivity is close to what is generally used in source analysis (0.0042 S/m, see [5, 47, 51]), the estimated brain conductivity and thus also the brain:skull ratio is higher than the traditional values proposed [40, 106].

5.4 Discussion and conclusion

We developed a Low Resolution Conductivity Estimation (LRCE) procedure to individually optimize a volume conductor model of a human head with regard to both geometry and tissue conductivities. We exploited a combined T1-/PD-MRI dataset for the construction of a four-tissue volume conductor FE model with a special focus on an improved modeling of the skull shape and thickness and of the highly conducting cerebrospinal fluid (CSF) compartment [37]. Obtaining accurate skull geometry is important because changes in skull conductivity are known to be closely related to changes in its compartmental thickness. Goncalves *et al* also argued that the correct geometric modeling of the skull compartment was essential for the measurement of skull conductivity [45]. While other authors have used parameter estimation in continuous parameter space with local optimization algorithms [51, 73, 108], we propose the combination of a discrete low resolution parameter estimation with a global optimization method applied to realistic geometry to better take into account the limited SNR of real EEG measurements. Because the cost function was shallow [41], the proposed computationally expensive procedure using realistic FE volume conductor modeling and global Simulated Annealing (SA) optimization was important to accurately search an optimal parameter. While other authors used three compartment Boundary Element (BE) models [45, 51, 109] of the head, we additionally modeled the CSF, not only because its presence is required for accurate and realistic forward computations as shown in [3, 7], but also to avoid the problem of the ambiguity between source strength and overall conductivity.

Plis *et al* [109] derived a lower Cramer-Rao bound for the simultaneous estimation of source and skull conductivity parameters in a sphere model for dipoles whose locations were not constrained within the inner sphere volume. Since source depth and skull conductivity are closely related, their final result was that it is impossible to simultaneously reconstruct both source and skull conductivity parameters from measured surface EEG data in the sphere model. While Plis *et al* reported an incapability of the simultaneous estimation, there were strong differences to our study. Our study, as well as the FE study of Vallaghe *et al* [108], used a cortex constraint, i.e., sources were only allowed on a surface and a realistic FE model of the head instead of the spherical volume conductor model for the derivation of the Cramer-Rao bounds used by Plis *et al*, and we fixed the conductivity of the CSF compartment in our analysis to the value measured by Baumann *et al* [37].

In a first study, we evaluated the LRCE algorithm in EEG simulations for its ability to determine both the brain and the skull tissue conductivities together with the reconstruction of one and two somatosensory reference sources. At relatively low noise levels (down to 25 dB SNR in the single source scenario and down to 40 dB SNR in the two source scenario), the LRCE resulted in acceptable reconstruction errors for the reference sources and correctly estimated reference tissue conductivities, while results became unstable at lower SNR. We also set up a simulation for the reconstruction of the skull to brain conductivity ratio in which results were satisfying (correct skull:brain conductivity ratio, source localization errors smaller than 3.4 mm) up to noise levels equivalent to 25 dB SNR for the mainly tangentially oriented somatosensory reference sources. We found in our simulations that the most accurate source reconstructions were always associated with the correctly estimated conductivities (or conductivity ratio) and, moreover, that assuming an incorrect conductivity ratio had a profoundly negative effect on the source reconstruction accuracy.

In a last examination, we applied the LRCE to measured tactile Somatosensory Evoked Potentials (SEP) with the focus on estimating both the brain and the skull conductivity. With an SNR of 26.4 dB, the data were of similar quality to that in the second simulation study, which was based on a single equivalent current dipole model. As shown in numerous studies [83, 110], this source model is adequate because the early SEP component arises consistently from area 3b of the primary somatosensory cortex (SI) contralateral to the side of stimulation. Our explained variance to the measured data of about 99% for this source model further supports our choice. The results from the LRCE analysis were a brain conductivity of 0.48 S/m and a skull conductivity of 0.004 S/m. While this skull conductivity corresponds to the traditional value in the literature [5, 47, 51], the brain had a lower resistance than generally assumed [106]. Many recent papers have focused on the brain:skull conductivity ratio and large variability of results have been reported for this value including 80 [40], 72 [41], 42 [45], 25 [44], 23 [43], 15 [42] and 8 [111]. Because of the higher conductivity of the brain, with an estimated ratio of 120, our LRCE result is larger than the largest previously reported value of 80 [40].

The current results illustrate the feasibility of building an optimized volume conductor model with regard to both geometry and conductivity. As we have formulated it, such a study requires accurate head geometry, in this case from both T1- and PD-weighted MRI and cortical constraints on the sources. The highly conducting CSF should not be neglected in a model of the head and our procedure takes this compartment into account. By obtaining somatosensory evoked potential data, which allow independent reconstruction of the underlying bioelectric source, it is then possible to estimate the optimal conductivities for the individual subject using the proposed LRCE approach in highly realistic finite element models, provided that the data has a sufficient signal-to-noise ratio. A related finding from this study is that there is a trade off between the number of independent parameters that can be determined and the complexity of the assumed source model. The specific trade off point is also strongly influenced by the quality of the measured electric potentials. Thus the number of parameters that can be dependably estimated is a function of both the signal quality and the number and quality of *a priori* knowledge about, for example, the source location or orientation through a combination with fMRI or anatomical and/or functional arguments (e.g., a strong restriction of the source location to anatomically and physiologically reasonable areas close to the somatosensory SI area). In this context, others have suggested that by including MEG data in the scheme [51, 66], it will be possible to improve stability considerably. We note that our approach differs from others published studies [51, 66] with regard to both head modeling and conductivity optimization.

The success of the conductivity optimization approach and the more general advantages of customized geometric models suggest a procedure for clinical applications. First of all, one could use SEP data generated from a dependable source location with high SNR together with T1- and PD-MR images from the patient to construct a model that would be optimized for both geometric accuracy and individual conductivity values. With this volume conductor model in place, recorded potentials from more complex and clinically interesting sources could drive the inverse solution and source analysis.

Optimizing the volume conductor using the proposed LRCE method is an important step towards making effective use of simultaneous EEG/MEG source analysis [51]. Combining EEG and MEG modalities compensates the disadvantages of each approach, i.e., poor sensitivity of MEG to radial sources and the much stronger conductivity dependency of EEG. Using combined somatosensory evoked potentials and fields (SEP/SEF) in combination with T1- and PD-MRI should further stabilize the application of the presented LRCE method for the estimation of tissue conductivities. For the quasi-tangentially oriented P35 somatosensory source, MEG-SEF data can be exploited to strongly restrict the source location and especially its depth as shown elsewhere, [51, 66], so that the resolution of the proposed LRCE method with regard to the conductivities of the different compartments could be increased. With such data in hand, the presented LRCE method using FE volume conductor modeling might also contribute to the estimation of anisotropy ratios in the skull and brain compartments [3, 55, 112].

CHAPTER 6

MEG/EEG COMBINED SOURCE ANALYSIS FOR CONDUCTIVITY ESTIMATION

Although the EEG LRCE can estimate the tissue conductivity with low noise (high SNR) data, the higher noise levels can deteriorate the stability of the EEG LRCE procedure and eventually result in poor tissue conductivity estimation. In order to cope with the problem, we proposed a stabilizing method that imposes a constraint on the source parameter. The constraint is *a priori* information about the source that is acquired from the MEG dipole fit. The rational is that the MEG is not very sensitive to the tissue conductivity so that fitting an MEG dipole gives a good localization result even with uncertainty of tissue conductivity values. In Section 2.5, simulation results showed the low sensitivity of tissue conductivity on the source localization from measured MEG. This constrained LRCE approach uses sources from the MEG dipole fit in the EEG LRCE as a constraint on the source that is derived from MEG data. In the subsequent step the EEG LRCE searches for tissue conductivity. This method expects to strongly stabilize the LRCE procedure even with high noise data. In this study, we performed simulations with the proposed conductivity estimation procedure with multi EEG and MEG data. Also we applied the method to set of measured real SEP/SEF data.

6.1 Methods

6.1.1 MEG dipole fit

Here we describe the MEG dipole fit method that is used for the combined analysis. As in the Section 3.4.2, we can use an MEG dipole fit method based on the MEG lead field matrix for a given source space and the MEG sensors. The dipole fit equation will be

$$L_{MEG} \cdot J^{Ven} = \Phi_{sim}, \tag{6.1}$$

where J^{Ven} is a current source vector of dimension $3r \times 1$ defined at the discrete source space and Φ_{sim} is the simulated magnetic flux vector of dimension $m \times 1$. m is the number of MEG sensors and r is the number of permissible source locations. L_{MEG} has dimension $m \times 3r$ because we do not use the normal constraint.

The goal function to be minimized will be

$$g_f = min \, \|\Phi_{MEG} - \Phi_{sim}\|_2 = \min_{J_s} \|\Phi_{MEG} - L_s \cdot J_s\|_2. \tag{6.2}$$

In this equation, L_s $(m * 3k)$ indicates the reduced MEG lead field matrix for the current choice of source locations $s = (s_1, \cdots, s_k)$ with s_i the i-th source location $(1 \leq i \leq k)$. The procedure of the MEG dipole fit is the same as in the Section 3.4.2.

6.1.2 EEG/MEG combined analysis for conductivity estimation

The procedure is similar to that of the LRCE method with EEG data, except that the source parameter is no longer a free parameter but fixed during the calibration phase of LRCE. This method requires both EEG and MEG data and consists of two stages. The first calibration stage is to fit a dipole source with MEG data only by the procedure in the Section 6.1.1. As a result, we have the source parameter including source location and source moment (dipole direction and dipole strength). The second stage is to run the EEG LRCE in order to estimate tissue conductivity with constraints from the source parameter derived from the MEG dipole fit. The following summarizes the general procedure of the conductivity estimation with the MEG fitted source parameter. Here we use two types of constraints. One is the source location, and the other is all components of the source parameter. In the first case, the lead field matrix L will be $m \times 3$, since we fix location and allow moment to be changed during an optimization. In the latter case, the lead field matrix L will be $m \times 1$, since we fix location, direction, and magnitude to the MEG fitted dipole.

- Define a discrete estimate of the conductivity values for each tissue, i.e., fix all $\sigma_{ij_i}, 1 \leq i \leq l$
- Obtain a dipole source parameter J_s (location, orientation, magnitude) by MEG dipole fit method.

- Precompute the global influence matrix Λ corresponding to each of the possible conductivity combinations, given the source parameter or source location fitted in the previous step.
- **Repeat:**
  - Allow SA optimizer to choose a configuration of conductivities $\sigma = (\sigma_1, \cdots, \sigma_l)$
  - Get lead field matrix $L_s(\sigma)$ for the chosen conductivity configuration.
  - Compute a cost function, $g_f = min\|\Phi_{EEG} - L_s(\sigma)J_s\|_2$ with respect to source parameter J_s.
- **Until** cost function meets a tolerance criteria or the number of iterations exceeds a limit.
- Accept the configuration of conductivities as an optimum.

When the source is purely tangentially, we expect the source parameter from the MEG dipole fit to be accurate. However, since the reconstruction of non-tangential sources with MEG might lead to spurious orientation and strength components, we use the following iterative procedure for the combined EEG and MEG data to better take into account the strength and weaknesses of each modality. Therfore, the iterative approach could compensate an error in the radial component of the MEG fitted source moment with the combined EEG/MEG LRCE as in the Algorithm 2.

6.1.3 Simulation studies

For the study of the combined EEG/MEG conductivity estimation, we used the four compartment (scalp, skull, CSF, brain) isotropic FEM volume conductor model created with the same method described in Section 5.2.4 and 5.2.5. The FEM model consisted of 164903 nodes and 1,001,293 tetrahedra. We also created the discrete influence space of 21,302 nodes and 42,760 triangles by means of the method described in Section 5.2.6.

We used an EEG configuration with 63 electrodes and the MEG sensor configuration of the *Omega 2005* machine from VSM Medtech, Ltd. with 275 axial gradiometer measurement sensors. The measurement coils of this machine have a baseline of 50mm and a radius of 9mm. Additionally, the MEG system is equipped with a noise rejection technique that is described in Lanfer [4]. 29 reference sensors, being either magnetometers or axial or planar gradiometers with differing coil radii of between 7.76mm and 17.27mm

Algorithm 2 Iterative Approach

```
do while variance-to-data-not-well-explained
    step 1: MEG dipole fit. Result: Single SEF source at location $\underline{x}$ with orientation
            $\underline{o}_1$ and magnitude $m_1$.
    step 2: Keeping location and moment $(m_1 \cdot \underline{o}_1)$ constant, perform LRCE fit for
            brain and skull conductivity. Result: $\sigma_{brain_1}$ and $\sigma_{skull_1}$.
    step 3: Keeping only the dipole location $\underline{x}$ fixed and using the optimized volume
            conductor with conductivities. $\sigma_{brain_1}$ and $\sigma_{skull_1}$, compute $\underline{o}_2$ and $m_2$
            by means of a linear least square fit to the EEG data. Result: $\underline{o}_2$ and $m_2$
            (step 3 is necessary since $\underline{o}_1$ and $m_1$ might be spurious in the case that
            the source is not optimally quasi-tangential.
    step 4: Fix $\underline{x}$ and $\underline{o}_2$ and perform linear least square fit to the MEG data.
            Result: $m_3$.
    step 5: Keeping $\underline{x}$ and moment $\underline{o}_2 * m_3$ constant, perform EEG LRCE fit for
            brain and skull conductivity. Result: $\sigma_{brain_2}$ and $\sigma_{skull_2}$.
    step 6: Final result for best parameters: $\underline{x}, \underline{o}_2, m_3, \sigma_{brain_2}$ and $\sigma_{skull_2}$.
end
```

and a gradiometer baseline of 78.74mm, are situated in the dewar above the measurement sensors. Figure 6.1 shows a configuration of MEG measurement sensors and reference sensors.

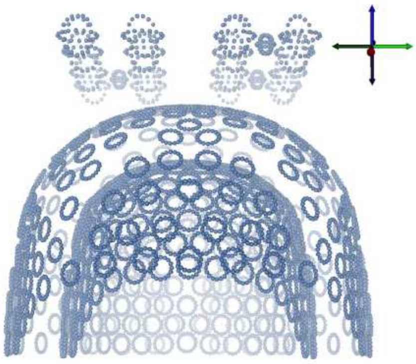

Figure 6.1. MEG Measurement sensors and reference sensors. FEM nodes were used to model the sensors. This visualization is adapted from [4]

We used a single quasi-tangential dipole source in the left somatosensory cortex region as a reference source for the simulation study. We chose the single source because the right finger tactile stimulus experiment evokes a single left somatosensory dipole. Given a dipole strength of 10nAm, the forward EEG and MEG simulations were carried out using the FE model with the reference conductivities (see below). Then we added noncorrelated noises to the reference EEG and MEG data, resulting in 40, 25, 20, and 15 dB SNR. The SNR was calculated as $SNR(dB) := 20 * \log_{10}(SNR)$ with $SNR := \frac{1}{\mathrm{S}}(\sum_{i=1}^{\mathrm{S}} \Phi^2_{[i]})/\sigma^2$, where $\underline{\Phi}_{[i]}$ is the noisy signal of either EEG or MEG at sensor i and $\underline{\sigma}$ the standard deviation of noise.

The following indicates that the reference source position is not an the source mesh node and the reference brain and skull conductivities are not conductivities in the discrete conductivity parameters.

- reference dipole source: pos(196.3 162.2 170.2), dir(0 1 0), mag(10 nAm)
- reference conductivity: brain(0.365), skull(0.0135), scalp(0.33), CSF(1.79)

Figure 6.2 shows the EEG potential maps (40dB, 25dB, and 20dB SNR) on the scalp, which were used as reference EEG data for the simulation study. The figure also shows the reference MEG magnetic flux maps on the MEG sensors located around the head.

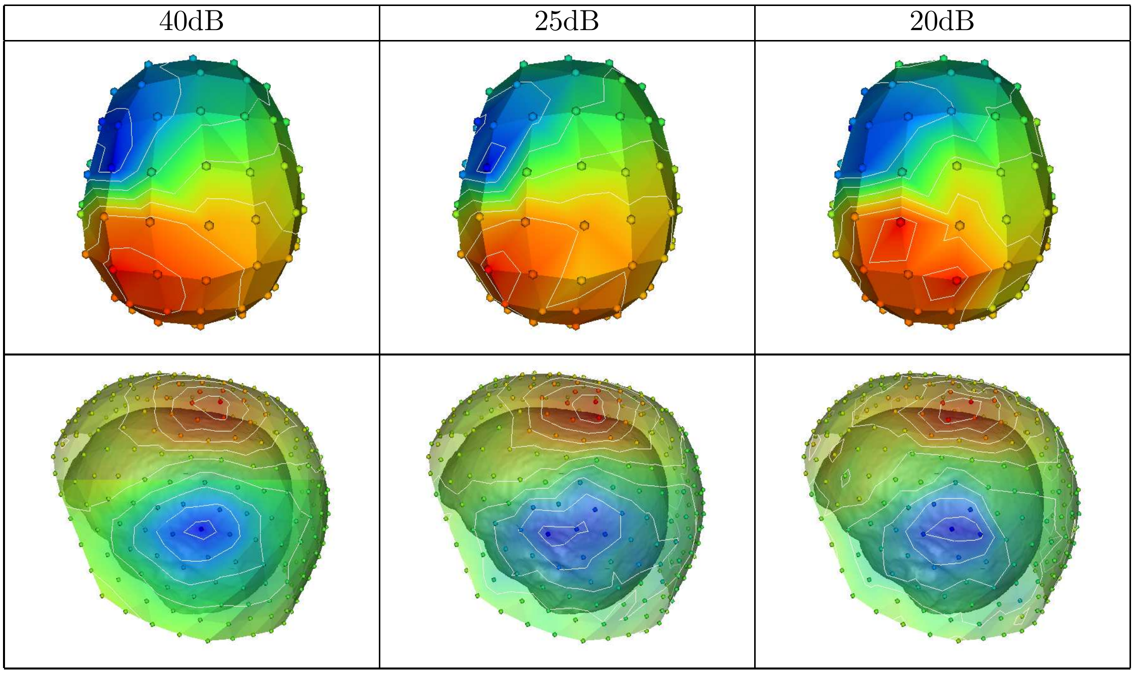

Figure 6.2. Simulated EEG (top) and MEG (bottom) maps with noise. Both maps are linearly interpolated among the sensors. The EEG map is on the scalp surface and the MEG map is over the head. White contour lines are iso-lines of electric potential and magnetic field amplitudes.

6.1.4 SEP/SEF measurement

We took a simultaneous SEP/SEF measurement of the tactile stimulus experiment for the same male subject as in Section 5.2.8. We used an MEG-compatible EEG cap with 63 electrodes following the 10% EEG system and the 304 channel MEG system as described above for the combined SEP and SEF measurements. Among the 304 MEG channels, 29 channels were used as reference sensors to reject environmental noises [4] as in the simulation study. The experimental protocol and the post processing procedure were the same as that of SEP measurement in Section 5.2.8. The SNR for SEP and SEF were 24dB and 30dB, respectively. As for the reference SEP/SEF data, we extracted the post stimulus P35 components from 63 EEG channels and 275 MEG channels. Figure 6.3 shows the P35 components of SEP and SEF data.

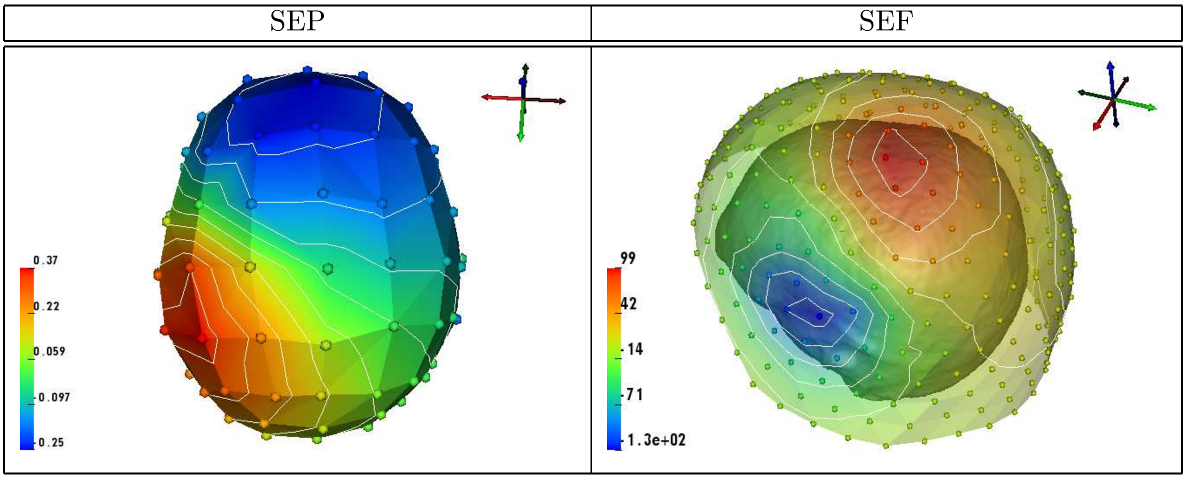

Figure 6.3. Sample measured SEP and SEF data (Left) Map of SEP potentials on the scalp surface. The small spheres indicate the EEG electrodes and the map is linearly interpolated among the electrodes. Electric potential is in mV. (Right) Magnetic field map of SEF over the head boundary. The small spheres indicate the MEG sensors. The field map is also linearly interpolated among the MEG sensors. The magnetic field is in fT. White contour lines indicate either iso-potential for SEP and iso-field lines for SEF.

6.2 Results

6.2.1 Skull conductivity estimation with single source

We first estimated skull tissue conductivity, given the reference volume conductor model. The following shows the setup of parameter for the estimation. The skull conductivity was assigned a value from a predefined set of possible skull conductivities that did not include exactly the reference skull conductivity (0.0135), which is intended to simulate a realistic situation.

$$\begin{aligned}
X &= \{s_{left_{somato}},\ \sigma_{skull}\} \\
\sigma_{brain} &= 0.332 S/m \\
\sigma_{skull} &\in \{0.0042,\ 0.0055,\ 0.0083,\ 0.0095,\ 0.0111, \\
&\quad 0.0123,\ 0.0133,\ 0.0144,\ 0.0166,\ 0.0221,\ 0.0415\} \\
\sigma_{scalp} &= \ 0.33,\ \ \sigma_{CSF} = \ 1.79\ S/m
\end{aligned}$$

In the first simulation, we fixed only the source location to the MEG fitted source and the source direction and the strength were allowed to change during the optimization. For the MEG dipole, we used a brain conductivity of 0.332 and skull conductivity of 0.0133, which were not the same values as the reference brain and skull conductivities. This is intend to simulate a realistic situation and also to avoid the so-called inverse crime. For the scalp and CSF, the conductivity values were 0.33 and 1.7 /S/m. Table 6.1 shows the results of skull conductivity estimation with the constraint of fixed source location. In the table, the left most column indicates the three different SNR levels of data for the MEG dipole fit used to locate the source. For each MEG SNR level, five different levels of EEG data noise were used for the estimation (SNR=15, 20, 25, 40, ∞ dB). The simulation results are tabulated for each EEG and MEG data combination. The table showed the estimated skull conductivity and the source moment with residual variance. Since we fixed only the location and were allowed to change the source moment during the optimization of EEG LRCE, the fixed source location in the table was from the MEG dipole fit, while the fitted direction and magnitude were from the EEG LRCE. Also included are the localization errors that measures the Euclidian distance between the reference source location and the MEG fitted source location. Overall, the single conductivity estimation gives a good estimation of skull conductivity at all noise levels, even though the conductivity diverges gradually from the reference value as the noise level increases. The best estimation was 0.0133, while the reference value is 0.0135. The worst was 0.221 in the case of 20dB MEG and 20dB EEG. The fitted directions for the MEG data of 40 dB and 25 dB SNR were very close to the reference direction of (0 1 0), while those of the 20dB MEG were more deviated from the reference than the other MEG data. The noise level of MEG data had an influence on the fitted dipole direction.

Table 6.1. Simulation study: EEG skull conductivity estimation by fixing **source location** to MEG fitted with $\sigma_{brain} = 0.332$, $\sigma_{skull} = 0.0133$. The MEG fit was carried out with simulated annealing and TSVD(10^{-2}). Explained residual variances of EEG and MEG are in %.

Data		σ_{skull}	location fixed	fitted source		explVar	
MEG	EEG			dir	mag	EEG	MEG
no	no	0.0133	x=196.8 y=163.7 z=171.7 err=2.2 mm	(-0.08 1 -0.02)	9.5	99.9	99.0
	40dB	0.0133		(-0.05 1 -0.05)	9.5	98.0	99.0
	25dB	0.0144		(-0.16 0.98 -0.03)	9.2	95.5	98.7
	20dB	0.0166		(-0.05 1 0.03)	8.6	91.2	99.6
	15dB	0.0144		(-0.12 0.99 0.04)	9.3	85.5	98.3
40dB	no	0.0133	x=196.8 y=163.7 z=171.7 err=2.2 mm	(-0.08 1 -0.02)	9.5	99.9	98.1
	40dB	0.0133		(-0.05 1 -0.05)	9.5	98.0	98.2
	25dB	0.0144		(-0.16 0.98 -0.03)	9.2	95.5	97.7
	20dB	0.0166		(-0.05 1 0.03)	8.6	91.2	98.7
	15dB	0.0144		(-0.12 0.99 0.04)	9.3	85.5	97.4
25dB	no	0.0144	x=196.8 y=163.7 z=169.7 err=1.7 mm	(-0.09 1 -0.01)	9.2	99.9	94.3
	40dB	0.0144		(0.06 1 -0.03)	9.2	99.1	94.0
	25dB	0.0144		(-0.17 0.99 -0.01)	9.2	95.6	94.2
	20dB	0.0166		(-0.07 1 0.03)	8.6	91.1	94.2
	15dB	0.0166		(-0.13 0.99 0.04)	8.9	85.7	94.3
20dB	no	0.0166	x=195.8 y=157.7 z=169.7 err=4.6 mm	(-0.29 0.95 -0.13)	10.2	99.6	89.5
	40dB	0.0166		(-0.28 0.95 -0.15)	10.1	98.5	89.2
	25dB	0.0166		(-0.35 0.93 -0.13)	10.5	95.2	89.0
	20dB	0.0221		(-0.28 0.95 -0.1)	9.1	90.1	87.1
	15dB	0.0166		(-0.32 0.94 -0.08)	10.4	84.3	89.2

Table 6.2 shows the results of skull conductivity estimation with the EEG LRCE by fixing the source parameter (both source location and moment) to the MEG fitted dipole. The best estimation of skull conductivity was 0.0144 and the worst estimation was 0.0055, where the reference is 0.0136. The explained residual variance of 20dB MEG data were from 52% to 62.2%, while that of other MEG data were from 80% to 99.2%. It seems that the source moment constraint made the fit worse in the case of 20dB MEG data than the source location constraint in Table 6.1. The constraint of source moment seems not to reflect the actual moment. This results could indicate that incorrect radial component of source moment plays a negative role in the estimation. As a cure for the problem, the proposed iteration method must be applied. Also, the table shows that the fitted source locations by MEG data of no noise (2.2 mm), 40 dB SNR (2.2 mm), and 25 dB SNR (1.7

mm) were close neighboring nodes to the reference source, while that of 20dB MEG was more away (4.6 mm) from the reference location.

Table 6.2. Simulation study: EEG skull Conductivity estimation by fixing **source location and moment** to MEG fitted with the non-reference conductivities of $\sigma_{brain} = 0.332$, $\sigma_{skull} = 0.0133$. Explained residual variances of EEG and MEG are in %.

Fixed to MEG fitted source	noise	no			40dB		
	location	(196.8 163.7 171.7)			(196.8 163.7 171.7)		
	direction	(-0.15 0.98 -0.09)			(-0.15 0.98 0.09)		
	magnitude(nAm)	8.7			8.7		
	location error	2.2 mm			2.2 mm		
	noise	σ_{skull}	explVar		σ_{skull}	explVar	
			EEG	MEG		EEG	MEG
EEG data (dB)	no	0.0166	99.2	99.7	0.0166	99.2	98.8
	40dB	0.0144	98.0	99.7	0.0166	98.1	98.8
	25dB	0.0166	95.3	99.7	0.0166	95.3	98.8
	20dB	0.0144	90.0	99.7	0.0144	90.1	98.8
	15dB	0.0166	85.0	99.7	0.0166	85.0	98.8
Fixed to MEG fitted source	noise	25dB			20dB		
	location	(196.8 163.7 169.7)			(195.8 157.7 169.7)		
	direction	(-0.24 0.96 -0.12)			(0.14 0.92 0.36)		
	magnitude(nAm)	8.7			11.2		
	location error	1.7 mm			4.6 mm		
	noise	σ_{skull}	explVar		σ_{skull}	explVar	
			EEG	MEG		EEG	MEG
EEG data (dB)	no	0.0083	94.0	94.8	0.0055	61.9	91.5
	40dB	0.0083	92.9	94.8	0.0055	62.2	91.5
	25dB	0.0095	92.2	94.8	0.0055	52.9	91.5
	20dB	0.0083	84.9	94.8	0.0055	58.6	91.5
	15dB	0.0083	80.0	94.8	0.0055	52.0	91.5

6.2.2 Brain and skull conductivity estimation with single source

We estimated the brain and the skull tissue conductivities with the EEG/MEG combined method, given the single dipole source. The estimated conductivity parameters were the same as in the previous section, except for the addition of brain conductivity. We used three conductivity values for the brain that all differenced from the reference brain conductivity (0.365). We also used predefined estimates for the skull conductivity that did not include the reference value (0.0135). The following shows the parameters we used during the optimization.

$$
\begin{aligned}
X &= \{s_{left_{somato}},\ \sigma_{brain},\ \sigma_{skull}\} \\
\sigma_{brain} &\in \{0.12,\ 0.332,\ 0.48\ S/m\} \\
\sigma_{skull} &\in \{0.0042,\ 0.0055,\ 0.0083,\ 0.0095,\ 0.0111, \\
&\quad\ 0.0123,\ 0.0133,\ 0.0144,\ 0.0166,\ 0.0221,\ 0.0415\} \\
\sigma_{scalp} &= 0.33, \\
\sigma_{CSF} &= 1.79\ S/m
\end{aligned}
$$

First of all, we used the constraint of the source location fitted from the MEG dipole fit in order to estimate the brain and skull conductivities. The same conductivity values (brain=0.332, skull=0.0133 S/m) as in the previous section are used for the MEG dipole fit. Table 6.3 shows the estimation results with the EEG and MEG data. The estimated skull conductivity varies from 0.0133 to 0.0166 for all noise levels (reference values was 0.0135). The estimated brain conductivity was either 0.33 or 0.48 (reference was 0.365).

Table 6.4 shows the conductivity estimation result of the combined EEG/MEG method by fixing the source parameter (source location and moment) to the MEG fitted. For the case of no noise and 40dB MEG data, the brain conductivity was estimated as 0.332 for all EEG noise levels, which is the closest value to the reference conductivity value. The estimated skull conductivity values differed from the reference value by 6.7% to 23.5%. For the case of 25dB and 20dB MEG data, however, the estimated brain conductivity was 0.48, which differed more from the reference than that of the 40dB MEG data. As described in the previous section, the MEG fitted source moment may not be correct due to the poor radial sensitivity of MEG and the higher MEG noise. The low explained residual variances in the case of 20dB MEG data suggests that the fitted parameter did explain the reference EEG data well enough, even though they were best fits that would possible with the method.

6.2.3 Iteration Approach

In an effort to compensate for the poor radial sensitivity of MEG, we applied the iteration method proposed in the Section 6.1.2 to the estimation results in Table 6.4. Table 6.5 shows the results after a single iteration. The estimated brain conductivity for

Table 6.3. Simulation study: EEG Brain & Skull conductivity estimation by fixing **source location** through MEG fitting with the non-reference conductivities of $\sigma_{brain} = 0.332$, $\sigma_{skull} = 0.0133$. (Reference conductivities; $\sigma_{brain} = 0.365$, $\sigma_{skull} = 0.0135$. Explained residual variances of EEG and MEG are in %.

Data		σ_{brain}	σ_{skull}	location fixed	fitted source		explVar	
MEG	EEG				dir	mag	EEG	MEG
no	no	0.332	0.0133		(-0.1 1 0)	9.5	99.9	99.0
	40dB	0.332	0.0133	x=196.8	(-0.1 1 -0.1)	9.5	99.0	99.0
	25dB	0.48	0.0133	y=163.7	(-0.2 0.98 -0.0)	11.5	95.5	82.3
	20dB	0.48	0.0166	z=171.7	(-0.1 0.99 0)	10.4	91.2	94.0
	15dB	0.48	0.0144	err=2.2 mm	(-0.1 0.99 0))	9.3	82.3	98.0
40dB	no	0.332	0.0133		(-0.1 1 0)	9.5	99.9	98.1
	40dB	0.332	0.0133	x=196.8	(-0.1 1 -0.1)	9.5	99.0	98.2
	25dB	0.48	0.0133	y=163.7	(-0.2 0.98 -0.0)	11.5	95.5	81.5
	20dB	0.48	0.0166	z=171.7	(-0.1 0.99 0)	10.4	91.2	93.1
	15dB	0.48	0.0144	err=2.2 mm	(-0.1 0.99 0))	9.3	82.3	97.2
25dB	no	0.332	0.0144		(-0.1 1 0)	9.2	99.9	94.3
	40dB	0.332	0.0144	x=196.8	(-0.1 1 0)	9.2	99.1	94.0
	25dB	0.48	0.0133	y=163.7	(-0.2 0.97 0)	11.5	95.6	81.0
	20dB	0.48	0.0166	z=169.7	(-0.1 0.99 0.0)	10.4	91.1	90.2
	15dB	0.332	0.0166	err=1.7 mm	(-0.1 0.99 0.0)	8.9	85.7	94.3
20dB	no	0.48	0.0144		(-0.3 0.95 -0.1)	12.5	99.6	87.7
	40dB	0.48	0.0144	x=195.8	(-0.3 0.95 -0.1)	12.4	98.5	88.2
	25dB	0.48	0.0166	y=157.7	(-0.4 0.93 -0.1)	12.4	95.2	87.0
	20dB	0.48	0.0166	z=169.7	(-0.3 0.96 -0.1)	11.5	90.1	89.3
	15dB	0.48	0.0144	err=4.6 mm	(-0.3 0.94 -0.1)	12.8	84.3	85.3

all cases was 0.332, except the 20dB EEG and 20dB MEG data. The estimated skull conductivities were 0.0166 for the no noise, 40dB and 25dB MEG cases. The residual variances of the 20dB MEG data are much better than those of Table 6.4. Overall, this compensative iteration approach with the combined MEG/EEG method produced more stable results than the combined method without an iteration in estimating the brain and skull conductivity with high noise measurement data.

The signal to noise ratio (SNR) represents the overall root mean squared level amount of noise in a signal. It does not specify how the noise is distributed over the space, i.e., scalp EEG electrodes and the MEG sensors. This means that it is possible to have different spatial topographies for the same SNR values. In order to reveal the sensitivity of the results to different noise configurations, we performed simulation studies with ten different EEG/MEG noise configurations of the 20dB SNR for MEG and EEG data.

Table 6.4. Simulation study: EEG Brain & Skull Conductivity estimation by fixing **source location and moment** to MEG fitted with the non-reference conductivities of $\sigma_{brain} = 0.332$, $\sigma_{skull} = 0.0133$. Explained residual variances of EEG and MEG are in %.

Fixed to MEG fitted source	noise	no	40dB
	loc	(196.8 163.7 171.7)	(196.8 163.7 171.7)
	dir	(-0.15 0.98 -0.09)	(-0.15 0.98 0.09)
	mag	8.7	8.7

	noise	conductivity		explVar		conductivity		explVar	
		σ_{brain}	σ_{skull}	EEG	MEG	σ_{brain}	σ_{skull}	EEG	MEG
EEG data (dB)	no	0.332	0.0166	99.2	99.7	0.332	0.0166	99.2	98.8
	40dB	0.332	0.0144	98.0	99.7	0.332	0.0166	98.1	98.8
	25dB	0.332	0.0166	95.3	99.7	0.332	0.0166	95.3	98.8
	20dB	0.332	0.0144	90.0	99.7	0.332	0.0144	90.1	98.8
	15dB	0.332	0.0166	85.0	99.7	0.332	0.0166	85.0	98.8

Fixed to MEG fitted source	noise	25dB	20dB
	loc	(196.8 163.7 169.7)	(195.8 157.7 169.7)
	dir	(-0.24 0.96 -0.12)	(0.14 0.92 0.36)
	mag	8.7	11.2

	noise	conductivity		explVar		conductivity		explVar	
		σ_{brain}	σ_{skull}	EEG	MEG	σ_{brain}	σ_{skull}	EEG	MEG
EEG data (dB)	no	0.48	0.0144	94.9	94.1	0.48	0.0083	63.9	90.6
	40dB	0.48	0.0144	94.0	94.1	0.48	0.0083	64.1	90.6
	25dB	0.48	0.0166	92.0	94.1	0.48	0.0083	55.0	90.6
	20dB	0.48	0.0133	85.8	94.1	0.48	0.0083	60.7	90.6
	15dB	0.48	0.0166	81.8	94.1	0.48	0.0083	53.5	90.6

Different sets of random noise of 20dB SNR were generated and added to the noise free reference data such that each set had topologically different noise configuration. Table 6.6 shows the results of the iteration method for the ten datasets. As shown in the table, the estimated conductivities were different from one another. Nevertheless, the averaged conductivity values (brain=0.36 and skull=0.0164) over the ten cases gives a close approximation of the reference conductivities (brain=0.365, skull=0.0135). The average (± standard deviation) of the MEG fitted source positions over the ten datasets was (196.5±0.7 161.9±3.8 170.4±0.9) with a localization error of 3.6 mm.

6.2.4 Application to SEP/SEF data

We applied the proposed MEG/EEG combined analysis for the conductivity estimation to a real SEP/SEF dataset from the experiment described in Section 5.2.8. We fixed scalp and CSF conductivities and allowed the brain and skull conductivities to vary as

Table 6.5. Brain and skull tissue conductivity estimation with the proposed iteration method based on the combine EEG/MEG analysis. Explained residual variances of EEG (varEEG) and MEG (varMEG) are in %.

MEG no noise							
EEG	$\mathbf{o_2}$	m_2	$\mathbf{m_3}$	$\sigma_{\mathbf{brain_2}}$	$\sigma_{\mathbf{skull_2}}$	varEEG	varMEG
no noise	(-0.08 1.00 -0.03)	8.8	8.8	0.332	0.0166	99.2	99.7
40dB	(-0.06 1.00 -0.05)	9.2	8.9	0.332	0.0166	99.0	99.5
25dB	(-0.16 0.99 -0.03)	8.8	8.5	0.332	0.0166	95.3	99.6
20dB	(-0.05 1.00 0.03)	9.0	8.8	0.332	0.0166	90.1	99.7
15dB	(-0.12 0.99 0.03)	8.9	8.5	0.332	0.0166	85.0	99.4

MEG 40dB noise							
EEG	$\mathbf{o_2}$	m_2	$\mathbf{m_3}$	$\sigma_{\mathbf{brain_2}}$	$\sigma_{\mathbf{skull_2}}$	varEEG	varMEG
no noise	(-0.08 1.00 -0.03)	8.8	8.8	0.332	0.0166	99.9	98.8
40dB	(-0.06 1.00 -0.06)	8.9	8.9	0.332	0.0166	99.0	98.6
25dB	(-0.16 0.99 -0.03)	8.8	8.5	0.332	0.0166	95.4	98.6
20dB	(-0.05 1.00 0.03)	9.0	8.8	0.332	0.0166	91.1	98.8
15dB	(-0.12 0.99 0.03)	8.9	8.5	0.332	0.0166	85.5	98.6

MEG 25dB noise							
EEG	$\mathbf{o_2}$	m_2	$\mathbf{m_3}$	$\sigma_{\mathbf{brain_2}}$	$\sigma_{\mathbf{skull_2}}$	varEEG	varMEG
no noise	(-0.14 0.99 -0.01)	11.2	8.6	0.332	0.0166	99.6	94.5
40dB	(-0.12 0.99 -0.03)	11.2	8.7	0.332	0.0166	98.8	94.4
25dB	(-0.22 0.97 -0.01)	10.8	8.4	0.332	0.0166	95.2	94.1
20dB	(-0.12 0.99 0.04)	11.2	8.7	0.332	0.0166	90.8	94.4
15dB	(-0.19 0.98 0.04)	10.9	8.5	0.332	0.0166	85.4	93.9

MEG 20dB noise							
EEG	$\mathbf{o_2}$	m_2	$\mathbf{m_3}$	$\sigma_{\mathbf{brain_2}}$	$\sigma_{\mathbf{skull_2}}$	varEEG	varMEG
no noise	(-0.29 0.95 -0.09)	15.1	10.8	0.332	0.0144	99.2	90.1
40dB	(-0.28 0.96 -0.11)	15.1	10.9	0.332	0.0133	99.0	90.5
25dB	(-0.36 0.96 -0.09)	15.7	10.8	0.332	0.0144	95.3	88.8
20dB	(-0.28 0.96 -0.05)	14.6	10.7	0.48	0.0221	90.0	89.7
15dB	(-0.32 0.95 -0.04)	15.5	10.6	0.332	0.0166	85.0	88.9

parameters of the optimization . The sets of the brain and skull conductivities include the following values from the literature.

Table 6.6. Proposed iterative EEG/MEG combined analysis for conductivity estimation with MEG (20dB) and EEG (20dB) data, given the 10 sets of different EEG/MEG noise configurations. Explained residual variance is in %.

	Before iteration		parameters during iteration			After iteration		explVar	
#	σ_{br_1}	σ_{sk_1}	o_2	m_2	m_3	σ_{br_2}	σ_{sk_2}	EEG	MEG
1	0.48	0.0083	(-0.28 0.96 -0.05)	14.6	10.7	0.48	0.0221	90.1	89.7
2	0.48	0.0123	(-0.26 0.96 -0.11)	13.5	10.7	0.332	0.0166	91.1	90.4
3	0.48	0.0083	(-0.29 0.94 -0.15)	15.5	11.1	0.332	0.0144	91.3	90.4
4	0.48	0.0221	(-0.13 0.98 0.13)	9.4	8.5	0.332	0.0144	90.4	89.7
5	0.332	0.0123	(-0.06 1.00 -0.02)	9.3	8.9	0.332	0.0123	91.0	90.7
6	0.48	0.0055	(-0.33 0.94 -0.12)	18.4	11.2	0.332	0.0123	91.8	89.8
7	0.48	0.0221	(-0.15 0.99 0.075)	10.3	9.0	0.332	0.0166	91.7	91.3
8	0.48	0.0221	(-0.17 0.98 -0.11)	9.7	8.9	0.48	0.0221	91.3	90.0
9	0.332	0.0166	(-0.04 1.00 0.035)	9.0	8.8	0.332	0.0166	91.2	90.8
10	0.332	0.0166	(-0.15 0.98 -0.11)	8.2	7.8	0.332	0.0166	91.1	89.9
mean	0.44	0.0146	(-0.19 0.97 -0.04)	11.8	9.6	0.36	0.0164	91.1	90.3
std	0.07	0.0062	(0.1 0.02 0.1)	3.5	1.2	0.06	0.0034	0.5	0.5

$$
\begin{aligned}
X &= \{s_{somato},\ \sigma_{brain},\ \sigma_{skull}\} \\
\sigma_{scalp} &= \ 0.33\ S/m,\ \sigma_{CSF} =\ 1.79\ S/m \\
\sigma_{brain} &\in \{0.12,\ 0.332,\ 0.48,\ 0.57\ S/m\} \\
\sigma_{skull} &\in \{0.00066, 0.00083, 0.00095, 0.0011, 0.0013, 0.0015, 0.0018, 0.0021, 0.0024, 0.0028, \\
&\quad 0.0033, 0.0042, 0.0046, 0.0055, 0.0079, 0.0133, 0.0144, 0.0221, 0.0332, 0.0415, 0.0664\}
\end{aligned}
$$

We used four different approaches to estimate the conductivities. The first was EEG-only LRCE, and the second one was the EEG LRCE by fixing the source location based on MEG fitting. The third approach was the EEG LRCE by fixing the source location and moment (magnitude and direction) based on MEG. The fourth was the iterative method based on the results of the third approach. For the MEG dipole fit, we used a simulated annealing on the source space with $\sigma_{brain} = 0.332$, $\sigma_{skull} = 0.0042\ S/m$. TSVD was used for the regularization with the relative cut off of 10^{-2}.

Table 6.7 shows the results of conductivity estimation by the four different methods. Depending on the source constraint, the estimated skull conductivity varied widely, while the brain conductivity remained the same at 0.48. The EEG and MEG residual variances reflect the type of constraints; with the source location fixed, the result of EEG LRCE gave a good EEG residual variance because the source moment was fitted to optimize the EEG data. With the source location and moment fixed, the conductivity estimation

Table 6.7. SEP/SEF study: Brain and skull Conductivity estimation by the four different methods. The conductivities of the CSF and scalp were 1.79 and 0.33 S/m, respectively. Explained residual variances of EEG (varEEG) and MEG (varMEG) are in %, and Mag is in nAm

		EEG LRCE	MEG/EEG		
			Loc fixed	Loc/Mom fixed	Iteration
σ_{brain}		0.12	0.48	0.48	0.48
σ_{skull}		0.0055	0.0055	0.0011	0.0015
src loc	x	198.8	196.8	196.8	196.8
	y	155.7	163.7	163.7	163.7
	z	171.7	169.7	169.7	169.7
src dir	dx	0.62	0.58	0.24	0.59
	dy	0.69	0.79	0.81	0.79
	dz	-0.39	-0.21	-0.53	-0.16
src mag		2.6	6.7	15.1	15.4
varEEG		97.3	97.9	74.1	96.4
varMEG		-	61.0	95.8	88.0

gave a good MEG residual variance because the source parameters came from the best fit MEG data. Even though the fixed source parameter from the MEG fit was used for the EEG LRCE, the iteration revised the radial component of the source moment from the EEG fit.

Figure 6.4 is the plot of explained residual variance with respect to the fixed skull conductivity in order to show the goal function to be optimized. The residual variances in Figure 6.4 (a) were computed with the estimation result of EEG LRCE, given a fixed source location from the MEG dipole fit. The curve is very flat in the region of the maximum, which means that any skull conductivity in the flat region does not make a difference in terms of the estimation quality. However, the variance curves in Figure 6.4 (b) computed with the iterative MEG/EEG combined method were very sensitive to the skull conductivity variation. The peak variances of the four brain conductivities were agreed very closely; the difference between the minimum and the maximum over the peaks of four curves was only 1.5%. However, variance changed sharply with skull conductivity in each case, dropping to 70% for shift of 1.5-1.75 in skull conductivity. Also, the value of σ_{skull} corresponding to the maximum variance changed with the value of σ_{brain}. These result suggest that the brain conductivity has less influence to the estimation result than the skull conductivity.

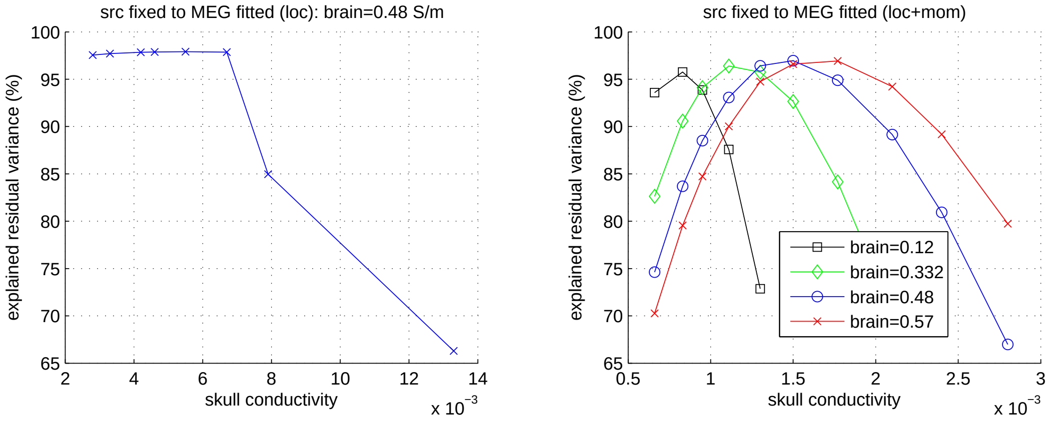

(a) (b)

Figure 6.4. Plot of residual variance. (a) The explained residual variance was computed with the parameters that resulted from the EEG LRCE with the fixed source location of MEG dipole fit. (b) The explained residual variance was computed with the estimated parameter from the iterative MEG/EEG combined method. Also shown with the other brain conductivities.

Figure 6.5 shows the potential on a sagittal cut plane with the source fitted with the iterative combined SEP/SEF method. It also shows the current flow on the scalp surface generated by the reconstructed dipole source and the reference SEP. Figure 6.6 shows the magnetic field due to the source fitted with the iterative combined SEP/SEF method at the MEG sensors.

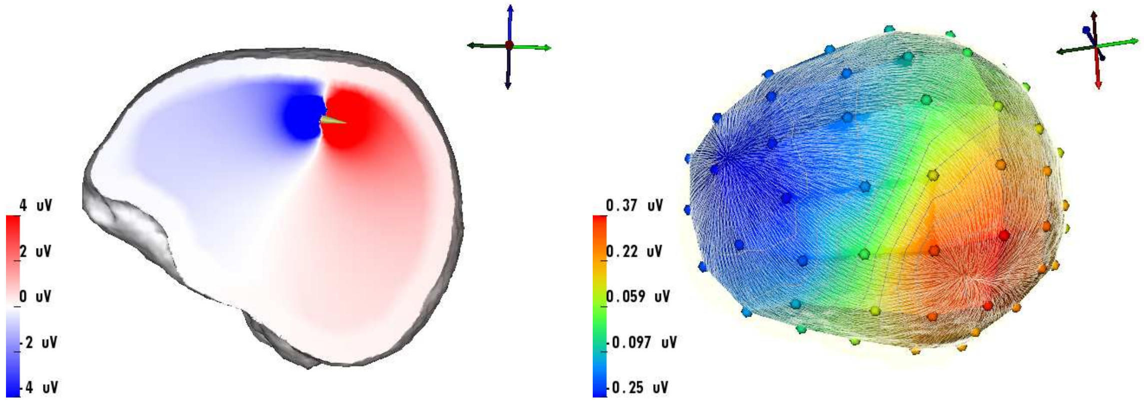

Figure 6.5. Results after one iteration of combined approach. Left: potential map on the sagittal cut with fitted source after an iteration. Right: Current on the scalp surface (yellow lines) after an iteration together with the original SEP coded by color.

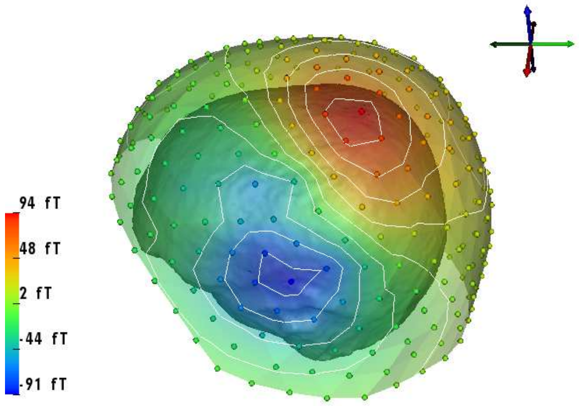

Figure 6.6. Magnetic field map on the MEG sensors over the head boundary. The field was computed with the iteratively fitted source and conductivities.

6.3 Discussion and Conclusion

The conductivity estimation with the combined MEG/EEG source analysis opens up a possibility of estimating an individual's own tissue conductivity and then using the resulting customized head model to localize the desired pathological sources. In contrast to the EEG-only LRCE, the MEG/EEG combined analysis strongly stabilizes the inverse solution process, mainly due to the constraints on the source parameters from the MEG modality. The results of these simulation studies support such a possibility. Unlike the EEG-only LRCE, the combined method gives more stable estimation even with the low SNR EEG data. The accuracy of the conductivity estimation seems to depend more on the MEG SNR and less on the EEG SNR. This means that the quality of the constraint, i.e., the accuracy of the source parameter that is obtained from the MEG dipole fit, has more influence on the estimation results than any other typical factor.

When the source was tangentially positioned, the MEG dipole fit was able to correctly fit source moment. In the case of a non-tangential source, however, the MEG fitted source moment did not fully recover the radial component of the source, probably due to the poor sensitivity to radial component of the MEG modality. The proposed iterative method is an attempt to take advantage of the EEG modality that has the same radial and tangential sensitivity of the source, in order to compensate for the unrecovered radial source moment from MEG. The simulation results clearly show the effectiveness of the iterative approach. Taking into account both modalities' advantages resulted in the strong possibility of customizing an individual volume conductor model in terms of tissue conductivity.

The MEG/EEG combined analysis produced a type of goal function that has a deep valley. The residual variances (a way of representing the goal function) in the MEG/EEG combined analysis with different constraints (Figure 6.4) clearly showed the characteristic of goal functions. While the one that took only source location into the constraint gave a very flat curve near the best fit, the one with the full accommodation of source parameters with iteration gave a quadratic curve that showed a clear peak. Full commitment of source parameter including source location, direction and magnitude makes a deep goal function to be optimized.

The application of those approaches to real SEP/SEF data resulted in values of 0.48 S/m for brain conductivity and 0.0015 S/m for skull conductivity. The estimated brain conductivity lay within the reported values from the literature, however, the skull conductivity was much smaller than the lower limit of the reported values that fall into the range of 0.0133∼0.0042 S/m. The sensitivity of the skull thickness on the forward computation was relatively larger than that of other tissues. Therefore, it is reasonable to investigate the influence of the skull tissue modeling on the forward computation. In fact, the skull is in fact made of compacta (hard bone) and spongiosa (soft tissue); the compacta is of high electric resistance and the spongiosa is of low resistance. Because of these components of skull tissue, the skull conductivity is often modeled as an effective anisotropy that captures the lower conductivity in the radial direction and the higher conductivity in the tangential direction. We might consider the effect of skull anisotropy on the conductivity estimation.

We also point out that with regard to the skull conductivity modeling, it was recently reported in [113] that it might not be sufficient to approximate the influence of outer compacta, spongiosa and inner compacta by means of a radial-to-tangential anisotropy as proposed in [55]. Accordingly, it is reasonable to model the three layeredness of skull tissue and to estimate the skull conductivities based on the skull tissue model. A modeling of the three-layeredness can easily be done in a high-resolution 1mm hexahedra FE approach as long as a segmentation of the spongiosa is available.

We could apply the combined MEG/EEG conductivity estimation to other event related evoked data such as VEP/VEF (Visaul Evoked Potential/Field) and AEP/AEF (Auditory Evoked Potential/Field). Having those data could further validate the conductivity estimation procedure. In the long run, we could have a customized conductivity profile of a subject by means of the MEG/EEG evoked data and the proposed conductivity estimation procedure. This specific conductivity profile would then be used clinically for more routine EEG analysis that has a strong dependency on the conductivity.

As briefly described in the introduction, a recent study of Huang *et al* [66] tried to estimate tissue conductivity ratio with a sphere model and boundary element model. The study did not fully account for absolute tissue conductivity values, but tried to find a best fit ratio among head tissue conductivities. He used the MEG and EEG combined modality for the study and decomposed the MEG fitted source moment into the radial and tangential components in order to use only the tangential component that can be correctly obtained from the MEG. For the sphere model, the radial source direction is obvious, but for the boundary element model that has the geometry from the realistic head image, getting the radial direction is not an obvious procedure. He proposed to extract the radial source from the MEG gain matrix at the fitted source location. SVD (Singular Value Decomposition) decomposed the MEG gain matrix and give three eigenvalues and three eigenvectors that represent three orthogonal directions. Out of the three eigenvalues, the smallest eigenvalue is presumed to be from the least sensitivity direction, which is the radial direction in MEG. The eigenvector corresponding this eigenvalue is then the radial direction. The other two eigenvectors represent two tangential directions.

CHAPTER 7

SUMMARY AND FUTURE WORK

7.1 Summary and Conclusions

The research of this dissertation divides naturally into three projects, all based on the numerical method of finite element volume conductor models. The first project sought to evaluate numerical accuracy and computational cost of a forward simulation for three FE dipole models and three numerical FE solvers using a spherical FEM head model. Second, we developed a new method to expand the basic source localization approach in a way that also estimates skull and brain tissue conductivities from EEG data, given a realistic, four compartment FEM head model. Third, we further extended this approach of tissue conductivity estimation by adding MEG data into the EEG based estimation method, thus achieving another goal of maximizing the utilization of both compensating modalities. The long-term goal of this research is to create subject specific volume conductor models in terms of head geometry and tissue conductivity.

The summary and the important outcomes of each research project are described in the following.

1. Chapter 4 described the evaluation of FEM forward solution accuracy with respect to three dipole models (Venant model, partial integration method, and subtraction approach) and the computational efficiency with respect to three finite element solvers (Jacobi-CG, IC-CG, and AMG-CG). Despite many years of research in the area of finite element solvers, the relative novelty of the multigrid method and especially the more sophisticated dipole source representations made this a unique, timely, and practically essential study. We modeled the head as a four compartment (scalp, skull, CSF, and brain) sphere. A large number of forward computations were carried out with respect to a set of parameters including solver accuracy, dipole location, dipole orientation, finite mesh size, and brain mesh constraint, for a given choice of the dipole model and the numerical solver. We computed the accuracy of the forward simulation by the error metrics of RE,

RDM, and MAG at given EEG electrode locations, based on the forward solution of an analytic sphere model. We also measured wall-clock time for each forward computation to evaluate computational efficiency. Simulation results showed that the subtraction approach was the most accurate over all source locations and did not depend on the mesh size of brain compartment where the source was placed. Nevertheless, the Venant dipole model showed a compatible performance in the solution accuracy, as long as the mesh was regular and of high resolution. Another benefit of the Venant dipole is its high computational efficiency due to the nature of a simple implementation. Concerning the solver efficiency, the AMG-CG iterative solver outperformed the other solvers due to its superior preconditioning quality.

2. Chapter 5 described a new method that extends source localization to include an estimation of tissue conductivity. The motivation for this approach comes from the persistent discrepancies in the values of tissue conductivity that are found in the literature. It may well be that tissue conductivity varies among individuals or even over times. Hence a solution that adjusts tissue conductivity values based on individual and time specific electrical measurements has the potential to dramatically improve source localization by customizing it to situation. The low resolution conductivity estimation (LRCE) method was implemented based on a global optimizer and the lead field approach. By this method, initially a global lead field matrix is created with possible source locations and possible conductivity values. Based on EEG measurements and using a global optimizer and a linear least-square fit, the sources are evaluated in a predefined source space and, similarly, the conductivity values are evaluated in their predefined set of values, such that the LRCE finds an optimal combination of source and conductivity that meets a minimum norm criteria. The feasibility of the LRCE was tested with the several scenarios of source and conductivity configurations, including single source and brain/skull conductivities, two sources and skull conductivity, and two sources and brain/skull conductivities. The two sources were located in the right and left somatosensory area and oriented either quasi-tangentially or quasi-radially. We used a four compartment (scalp, skull, CSF and brain), realistic FEM conductor model that was created from the MR images of a subject. The source space was extracted from the 2 mm under the outer surface of the brain, which represents a layer of gray matter. The predefined conductivity values were collected from

the literature. The simulation results showed that the LRCE method correctly estimated conductivities as long as the EEG data had SNRs better than above 25dB, but was unable to estimate them correctly with the low SNR data. We also applied the method to real somatosensory evoked EEG data and estimated brain and skull conductivity to be 0.48 S/m and 0.004 S/m, respectively, values that are within those in the literature.

3. Chapter 6 described a further extension of the LRCE approach that combined MEG/EEG source analysis and estimated tissue conductivity with even better accuracy and robustness. In order to improve the EEG based conductivity estimation, we introduced *a priori* constraints on the source parameter based on MEG measurement. The rational for this approach is the fact that MEG signals are less affected by tissue conductivities than EEG signals, although they are more prone to errors in source orientation. Thus we sought to use MEG signals to estimate source localization as a constraint on a subsequent application of the LRCE approach. The EEG LRCE method in Chapter 5 was modified to accommodate the source constraint from the MEG dipole fit. Moreover, we implemented an iteration scheme to compensate for the poor radial sensitivity of the MEG modality. We tested the MEG/EEG conductivity estimation with the same realistic FEM head model, given a quasi-tangentially oriented dipole source in the left somatosensory cortex. The simulation studies were carried out with the constraint of source location and the constraint of source location, direction and magnitude. While the conductivity estimation with the constraint of source location did not improve the result appreciably, the additional constraint of source direction and magnitude with the iteration scheme clearly improved the estimation results. Based on the simulation results, we can conclude that the iterative combined MEG/EEG conductivity estimation with the source parameter constraint is more robust at estimating tissue conductivity than the original EEG-only LRCE method. We also applied the combined method to real SEP/SEF data and the estimated brain and skull conductivities were 0.48 S/m and 0.0015 S/m, respectively. While this estimated brain conductivity is in the range of literature values, the skull conductivity is approximately three time less than the lower limit of the literature values.

7.2 Future Works

As with any study, this one introduces as many new questions and it provides answers and there is a wide range of future directions for this area of research. The basic concept of the LRCE approach is not limited to skull and brain conductivity, nor are these the only parameters in the inverse source localization problem that could influence the results in a meaningful way. Here we summarize just a few examples of specific extensions of our findings and ideas.

The LRCE results for a single combined SEP/SEF measurement is not representative for other head models. Further studies including more subjects and a variety of evoked potential measurements have to be performed and results of LRCE analysis have to be validated with other methods such as, e.g., EIT. The single dipole source might not be sufficient to appropriately model the SEP/SEF peak at 35 ms post-stimulus. Furthermore, realistic EEG/MEG data noise, segmentation inaccuracies, a too coarse FE meshing and the general limitations of the quasistatic Maxwell equations and the dipole model should be considered for the customized volume conductor. White matter conductivity anisotropy might play a bigger role as shown in Wolters *et al* and Güllmar *et al* [114].

There is an intimate relationship between skull thickness and specific conductivity as they both affect the solution of bioelectric field problems in the head by the same mechanisms. Hence, while we focused on conductivity in this study, a similar approach applied to the thickness of the skull could provide additional opportunities for model optimization. For the current study, we created a realistic head geometry from the T1- and PD-MR images in order to study the role of tissue conductivity in the solution of a finite element volume conductor problem. The assumption of the conductivity estimation was that the segmented geometry represented the anatomy of a head as closely as possible, so that we could estimate an absolute tissue conductivity value. The PD-MR image was used as an adjunct to more typical T1-MRI, which avoided the need for ionizing radiation of CT and yet still allowed us to extract an inner skull boundary. However, because the skull conductivity is relatively much smaller than other tissues, a small variation of the skull thickness has larger impact than that of other tissues. By perturbing the skull thickness and applying an LRCE type approach, we could quantify the variation of the estimated conductivity that arises due to errors in skull thickness measurements.

All of the results presented here are based on the assumption that skull conductivity is a constant, at least over one patient or a short period of time, and isotropic. However, there is evidence to suggest that conductivity does depend on orientation of the current, i.e., it is anisotropic and consists of highly conducting soft *spongiosa* sandwiched by two layers of poorly conducting hard *compacta*[3]. Including the assumptions of anisotropy of skull conductivity is therefore an additional potential direction for future development. The finite element approach is very well suited to inclusion of anisotropy, through an effective anisotropic conductivity assigned to each FE element of skull compartment [3]. Extending the LRCE approach to include anisotropy would require modifications and it is not clear that it would generate stable results given the additional optimization parameters.

A recent study of Sadlier *et al* [113] reported that it might not be enough to approximate the influence of outer compacta, spongiosa and inner compacta on the skull tissue conductivity by means of a mere radial-to-tangential anisotropy. This result indicates that a skull anisotropy does not accurately model the conductivity of skull compartment and suggests that a segmentation of the three skull layers is necessary for an accurate representation of skull tissue inhomogeneity. As long as a segmentation of the spongiosa is available, FE approach is able to model the three-layeredness in a high-resolution.

Similar to the inclusion of anisotropy in the skull conductivity, it would also be possible and justified to include anisotropic white matter conductivity in a comprehensive source localization. In the current study, we used a four compartment model, in which the brain was modeled as one homogeneous tissue and assigned an isotropic conductivity value. However, the brain tissue consists of two substances, gray matter and white matter and while the grey matter is isotropic, the fibrous structure of the white matter gives it a high degree of anisotropic conductivity. The preferable pathway of water diffusion in the white matter captured from DT-MR imaging can be used to build a directional preference of electric conduction and to formulate anisotropic conductivity tensors for the white matter. Nevertheless, each tensor provides the information of anisotropic conductivity ratio, not the absolute conductivity value. Recent study of Wolters *et al* [3] indicated that conductivity in the modeling of white matter may give a more accurate forward solution, especially when the sources are located deep in the brain. Our combined MEG/EEG conductivity estimation could be extended to estimate the absolute conductivity value of anisotropic white matter with a FEM volume conductor model. In addition, the combined estimation could be extended to estimate the scaling factor (just one parameter for the white matter compartment) between the measured diffusion tensors and the conductivity tensors that are computed from the diffusion tensors by means of an effective medium approach as proposed by Tuch *et al* [115, 116] and used in Wolters *et al* [28] and Güllmar *et al* [114].

Validation is an ongoing and sometimes challenge aspect of any simulation studies and there are additional approaches to testing the accuracy of LRCE based source localization. One such possibility is to validate the conductivity estimation method with other event related experimental data such as visually evoked potential/field (VEP/VEF) and auditory evoked potential/field (AEP/AEF). In the current study, only SEP/SEF were used to estimate tissue conductivity and by exciting other sensory systems, the source location would shift and thus provide extended validation options. While the resulting conductivities from such simulations might vary, they could provide a reasonable range of values that would limit the choice of conductivity and provide the information for some constraints.

One source of uncertainty in all practical applications of source localization is determining the number of independent sources active in the brain. An incorrect assumption about this value can lead to high errors in the resulting solution, whereas knowledge of the number of sources provides a strong constraint on the viable solutions. To resolve this ambiguity, the dipole fit method, the basis of the conductivity estimation method, could be combined with the method of *linear estimation* or *independent component analysis* (ICA) to accommodate the more realistic measurement data. As in the evoked potential experiment in the current research, there are cases in which we can correctly assume the number of sources. However, it is not always easy to predict the number of source in advance and many realistic clinical cases fall into this category. Accordingly, when the number of sources is uncertain, the dipole fit method may not be a good means of source localization. Instead, one should first determine the number of sources from the given EEG or MEG data in order to apply the properly constrained dipole fit approach to the given data. One such method is the *linearized estimation* in the source localization. The linearized estimation does not need to specify the number of sources, instead it solves the linear system of equations without specifying the number of sources for a source vector of source strengths. With this information, it is then possible to evaluate the source strength map that may indicate the number of sources. Another method with the same goal is the *principal component analysis* (PCA) or the ICA. The methods decompose EEG or MEG data into principal components or independent components, respectively. Among the components, we can extract source components and disregard all the other artifacts. The number of source components may be used as an *a priori* constraint on the number of sources in the dipole fit approach.

One original implicit goal of our studies was to maximize the utility of the EEG to help localize brain sources, in part because of its simplicity to apply and low cost. We have shown, however, that the additional MEG data from the same patient can substantially improve the accuracy of our approach. Thus an intriguing future study would be to use the MEG as we have used the EEG and consider the accuracy of an MEG-based forward solution with a finite element conductor model. In the current study, we used only EEG modality and evaluated the forward solution accuracy with respect to dipole models. For a future study, MEG should go through an accuracy evaluation with respect to dipole models with a finite element model [4]. One could follow the same method as used in the evaluation of the EEG forward accuracy. In addition, the radial source could serve as a good measure of numerical accuracy of the finite element model, since the MEG does not see the radial source activity due to the symmetry of sphere. Thus an MEG-based forward simulation for a radial source with a spherical head model would provide the numerical error due to the use of FEM modeling techniques.

Another core assumption of most brain source modeling is that a focal source is the most realistic choice for the actual distribution of bioelectric fields in the head. However, there are fields that might be better described as coming from a distributed source and there is a persistent need for high quality, realistic models for such sources. Developing and evaluating such models is a significant task but one that is critical for the application of source modeling to a wide array of disorders.

APPENDIX A

PUBLICATIONS

A.1 Peer-Reviewed Journal Publications

1. S. Lew, C. Wolters, T. Dierkes, C. Roer, RS MacLeod, "Accuracy and time comparison for different potential approaches and iterative solvers in finite element method based EEG source analysis", Applied Numerical Mathematics, (in review)

2. S. Lew, C. Wolters, A. Anwander, S. Makeig, RS MacLeod, "Improved EEG source localization using low resolution conductivity estimation in a realistic head model", Human Brain Mapping, (in review)

3. S. Lew, C. Wolters, B. Lanfer, RS MacLeod, "EEG/MEG combined analysis with tissue conductivity estimation in a realistic head model", NeuroImage, (in preparation)

A.2 Peer-Reviewed Conference Proceedings

1. S. Lew, C. Wolters, A. Anwander, S. Makeig, R.S. MacLeod. Low Resolution Conductivity Estimation to Improve Source Localization. In New Frontiers in Biomagnetism. Proceedings of the 15th International Conference on Biomagnetism, Vancouver, BC, Canada, August 21-25, 2006., International Congress Series, Vol. 1300, pp. 149–152. June, 2007.

2. C. H. Wolters, A. Anwander, X. Tricoche, S. Lew, C.R. Johnson. Influence of Local and Remote White Matter Conductivity Anisotropy for a Thalamic Source on EEG/MEG Field and Return Current Computation. In Int.Journal of Bioelectromagnetism, Vol. 7, No. 1, pp. 203–206. 2005

A.3 Abstracts

1. CH. Wolters, S. Lew, F. Drechsler, T. Dierkes, L. Grasedyck, Improved EEG/MEG forward modeling using conductivity fitting in realistic finite element volume conductor models, Deutsches EEG/EP Meeting, Gissen, Germany, October 19-21, 2007
2. S. Lew, C. Wolters, A. Anwander, S. Makeig, RS MacLeod. Simulation study of brain source localization by conductivity fitting. In 2nd Annual Mountain West Biomedical Engineering Conference, Snowbird, Utah, September 15-16, 2006
3. S. Lew, C. Wolters, K. Lee, S. Makeig, G. Worrell, R. MacLeod. Epileptogenic Source Localization For Open Skull Head Model of Epilepsy By Independent Component Analysis And Inverse Dipole Fit Method. In 1st Annual Mountain West Biomedical Engineering Conference, Snowbird, Utah, September 16-17, 2005

A.4 Other Presentations

1. S. Lew, C Wolters, R.S. MacLeod. EEG/MEG source analysis and brain tissue conductivity. SCI seminar, SCI Institute, University of Utah, March 14, 2008
2. S. Lew, C Wolters, R.S. MacLeod. Source localization in realistic head model with the simulated annealing algorithm. Instituts Kolloquium, Biomagnetismus und Biosignalanalyse, Muenster, Germany, December 15, 2005

APPENDIX B

THE VENANT DIRECT APPROACH

To derive the Venant direct potential approach, we follow the ideas of [5] and start from the basic relation for a dipole moment $\mathbf{T}_0 \in \mathbb{R}^3$ at position $\mathbf{x}_0 \in \mathbb{R}^3$, $\mathbf{T}_0 = \int_\Omega (\mathbf{x} - \mathbf{x}_0) \mathrm{J}^p(\mathbf{x}) d\mathbf{x}$ (see, e.g., [117, formula (2.92)]). Assuming discrete sources and sinks on only the C neighboring FE mesh nodes to the FE node which is closest to $\mathbf{x}_0$, $\mathbf{T}_0 = \sum_{c=1}^{C} \Delta\mathbf{x}_{c0} \underline{j}_0^{[c]}$ with $\Delta\mathbf{x}_{c0}$ denoting the vector from FE node c to source position $\mathbf{x}_0$. When using higher moments $\underline{\bar{T}}_0^r \in \mathbb{R}^{n_0+1}$ with $n_0 = 1, 2$ and the Cartesian direction r ($r = x, y, z$), this expression becomes

$$\left(\underline{\bar{T}}_0^r\right)^{[n]} = \left(\underline{\bar{T}}_0^r\right)^{[n]} \left(\underline{j}_0\right) = \sum_{c=1}^{C} \left(\Delta\bar{x}_{c0}^r\right)^n \underline{j}_0^{[c]} \qquad \forall n \in 0, \ldots, n_0 \tag{B.1}$$

(for a motivation of higher moments see [5]). The bar indicates a scaling with a reference length a_{ref}, so that

$$\Delta\bar{x}_{c0}^r = \Delta x_{c0}^r / a_{\mathrm{ref}} \overset{!}{<} 1 \tag{B.2}$$

is dimensionless and the physical dimension of the resultant scaled n^{th} order moment, $\left(\underline{\bar{T}}_0^r\right)^{[n]}$, is that of a current (i.e., Amps). The reference length a_{ref} has to be chosen so that $\Delta\bar{x}_{c0}^r$ is less than 1. The equation is well known from the Saint Venant law in mechanical engineering — small forces in combination with long lever arms have the same effect on the system as large forces in combination with short lever arms.

If we now define the matrix $\bar{X}_0^r \in \mathbb{R}^{(n_0+1)\times C}$, the moment vector $\underline{\bar{M}}_0^r \in \mathbb{R}^{n_0+1}$, computed from a given dipole moment vector $\mathbf{M}_0$, and the diagonal source weighting matrix $\bar{W}_0^r \in \mathbb{R}^{C\times C}$ by

$$\begin{aligned} \left(\bar{X}_0^r\right)^{[n,c]} &= \left(\Delta\bar{x}_{c0}^r\right)^n \\ \left(\underline{\bar{M}}_0^r\right)^{[n]} &= M_0^r \left(\frac{1}{2a_{\mathrm{ref}}}\right)^n \left(1 - (-1)^n\right) \\ \bar{W}_0^r &= \mathrm{DIAG}\left(\left(\Delta\bar{x}_{10}^r\right)^s, \ldots, \left(\Delta\bar{x}_{C0}^r\right)^s\right) \end{aligned} \tag{B.3}$$

with $s = 0$ or $s = 1$, then we can compute the monopole load vector $\underline{j}_0 \in \mathbb{R}^C$ for the Venant direct approach on the C neighboring FE nodes from a given dipole moment vector $\mathbf{M}_0$ at position $\mathbf{x}_0$ by means of minimizing the following functional

$$F_\lambda(\underline{j}_0) = \|\underline{\bar{M}}_0^r - \underline{\bar{T}}_0^r(\underline{j}_0)\|_2^2 + \lambda\|\bar{W}_0^r\underline{j}_0\|_2^2 = ||\underline{\bar{M}}_0^r - \bar{X}_0^r\underline{j}_0||_2^2 + \lambda\|\bar{W}_0^r\underline{j}_0\|_2^2 \overset{!}{=} \min.$$

The first part of the functional F_λ ensures a minimal difference between the moments of the Venant approach $\underline{\bar{T}}_0^r$ and the target moments $\underline{\bar{M}}_0^r$, while the second part smoothes the monopole distribution in a weighted sense and enables a unique minimum for F_λ. The solution of the minimization problem is given by

$$\left((\bar{X}_0^r)^{tr}\bar{X}_0^r + \lambda(\bar{W}_0^r)^{tr}\bar{W}_0^r\right)\underline{j}_0 = (\bar{X}_0^r)^{tr}\underline{\bar{M}}_0^r$$

(see, e.g., [118, Theorem 4.2.1]), so that the final solution for the monopole source vector $\underline{j}_0$ of the Venant approach is given by

$$\underline{j}_0 = \left(\sum_{r=1}^{3}\left\{(\bar{X}_0^r)^{tr}\bar{X}_0^r + \lambda(\bar{W}_0^r)^{tr}\bar{W}_0^r\right\}\right)^{-1}\sum_{r=1}^{3}\left\{(\bar{X}_0^r)^{tr}\underline{\bar{M}}_0^r\right\}. \tag{B.4}$$

The order n_0 is generally chosen as $n_0 = 1$ or $n_0 = 2$, where the latter imposes a spatial concentration of loads in the dipole axis. Furthermore, $s = 1$ stresses the spatial concentration of loads around the dipole. With $\Phi(\mathbf{x}) \approx \Phi_h(\mathbf{x}) = \sum_{j=1}^{N_h}\varphi_j(\mathbf{x})\underline{u}_h^{[j]}$, we can derive the linear system

$$K_h\underline{u}_h = \underline{j}_{\text{Venant},h} \tag{B.5}$$

with the same stiffness matrix as in (3.13). The right-hand side vector $\underline{j}_{\text{Venant},h} \in \mathbb{R}_h^N$ has only C non-zero entries and is determined by

$$\underline{j}_{\text{Venant},h}^{[i]} = \begin{cases} \underline{j}_0^{[c]} & \text{if } \exists c \in \{1,\ldots,C\} : i = \textsc{glob}(c), \\ 0 & \text{otherwise} \end{cases} \tag{B.6}$$

for a source at location $\mathbf{x}_0$. The function GLOB determines the global index i to each of the local indices c.

REFERENCES

[1] S. W. Ranson and S. L. Clark, *The Anatomy of Nervous System - Its Development and Function.* W. B. Sanders, 1959.

[2] H. Si, "TetGen, a quality tetrahedral mesh generator and three-dimensional delaunay triangulator, v1.3, user's manual," Weierstrass Institute for Applied Analysis and Stochastics, Tech. Rep. 9, 2004.

[3] C. Wolters, A. Anwander, D.Weinstein, M.Koch, X.Tricoche, and R.S.MacLeod, "Influence of tissue conductivity anisotropy on EEG/MEG field and return current computation in a realistic head model: A simulation and visualization study using high-resolution finite element modeling." *NeuroImage*, vol. 30, no. 3, pp. 813–826, 2006, http://dx.doi.org/10.1016/j.neuroimage.2005.10.014.

[4] B. Lanfer, C.H.Wolters, S.O.Demokritov, and C. Pantev, "Validating finite element method based eeg and meg forward computations." in *Proc. Biomedizinische Technik, Aachen, Germany.* ISSN: 0939-4990, September 26-29, (2007), pp. 140–149.

[5] H. Buchner, G. Knoll, M. Fuchs, A. Rienäcker, R. Beckmann, M. Wagner, J. Silny, and J. Pesch, "Inverse localization of electric dipole current sources in finite element models of the human head," *Electroenc. Clin. Neurophysiol.*, vol. 102, pp. 267–278, 1997.

[6] N. G. Gençer and C. E. Acar, "Sensitivity of EEG and MEG measurements to tissue conductivity," *Phys. Med. Biol.*, vol. 49, pp. 701–17, 2004.

[7] C. Ramon, P. Schimpf, J. Haueisen, M. Holmes, and A. Ishimaru, "Role of soft bone, CSF and gray matter in EEG simulations," *Brain Topogr.*, vol. 16, no. 4, pp. 245–8, 2004.

[8] T. Waberski, H. Buchner, K. Lehnertz, A. Hufnagel, M. Fuchs, R. Beckmann, and A. Rienäcker, "The properties of source localization of epileptiform activity using advanced headmodelling and source reconstruction," *Brain Top.*, vol. 10, no. 4, pp. 283–290, 1998.

[9] S. Baillet, J. Mosher, and R. Leahy, "Electromagnetic brain mapping," *IEEE Signal Processing Magazine*, vol. 18, no. 6, pp. 14–30, November 2001.

[10] J. Sarvas, "Basic mathematical and electromagnetic concepts of the biomagnetic inverse problem," *Phys.Med.Biol.*, vol. 32, no. 1, pp. 11–22, 1987.

[11] Y. Yan, P. Nunez, and R. Hart, "Finite-element model of the human head: Scalp potentials due to dipole sources," *Med.Biol.Eng.Comput.*, vol. 29, pp. 475–481, 1991.

[12] O. Bertrand, M. Thévenet, and F. Perrin, "3D finite element method in brain electrical activity studies," in *Biomagnetic Localization and 3D Modelling*, J. Nenonen, H. Rajala, and T. Katila, Eds. Report of the Dep. of Tech.Physics, Helsinki University of Technology, 1991, pp. 154–171.

[13] K. Awada, D. Jackson, J. Williams, D. Wilton, S. Baumann, and A. Papanicolaou, "Computational aspects of finite element modeling in EEG source localization," *IEEE Trans Biomed. Eng.*, vol. 44, no. 8, pp. 736–751, 1997.

[14] S. van den Broek, "Volume conduction effects in EEG and MEG," Ph.D. dissertation, Proefschrift Universiteit Twente Enschede, The Netherlands, 1997.

[15] H. Buchner, G. Knoll, M. Fuchs, A. Rienäcker, R. Beckmann, M. Wagner, J. Silny, and J. Pesch, "Inverse localization of electric dipole current sources in finite element models of the human head," *Electroenc. Clin. Neurophysiol.*, vol. 102, pp. 267–278, 1997.

[16] G. Marin, C. Guerin, S. Baillet, L. Garnero, and G. Meunier, "Influence of skull anisotropy for the forward and inverse problem in EEG: simulation studies using the FEM on realistic head models," *Human Brain Mapping*, vol. 6, pp. 250–269, 1998.

[17] J. Ollikainen, M. Vauhkonen, P. Karjalainen, and J. Kaipio, "Effects of local skull inhomogeneities on EEG source estimation," *Med.Eng.Phys.*, vol. 21, pp. 143–154, 1999.

[18] D. Weinstein, L. Zhukov, and C. Johnson, "Lead-field bases for electroencephalography source imaging," *Annals of Biomed.Eng.*, vol. 28, no. 9, pp. 1059–1066, 2000.

[19] P. Schimpf, C. Ramon, and J. Haueisen, "Dipole models for the EEG and MEG," *IEEE Trans Biomed. Eng.*, vol. 49, no. 5, pp. 409–418, 2002.

[20] C. Wolters, H. Köstler, C. Möller, J. Härtlein, L. Grasedyck, and W. Hackbusch, "Numerical mathematics of the subtraction method for the modeling of a current dipole in EEG source reconstruction using finite element head models." *SIAM J. on Scientific Computing*, vol. 30, no. 1, pp. 24–45, 2007.

[21] F. Drechsler, C. Wolters, T. Dierkes, H. Si, and L. Grasedyck, "A highly accurate full subtraction approach for dipole modelling in EEG source analysis using the finite element method." *J. Applied Numerical Mathematics*, 2007, in review.

[22] O. Tanzer, S. Järvenpää, J. Nenonen, and E.Somersalo, "Representation of bioelectric current sources using whitney elements in finite element method," *Phys.Med.Biol.*, vol. 50, pp. 3023–3039, 2005.

[23] J. de Munck, B. van Dijk, and H. Spekreijse, "Mathematical dipoles are adequate to describe realistic generators of human brain activity," *IEEE Trans Biomed. Eng.*, vol. 35, no. 11, pp. 960–966, 1988.

[24] S. Murakami and Y. Okada, "Contributions of principal neocortical neurons to magnetoencephalography and electroencephalography signals," *J.Physiol.*, vol. 575,

no. 3, pp. 925–936, 2006.

[25] N. Gencer and C. Acar, “Sensitivity of EEG and MEG measurements to tissue conductivity.” *Phys.Med.Biol.*, vol. 49, pp. 701–717, 2004.

[26] C. H. Wolters, L. Grasedyck, and W. Hackbusch, “Efficient computation of lead field bases and influence matrix for the FEM-based EEG and MEG inverse problem,” *Inverse Problems*, vol. 20, no. 4, pp. 1099–1116, 2004.

[27] H. Hallez, B. Vanrumste, P. V. Hese, Y. D’Asseler, I. Lemahieu, and R. V. de Walle, “A finite difference method with reciprocity used to incorporate anisotropy in electroencephalogram dipole source localization.” *Phys.Med.Biol.*, vol. 50, pp. 3787–3806, 2005.

[28] C. Wolters, *Influence of Tissue Conductivity Inhomogeneity and Anisotropy on EEG/MEG based Source Localization in the Human Brain*, ser. MPI Series in Cognitive Neuroscience. MPI of Cognitive Neuroscience Leipzig, 2003, no. 39, iSBN 3-936816-11-5 (also: Leipzig, Univ., Diss., http://lips.informatik.uni-leipzig.de/pub/2003-33/en).

[29] J. de Munck and M. Peters, “A fast method to compute the potential in the multi sphere model,” *IEEE Trans Biomed. Eng.*, vol. 40, no. 11, pp. 1166–1174, 1993.

[30] H. Schwarz, *Methode der finiten Elemente.* B.G.Teubner Stuttgart, 1991.

[31] J. Ruge and K. Stüben, “Algebraic multigrid (AMG),” in *Multigrid Methods*, ser. Frontiers in Applied Mathematics, S. McCormick, Ed. Philadelphia: SIAM, 1986, vol. 5, pp. 73–130.

[32] K. Stüben, “A review of algebraic multigrid,” GMD, Techn. Report 69, Nov. 1999, http://www.gmd.de.

[33] S. Reitzinger, “Algebraic multigrid methods for large scale finite element equations,” Ph.D. dissertation, Schriften der Johannes-Kepler-Universität Linz, Reihe C - Technik und Naturwissenschaften, No.36, 2001.

[34] G. Haase, M. Kuhn, and S. Reitzinger, “Parallel AMG on distributed memory computers,” *SIAM J. Sci.Comp.*, vol. 24, no. 2, pp. 410–427, 2002.

[35] D. L. Pham and J. L. Prince, “Adaptive fuzzy segmentation of magnetic resonance images,” *IEEE Trans. Med. Imag.*, vol. 18, no. 9, pp. 737–52, 1999.

[36] G. Huiskamp, M. Vroeijenstijn, R. van Dijk, G. Wieneke, and A. van Huffelen, “The need for correct realistic geometry in the inverse EEG problem,” *IEEE Trans. Biomed. Eng.*, vol. 46, no. 11, pp. 1281–1287, 1999.

[37] S. Baumann, D. Wozny, S. Kelly, and F. Meno, “The electrical conductivity of human cerebrospinal fluid at body temperature,” *IEEE Trans. Biomed. Eng.*, vol. 44, no. 3, pp. 220–3, 1997.

[38] J. Latikka, T. Kuume, and H. Eskola, “Conductivity of living intracranial tissues,” *Phys. Med. Biol.*, vol. 46, pp. 1611–1616, 2001.

[39] S. Rush and D. Driscoll, “Current distribution in the brain from surface electodes,” *Anesth. Analg.*, vol. 47, no. 6, pp. 717–23, 1968.

[40] S. Homma, T. Musha, Y. Nakajima, Y. Okamoto, S. Blom, R. Flink, and K. E. Hagbarth, “Conductivity ratios of scalp-skull-brain model in estimating equivalent dipole sources in human brain,” *Neurosci. Res.*, vol. 22, pp. 51–5, 1995.

[41] S. Gonçalves, J. C. de Munck, J. P. A. Verbunt, R. M. Heethaar, and F. H. L. da Silva, “In vivo measurement of the brain and skull resistivities using an EIT-based method and the combined analysis of SEF/SEP data,” *IEEE Trans. Biomed. Eng.*, vol. 50, no. 9, pp. 1124–1128, 2003.

[42] T. F. Oostendorp, J. Delbeke, and D. F. Stegeman, “The conductivity of the human skull: Results of *in vivo* and *in vitro* measurements,” *IEEE Trans. Biomed. Eng.*, vol. 47, pp. 1487–92, 2000.

[43] U. Baysal and J. Haueisen, “Use of a priori information in estimating tissue resistivities-application to human data in vivo,” *Physiol. Meas.*, vol. 25, pp. 737–48, 2004.

[44] Y. Lai, W. van Drongelen, L. Ding, K. E. Hecox, V. L. Towle, D. M. Frim, and B. He, “Estimation of in vivo human brain-to-skull conductivity ratio from simultaneous extra- and intra-cranial electrical potential recordings,” *Clin.Neurophysiol.*, vol. 116, pp. 456–65, 2005.

[45] S. Gonçalves, J. C. de Munck, P. A. Jeroen, V. F. B, R. M. Heethaar, and F. L. L. da Silva, “In vivo measurement of the brain and skull resistivities using an EIT-based method and realistic models for the head,” *IEEE Trans. Biomed. Eng.*, vol. 50, no. 6, pp. 754–67, 2003.

[46] B. N. Cuffin, “EEG localization accuracy improvements using realistically shaped head model,” *IEEE Trans. Biomed. Eng.*, vol. 43, pp. 299–303, 1996.

[47] J. de Munck and M. Peters, “A fast method to compute the potential in the multi sphere model,” *IEEE Trans Biomed Eng*, vol. 40, no. 11, pp. 1166–1174, 1993.

[48] J. Sarvas, “Basic mathematical and electromagnetic concepts of the biomagnetic inverse problem,” *Phys. Med. Biol.*, vol. 32, no. 1, pp. 11–22, 1987.

[49] M. Hämäläinen and J. Sarvas, “Realistic conductivity geometry model of the human head for interpretation of neuromagnetic data,” *IEEE Trans Biomed. Eng.*, vol. 36, pp. 165–171, 1989.

[50] J. de Munck, “A linear discretization of the volume conductor boundary integral equation using analytically integrated elements,” *IEEE Trans Biomed. Eng.*, vol. 39, no. 9, pp. 986–990, 1992.

[51] M. Fuchs, M. Wagner, H. Wischmann, T. Köhler, A. Theißen, R. Drenckhahn, and H. Buchner, "Improving source reconstructions by combining bioelectric and biomagnetic data," *Electroenc. Clin. Neurophysiol.*, vol. 107, pp. 93–111, 1998.

[52] H. Hallez, B. Vanrumste, P. V. Hese, Y. D'Asseler, I. Lemahieu, and R. V. de Walle, "A finite difference method with reciprocity used to incorporate anisotropy in electroencephalogram dipole source localization." *Phys.Med.Biol.*, vol. 50, pp. 3787–3806, 2005.

[53] O. Bertrand, M. Thévenet, and F. Perrin, "3D finite element method in brain electrical activity studies," in *Biomagnetic Localization and 3D Modelling*, J. Nenonen, H. Rajala, and T. Katila, Eds. Report of the Dep. of Tech.Physics, Helsinki University of Technology, 1991, pp. 154–171.

[54] Y. Yan, P. L. Nunez, and R. T. Hart, "A finite-element model of the human head: scalp potentials due to dipole sources," *Med. Biol. Eng. Comput.*, vol. 29, pp. 475–81, 1991.

[55] G. Marin, C. Guerin, S. Baillet, L. Garnero, and G. Meunier, "Influence of skull anisotropy for the forward and inverse problem in EEG: simulation studies using the FEM on realistic head models," *Hum. Brain Mapp.*, vol. 6, pp. 250–69, 1998.

[56] D. Weinstein, L. Zhukov, and C. Johnson, "Lead-field bases for EEG source imaging," *Annals of Biomed. Eng.*, vol. 28, no. 9, pp. 1059–66, 2000.

[57] C. Wolters, H. L. Grasedyck, and W. Hackbusch, "Efficient computation of lead field bases and influence matrix for the FEM-based EEG and MEG inverse problem,," *Inverse Problems*, vol. 40, pp. 1099–116, 2004.

[58] C. H. Wolters, M. Kuhn, A. Anwander, and S. Reitzinger, "A parallel algebraic multigrid solver for finite element method based source localization in the human brain," *Comp. Vis. Sci.*, vol. 5, pp. 165–77, 2002.

[59] J. Mosher and R. Leahy, "Source localization using recursively applied and projected (RAP) MUSIC," *IEEE Trans. Sig. Proc.*, vol. 47, no. 2, pp. 332–340, 1999.

[60] D. Cohen and B. N. Cuffin, "A method for combining MEG and EEG to determine the sources," *Phys. Med. Biol*, vol. 32, no. 1, pp. 85–89, 1987.

[61] F. Babiloni, C. Babiloni, F. Carducci, G. Romani, P. M. Rossini, L. M. Angelone, and F. Cincotti, "Multimodal integration of high-resolution eeg and functional magnetic resonance imaging data: a simulation study," *NeuroImage*, vol. 19, no. 1, pp. 1–15, 2003.

[62] G. JS, A. CJ, M. JC, S. DM, R. DM, S. HA, W. CC, L. JD, S. JA, and B. JW, "Mapping function in the human brain with magnetoencephalography, anatomical magnetic resonance imaging, and functional magnetic resonance imaging," *J. Clin. Neurophysiol.*, vol. 12, no. 5, pp. 406–431, 1995.

[63] F. Babiloni, F. Cincotti, C. Babiloni, F. C. D. Mattia, L. Astolfi, A. Basilisco, P. R. L. Ding, Y. Ni, J. Cheng, K. Christine, J. Sweeney, and B. He, "Estimation

of the cortical functional connectivity with the multimodal integration of high-resolution eeg and fmri data by directed transfer function," *NeuroImage*, vol. 24, no. 1, pp. 118–131, 2004.

[64] E. N. Brown, "Signal processing and statistical challenges in neuroscience data analysis," *SIAM News*, vol. 40, no. 2, March 2007.

[65] S. Baillet, J. C. Mosher, and R. M. Leahy, "Electromagnetic brain mapping," *IEEE Signal Processing Maagazine*, pp. 14–30, November 2001.

[66] M. Huang, T. Song, D. Hagler, I. Podgorny, V. Jousmaki, L.Cui, K.Gaa, D.L.Harrington, A. Dale, R.R.Lee, J.Elman, and E.Hargren, "A novel integrated MEG and EEG analysis method for dipolar sources," *NeuroImage*, vol. 37, pp. 731–748, 2007.

[67] R. Plonsey and D. Heppner, "Considerations on quasi-stationarity in electrophysiological systems," *Bull. Math. Biophys.*, vol. 29, pp. 657–64, 1967.

[68] C. H. Wolters, *Influence of tissue conductivity inhomogeneity and anisotropy on EEG/MEG based source localization in the human brain.* Leipzig, also: Leipzig, Univ., Diss, http://lips.informatik.uni-leipzig.de/pub/2003-33/en: In:MPI Series in Cognitive Neuroscience, 2003.

[69] L. Geddes and L. Baker, "The specific resistance of biological materials. A compendium of data for the biomedical engineer and physiologist," *Med. Biol. Eng.*, vol. 5, pp. 271–93, 1967.

[70] S. Rush and D. Driscoll, "EEG electrode sensitivity: An application of reciprocity," *IEEE Trans. Biomed. Eng.*, vol. 16, pp. 15–22, 1969.

[71] M. J. Brookesa, A. M. Gibsona, S. D. Hallb, P. L. Furlongb, G. R. Barnesb, A. Hillebrandb, K. D. Singhb, I. E. Hollidayb, S. T. Francisa, and P. G. Morris, "A general linear model for meg beamformer imaging," *NeuroImage*, vol. 23, no. 3, November 2004.

[72] J.C.Mosher, P. Lewis, and R. Leahy, "Multiple dipole modeling and localization from spatio-temporal meg data," *IEEE Trans. Biomed. Eng.*, vol. 39, pp. 541–53, 1992.

[73] D. Gutiérrez, A. Nehorai, and C. H. Muravchik, "Estimating brain conductivities and dipole source signals with EEG arrays," *IEEE Trans. Biomed. Eng.*, vol. 51, pp. 2113–2122, 2004.

[74] C. Wolters, A. Anwander, G. Berti, and U. Hartmann, "Geometry-adapted hexahedral meshes improve accuracy of finite element method based EEG source analysis," *IEEE Trans.Biomed.Eng.*, vol. 54, no. 8, pp. 1446–1453, 2007.

[75] C. Wolters, H. Köstler, C. Möller, J. Härtlein, L. Grasedyck, and W. Hackbusch, "Numerical mathematics of the subtraction method for the modeling of a current dipole in EEG source reconstruction using finite element head models." *SIAM J. on Scientific Computing*, vol. 30, no. 1, pp. 24–45, 2007.

[76] K. Awada, D. Jackson, J. Williams, D. Wilton, S. Baumann, and A. Papanicolaou, "Computational aspects of finite element modeling in EEG source localization," *IEEE Trans. Biomed. Eng.*, vol. 44, no. 8, pp. 736–751, 1997.

[77] F. Drechsler, C. Wolters, T. Dierkes, H. Si, and L. Grasedyck, "A highly accurate full subtraction approach for dipole modelling in EEG source analysis using the finite element method." *J. Applied Numerical Mathematics*, 2007, in review.

[78] M. Mohr, *Simulation of Bioelectric Fields: The Forward and Inverse Problem of Electroencephalographic Source Analysis*, ser. Arbeitsberichte des Instituts für Informatik. Friedrich-Alexander-Universität Erlangen-Nürnberg, 2004, vol. Band 37, no. Nummer 6, iSSN 1611-4205.

[79] W. Hackbusch, *Iterative solution of large sparse systems of equations.* New York, Berlin, HEidelberg, London, Paris, Tokyo, Hong Kong, Barcelona, Budapest: Springer Verlag, 1994.

[80] Y. Saad, *Iterative methods for sparse linear systems.* PWS Publishing Company, 1996.

[81] H. Schwarz, *Methode der finiten Elemente.* B.G.Teubner Stuttgart, 1991.

[82] M. Scherg and D. von Cramon, "Two bilateral sources of the late AEP as identified by a spatio-temporal dipole model," *Electroencephalogr Clin Neurophysiol*, vol. 62, no. 1, pp. 32–44, 1985.

[83] M. Mertens and B. Lütkenhöner, "Efficient neuromagnetic determination of landmarks in the somatosensory cortex," *Clin. Neurophysiol.*, vol. 111, pp. 1478–87, 2000.

[84] C. Wolters, R. Beckmann, A. Rienäcker, and H. Buchner, "Comparing regularized and non-regularized nonlinear dipole fit methods: a study in a simulated sulcus structure," *Brain Topogr.*, vol. 12, no. 1, pp. 3–18, 1999.

[85] H. R. Schwarz, *Methode der finiten Elemente.* PWS Publishing Company, 1996.

[86] J. Ruge and K. Stüben, "Algebraic multigrid (AMG)," in *Multigrid Methods*, ser. Frontiers in Applied Mathematics, S. McCormick, Ed. Philadelphia: SIAM, 1986, vol. 5, pp. 73–130.

[87] K. Stüben, "A review of algebraic multigrid," *Techn. report 69, GMD*, 1999.

[88] M. Jung and U. Langer, "Applications of multilevel methods to practical problems," *Surv. Math. Ind.*, vol. 1, pp. 217–57, 1991.

[89] 2000-2003, simBio: A Generic Environment for Bio-Numerical Simulation, IST-Program of the European Commission, Project No.10378, http://www.simbio.de.

[90] H. Si and K. Gärtner, "Meshing piecewise linear complexes by constrained Delaunay tetrahedralizations," in *Proc. 14th International Meshing Roundtable.* Sandia National Laboratories, 2005, pp. 147–163.

[91] J. Meijs, O. Weier, M. Peters, and A. van Oosterom, “On the numerical accuracy of the boundary element method,” *IEEE Trans Biomed. Eng.*, vol. 36, pp. 1038–1049, 1989.

[92] B. J. Roth, M. Balish, A. Gorbach, and S. Sato, “How well does a three sphere model predict positions of dipoles in a realistically shaped head,” *Electroenc. Clin. Neurophysiol.*, vol. 87, pp. 175–84, 1993.

[93] M. Wagner, “Rekonstruktion neuronaler Ströme aus bioelektrischen und biomagnetischen Messungen auf der aus MR-Bildern segmentierten Hirnrinde,” Ph.D. dissertation, Shaker-Verlag, Aachen, ISBN 3-8265-4293-2, 1998.

[94] 2000, cURrent Reconstruction and Imaging, http://www.neuro.com.

[95] J. A. Nelder and R. Mead, “A simplex method for function minimization,” *Comput. J.*, vol. 7, no. 4, pp. 308–13, 1965.

[96] D. W. Marquardt, “An algorithm for least-squares estimation of nonlinear parameters,” *J. Soc. Indust. Appl. Math.*, vol. 11, pp. 431–41, 1963.

[97] S. Kirkpatrick, C. D. Gelatt Jr, and M. P. Vecchi, “Optimization by simulated annealing,” *Science*, vol. 220, pp. 671–80, 1983.

[98] H. Haneishi, N. Ohyama, K. Sekihara, and T. Honda, “Multiple current dipole estimation using simulated annealing,” *IEEE Trans. Biomed. Eng.*, vol. 41, no. 11, pp. 1004–9, 1994.

[99] J. Gerson, V. A. Vardenas, and G. Fein, “Equivalent dipole parameter estimation using simulated annealing,” *Electroenceph. Clin. Neurophysiol.*, vol. 92, pp. 161–8, 1994.

[100] K. Uutela, M. Hämäläinen, and R. Salmelin, “Global optimization in the localization of neuromagnetic sources,” *IEEE Trans. Biomed. Eng.*, vol. 45, no. 6, pp. 716–23, 1998.

[101] N. Metropolis, A. Rosenbluth, M. Rosenbluth, A. Teller, and E. Teller, “Equation of state calculations by fast computing machines,” *J. of Chem. Phys.*, vol. 21, pp. 1087–92, 1953.

[102] S. Geman and D. Geman, “Stochastic relaxation, Gibbs distribution and the Bayesian restoration of images,” *IEEE Trans. Pattern Anal. Mach. Intell.*, vol. PAMI-6, no. 6, pp. 721–41, 1984.

[103] S. Hütten, “Über das asymptotische Verhalten von Simulated Annealing,” Diplomarbeit in Mathematik, Institut f?r Statistik und Wirtschaftsmathematik, RWTH Aachen, 1993, http://www.stochastik.rwth-aachen.de/si/.

[104] J. H. Lee, M. Garwood, R. Meno, G. Adriany, P. Anderson, C. L. Truwit, and K. Ugurbil, “High contrast and fast 3D magnetic resonance imaging at high fields,” *Magn. Reson. Med.*, vol. 34, pp. 308–312, 1995.

[105] A. Haase, J. Frahm, D. Matthaei, W. Hänicke, and K. D. Merboldt, “FLASH imaging: rapid NMR imaging using low flip-angle pulses,” *J. Magn. Reson.*, vol. 67, pp. 258–66, 1986.

[106] J. Haueisen, “Methods of numerical field calculation for neuromagnetic source localization,” Ph.D. dissertation, Shaker-Verlag Aachen, ISBN 3-8265-1691-5, 1996.

[107] BESA, “Brain Electric Source Analysis,” 2007, http://www.besa.de.

[108] S. Vallaghe, M. Clerc, and J.-M. Badier, “In vivo conductivity estimation using somatosensory evoked potentials and cortical constraint on the source.” *4th IEEE Int. Symp. on Biomedical Imaging*, pp. 1036–9, 2007.

[109] S. M. Plis, J. S. George, S. C. Jun, D. M. Ranken, P. L. Volegov, and D. M. Schmidt, “Probabilistic forward model for electroencephalography source analysis,” *Phys. Med. Biol.*, vol. 52, pp. 5309–5327, 2007.

[110] R. Hari and N. Forss, “Magnetoencephalography in the study of human somatosensory cortical processing,” *Phil. Trans. R. Soc. Lond.*, vol. 354, no. Ser. B, pp. 1145–1154, 1999.

[111] R. Hoekema, G. H. Wieneke, F. S. S. Leijten, C. W. M. van Veelen, P. C. van Rijen, G. J. M. Huiskamp, J. Ansems, and A. C. van Huffelen, “Measurement of the conductivity of skull, temporarily removed during epilepsy surgery,” *Brain Topogr.*, vol. 16, no. 1, pp. 29–38, 2003.

[112] J. Haueisen, D. Tuch, C. Ramon, P. Schimpf, V. Wedeen, J. George, and J. Belliveau, “The influence of brain tissue anisotropy on human EEG and MEG,” *NeuroImage*, vol. 15, pp. 159–166, 2002.

[113] R. J. Sadleir and A. Argibay, “Modeling skull electrical properties,” *Ann. Biomed. Eng*, vol. 35, no. 10, pp. 11–22, 2007.

[114] D. Güllmar, J. Haueisen, M. Eiselt, F. Gießler, L. Flemming, A. Anwander, T. R. Knösche, C. H. Wolters, M. Dümpelmann, D. Tuch, and J. R. Reichenbach, “Influence of anisotropic copnductivity on eeg source reconstruction: Investigations in a rabbit model,” *IEEE Trans Biomed Eng*, 2006.

[115] D. Tuch, V. Wedeen, A. Dale, J. George, and J. Belliveau, “Conductivity mapping of biological tissue using diffusion MRI,” *Ann. NYAS*, vol. 888, pp. 314–316, 1999.

[116] ——, “Conductivity tensor mapping of the human brain using diffusion tensor MRI,” *Proc.Natl.Acad.Sci.USA*, vol. 98, no. 20, pp. 11 697–11 701, 2001.

[117] W. Nolting, *Grundkurs: Theoretische Physik, Elektrodynamik.* Zimmermann-Neufang, Ulmen, 1992.

[118] A. Louis, *Inverse und schlecht gestellte Probleme.* Teubner-Verlag, 1989.